IMPROVING ATOMISTIC SIMULATIONS TO PREDICT DEFORMATION AND FRACTURE

A Dissertation

Presented to the Faculty of the Graduate School

of Cornell University

in Partial Fulfillment of the Requirements for the Degree of

Doctor of Philosophy

by

Kristopher Learion Baker

August 2012

IMPROVING ATOMISTIC SIMULATIONS TO PREDICT DEFORMATION AND FRACTURE

Kristopher Learion Baker, Ph.D.

Cornell University 2012

Atomistic simulations can illuminate detailed mechanisms of brittle and ductile fracture and plasticity. However, there are many limitations to these simulations like short timescales, small spatial scales, and limitations of the discretization. Using molecular dynamics (MD) and multiscale methods, adaptations can be made to allow MD to answer problems relevant to engineers. In the first of three examples, MD is adapted to simulate brittle fracture by changing the discretization and allowing permanent damage between particles. By changing the discretization, specific mechanisms inherent to MD can be suppressed to allow accurate, macroscopic simulations of dynamic fragmentation of brittle materials. Second, the timescale available to MD is extended in a concurrent multiscale method (CADD) combined with accelerated MD. This combined approach allows for microseconds of simulation time at experimentally achievable loading rates. The method is applied to crack opening in aluminum alloys, and the effect of the loading rate on crack growth mechanisms is observed. From the results, it is clear that crack growth mechanisms depend greatly on the rate of the far-field loading. Third, the effect of aging on fatigue crack growth is studied by varying the resistance to dislocation motion in the dislocation dynamics region of CADD. Only in a multiscale simulation like CADD, can dislocation pileups reaching microns into the material interact with the atomic-scale mechanisms at a crack tip. The results of the simulations indicated that increasing

the friction force raises the fatigue crack threshold. Also, a transition from stage I fatigue crack growth to stage II fatigue crack growth occurs by dislocations shielding dislocation nucleation on the primary slip plane. These observations support the conclusion that the fatigue crack growth threshold is controlled by the spacing between obstacles to dislocation glide, which is consistent with experimental observations.

BIOGRAPHICAL SKETCH

Kristopher Baker grew up in central Pennsylvania just north of Harrisburg. He graduated salutatorian of Susquenita High School in 2003. He attended Bucknell University, where he majored in Civil and Environmental Engineering. He graduated in 2007 with a Bachelor of Science in Civil Engineering with the highest GPA in his major. In the summer of 2007, Kris married Amanda Schroeder and moved to Ithaca, NY. Both he and his wife started graduate school at Cornell University in August of 2007. Kris has been studying in the School of Civil and Environmental engineering, with a concentration in structural engineering, for the past five years. In January of 2011, he received his Masters of Science in Civil and Environmental Engineering. In their spare time, Amanda and Kris practice Taekwondo under Master Han Cho at C.W. Taekwondo in Ithaca, NY, and help teach intermediate and beginner Taekwondo classes at Cornell University. They both received their first Dan black belts after testing in January of 2011.

To Amanda, my confidante, for growing with me and helping me become the person I am today.

To Sabumnim for pushing me in more ways than I realized.

To my family for all your support.

ACKNOWLEDGEMENTS

I gratefully acknowledge support from Ed Glaessgen and Steve Smith at NASA (Grant No. NNX08BA39A), Paul Hess at the Office of Naval Research (Grant No. N000141010323), and Ali Sayir at the Air Force Office of Scientific Research (Grant No. FA95501110273). I am also grateful for funding from Cornell's McMullen Fellowship during the 2007-2008 academic year.

TABLE OF CONTENTS

LIST OF TABLES

LIST OF FIGURES

CHAPTER 1

INTRODUCTION

Standard molecular dynamics (MD) methods are limited by their discretization, and the spatial scale and time scale able to be simulated. In particular, using MD to study deformation and fracture of engineering materials can be difficult when limited to nanoseconds of simulation time of a nanometer-scaled specimen. Nonetheless, MD provides a physics-based method that is ideal for exploring the atomic-scale mechanisms of deformation that would be useful for predicting the onset of failure, or providing insight to improve the design of new materials. This dissertation provides three examples of creating or using algorithms that extend and improve upon standard MD to study problems relevant to engineers and comparable to physical experiments.

The second chapter, entitled "Simulating Dynamic Fragmentation Processes with Particles and Elements," is published in *Engineering Fracture Mechanics* as indicated in the chapter. This work details how the molecular dynamics method can be used to accurately simulate the dynamic fragmentation of bulk brittle materials by modifying the material connectivity. It also addresses modeling concerns including convergence of the fragment mass distribution, possible non-physical results (or incorrect type of physics), and the effect of the initial defect distribution.

The third chapter, entitled "Extended Timescale Atomistic Modeling of Crack tip Behavior in Aluminum," is published in *Modelling and Simulation in Material Science and Engineering* as indicated in the chapter. This work concentrates on adding accelerated molecular dynamics techniques to an existing spatial multiscale method, the Coupled Atomistic and Discrete Dislocation (CADD)

method. The study describes the effect of the loading rate on the deformation at a crack tip in aluminum, and evaluates the performance and efficiency of the combined multiscale method.

The fourth chapter, entitled "Examining the Mechanisms of Near Threshold Fatigue Crack Growth in Aluminum Alloys with Atomistic Simulations," uses CADD to study the effect of dislocation pileups caused by lattice resistance on fatigue crack growth mechanisms. The simulations reveal that increasing the lattice resistance causes the fatigue crack growth threshold to increase. Furthermore, several mechanisms are illuminated that cause fatigue crack growth in each cycle at nanometer scale. It is concluded that the spacing of obstacles to dislocation motion control the fatigue crack growth threshold in aluminum alloys. This work is currently in preparation for publication.

CHAPTER 2

SIMULATING DYNAMIC FRAGMENTATION PROCESSES WITH PARTICLES AND ELEMENTS

By Kristopher Baker and Derek H. Warner

As published in *Engineering Fracture Mechanics*, **84** (2012) 96–110

2.1 Abstract

The dynamic fragmentation of brittle materials has been extensively studied via experiment, analytic theory, and numerical modeling. While analytic theories capture specific aspects of the fragmentation process observed experimentally, numerical models can produce a wide range of results dependent upon their makeup. This study examines dynamic fragmentation using particle and clustered particle (continuum) simulation approaches. The fragmentation of 1D string, 3D bar, and 3D plate geometries are examined along with the effects of irreversible damage and initial temperature (defects). The results highlight three distinct physical processes that can play an important role in a dynamic fragmentation event: crack nucleation, free surface sublimation (phase changes), and crack branching. Each process leaves a signature with regard to the resulting fragment size distribution and can be affected by the numerical discretization of the system. The findings of this work are intended to provide general guidance with regard to modeling dynamic fragmentation.

2.2 Introduction

Dynamic fragmentation events occur across a broad range of scales. Examples span collisions of atomic nuclei [12, 14, 21, 30, 35], ballistic impact of ceramic armor [117], concrete structures subjected to blast loading [19, 57], asteroid impacts [69, 86], and the big bang [43]. The phenomenon has been intensively studied via experiment, analytic theory, and numerical simulation, with each approach having its own benefits and drawbacks. This work focuses on the numerical simulation of dynamic fragmentation, with the general goal of illuminating the interaction between the numerical model and the prevailing physical processes.

Dynamic fragmentation events are often characterized by their resulting fragment size distribution. Typically, experiments report power law fragment mass distributions,

$$pdf(m) \propto m^{\tau}, \tag{2.1}$$

where $pdf(m)$ is the probability of finding a fragment of mass m, and τ is the power law exponent. To reduce statistical noise, the distributions are commonly reported as complementary cumulative distributions,

$$ccdf(m) = 1 - \int_0^m pdf(x)\,dx \propto m^{\tau+1}. \tag{2.2}$$

Fragmentation events are primarily characterized by their average fragment size, m_{avg}, and the power law exponent associated with the distribution. The average fragment size is a function of the boundary conditions (loading) and material properties while the power law exponent is generally thought to be a more universal quantity that depends only on the active physical processes governing the event.

Macroscopic, dynamic fragmentation experiments of brittle materials like glass, plaster, ceramics, and clay, typically report power law exponents between -1.5 and -1.7 for 2D and 3D fragmentation events [52, 53, 78, 49, 51, 50, 68, 47, 114]. Some experimental efforts have reported exponents outside of this range, examples of which involve the fragmentation of sandwiched plates (-2) [53], egg shells (-1.3) [114, 115], and impact events (-1.1 to -1.3) [49]. Interestingly, atomic collisions also produce power law fragment mass distributions [12, 14, 21, 30, 35, 42]. However, the power law exponents measured from atomic scale fragmentation are noticeably larger (-2.1 [21] and -2.6 [42]) than those observed in macroscopic experiments.

Analytic modeling can provide insight into the physical origin of these exponents. In macroscopic fragmentation events involving brittle materials, models suggest that exponents of $\tau = -1.5$ (2D) and $\tau = -1.67$ (3D) can be attributed to crack branching and stress waves [68, 41, 54]. At the atomic scale, 3D percolation processes [14] and Fisher's critical droplet model [34] have been linked to power law fragment size distributions with exponents of $\tau = -2.2$ and -2.23 respectively, consistent with experiments of atomic scale fragmentation events.

Numerical simulations can provide insight beyond that which can be obtained from experiment and analytic theoretical analysis alone. As virtual experiments, one has full control over the material properties and boundary conditions, while being able to completely track the evolution of the system. The majority of simulations conducted in the literature have utilized particle methods where point masses or rigid shapes are connected with breakable springs or beams, e.g. discrete elements and molecular dynamics. Some work has been done with smooth particle hydrodynamics (distributed mass points evolving

with continuity constraints) using an added fracture criteria [11]. A significant number of these particle based studies suggest power law fragment distribution exponents consistent with macroscopic experiments and theory, reporting values near -1.5 and -1.67 [86, 41, 11, 5, 6, 7, 8, 18]. However some simulations involving circularly expanding systems report fragment distribution exponents ranging from -2 [57] to -1 [3] and simulations of impact events report exponents between -1 and -2.3 [58, 15, 88]. While simulations of 2D and 3D dynamic fragmentation events have been performed using finite element methods, we are not aware of any that report fragment distributions [19, 29, 70, 85, 65]. Although, there is a large body of work focused on 1D fragment distributions using finite element methods (see [63] and references therein).

A key challenge common to both particle and element methods when simulating macroscopic bodies is the discretization. If the discretization is not linked to physically meaningful objects (such as aggregates or grains in a microstructure with weak grain boundaries [65]), the result should be independent of the size of discretization. This presents a significant challenge in light of the power law fragment size distribution often associated with dynamic fragmentation events. Moreover, particle based simulations tend to produce a very large population of small fragments (consisting of only a few particles) independent of the volume that the particles represent [57, 43, 41, 18, 3, 88, 4, 27, 102]. These small fragments, which also appear to follow a power law distribution with a more negative slope [57, 41, 18, 3, 88, 27], are often ignored in the analysis [18, 88, 4, 27]. Finally, the principle ingredient associated with dynamic fragmentation, i.e. dynamic crack propagation, has been shown to not be convergent with mesh size in finite element simulations [73].

By simulating dynamic fragmentation events in several settings and employing two numerical approaches this work aims to shed light on these challenges and better illuminate the key phenomena associated with dynamic fragmentation. All simulations are performed within a molecular dynamics framework, which in its native form is a particle method. However, by clustering particles (atoms) together using combinations of breakable and unbreakable bonds, we also investigate dynamic fragmentation in the context of element based simulation methods [20, 46] where the smallest discrete unit can be rotated and strained.

This work highlights three distinct processes that can occur during a fragmentation event, with each having an influence on the fragment size distribution. Each of the processes interacts with the numerical discritization in a distinct way and is associated with fragmentation occurring under a specific range of conditions. Thus, the ability of the numerical model to simulate a fragmentation event accurately is a function of the physical processes which occur during the specific fragmentation event that is being modeled. The paper is organized according to the simulation geometry, i.e. 1D string, 3D bar, and 3D plate, with each section bringing added complexity and building upon the insights gained in the previous sections.

2.3 Methods

The simulations performed herein utilized the LAMMPS [83] molecular dynamics engine. Inter-particle forces were computed from the model potential [13],

$$\frac{d\phi}{dr}(r) = k(r - r_0)\left[\exp(r\frac{\Xi}{r_{break}} - \Xi) + 1\right]^{-1}, \tag{2.3}$$

where $\phi(r)$ is the potential energy, r is the distance between two particles, r_0 is the equilibrium spacing of the particles, k is the stiffness, r_{break} is the distance at which the bonds break, and Ξ is a smoothing parameter. For all simulations, we used: $k = 332$, $r_0 = 2^{1/6}$, $r_{break} = 1.2$, and $\Xi = 1,000$. This function is plotted in Figure 2.1. With $\Xi = 1,000$, the potential is nearly harmonic up to a separation distance of r_{break}, at which point it sharply transitions to zero, making it a good representation of a linear, brittle material. Thus, the energy to break a single bond, i.e. to stretch it from its equilibrium distance to the point at which its strength goes to zero, can be accurately approximated as $\epsilon_b \approx k(r_{break} - r_0)^2/2$, which for the parameters used here gives $\epsilon_b = 1.00$.

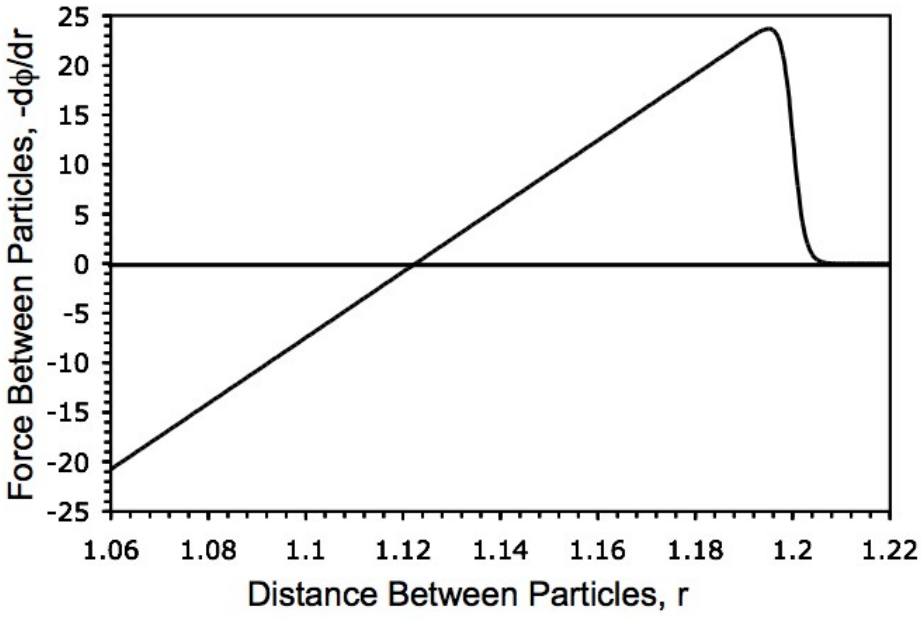

Figure 2.1: The interatomic potential used for all simulations is harmonic in tension and compression. When the particle separation reaches r_{break}, the bond force quickly drops to zero, simulating a brittle failure in tension. The purely repulsive potential used for the interaction of irreversibly broken bonds is simply the negative (compression) portion of this potential with the positive values (tension) set equal to zero.

To perform element-like simulations using LAMMPS, particles are clustered

using two pair potentials. The potential shown in Figure 2.1 is used to model the interactions between particles belonging to different clusters, while a similar, but unbreakable, pair potential is used for intra-cluster interactions. A diagram showing simple examples of this setup for 1D and 2D simulations is given in Figure 2.2. As indicated in the introduction, both reversible and irreversible bonding were examined, i.e. when a breakable bond was stretched beyond a length of r_{break}=1.2, the harmonic pair interactions were replaced by a purely repulsive potential with the same lattice constant and compressive stiffness.

A uniaxial strain was applied by expanding the simulation domain along the x-axis, while the domain size in the y and z directions remained fixed. Particles near the domain boundaries interacted with images of particles near opposite boundaries via periodicity in all three directions. The particles were assigned an initial, linear velocity profile of the form:

$$v(x) = \dot{\epsilon} x \tag{2.4}$$

where $\dot{\epsilon}$ is the uniaxial strain rate, and x is the coordinate in the pulling direction with $x = 0$ at the center of the sample. This initial velocity profile eliminates the creation of shock waves at time $t = 0$. The simulation cell boundaries in the x direction are moved with a constant velocity in the x direction. Fracture typically began at 3% strain and the simulations were continued to 200% strain to provide time for the fragment distribution to reach equilibrium. Three arrangements of particles were examined, i.e. a string of 20,000 particles in one dimension, a three-dimensional slender rod with a square cross section ($2 \times 2 \times 10,000$ unit cells with 160,000 atoms), and a three-dimensional, thin, square plate ($2 \times 200 \times 200$ unit cells with approximately 320,000 atoms). For the 3D rod and plate samples, the particles were arranged on a face centered cubic lattice as shown in Figure 2.3.

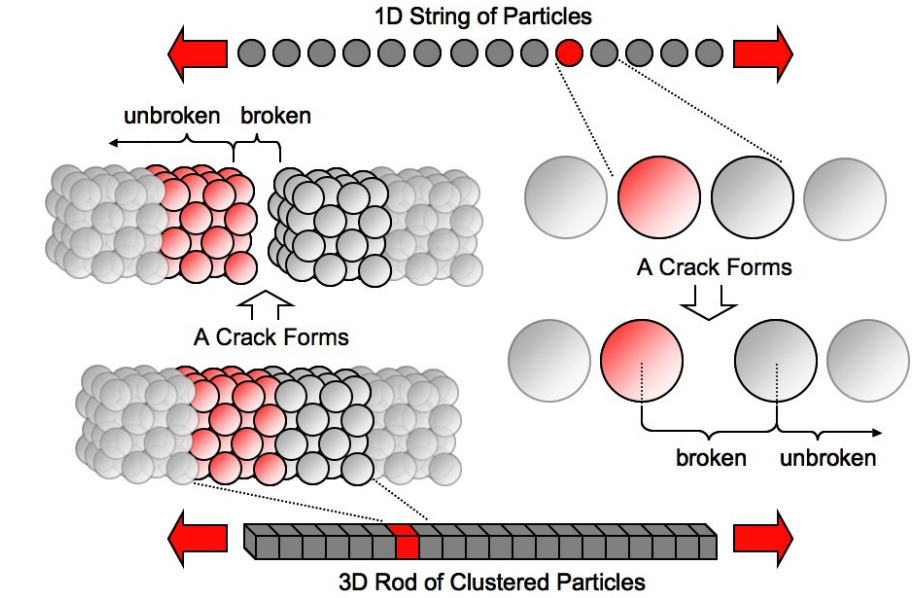

(a)

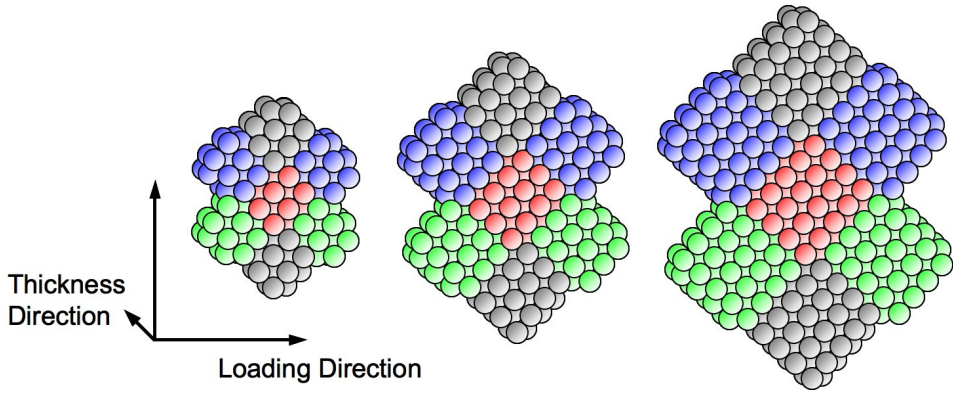

(b)

Figure 2.2: Cartoons of particle clustering, the technique used to vary the level of discretization. a) In this schematic, each cube in the 3D rod of particles is a single cluster. The boundary conditions remain the same, but the number of particles in each cluster is varied. Only bonds between clusters are allowed to break to form cracks. The 1D string of particles is the limit where the number of particles in each cluster is 1. b) In this 2D schematic diagram of cluster bonding, each particle is grouped by its color. Each particle interacts with its own color using an unbreakable potential, while interactions between two different colors use the breakable potential given in Figure 2.1. This configuration of bonds will allow cracking only between clusters of particles.

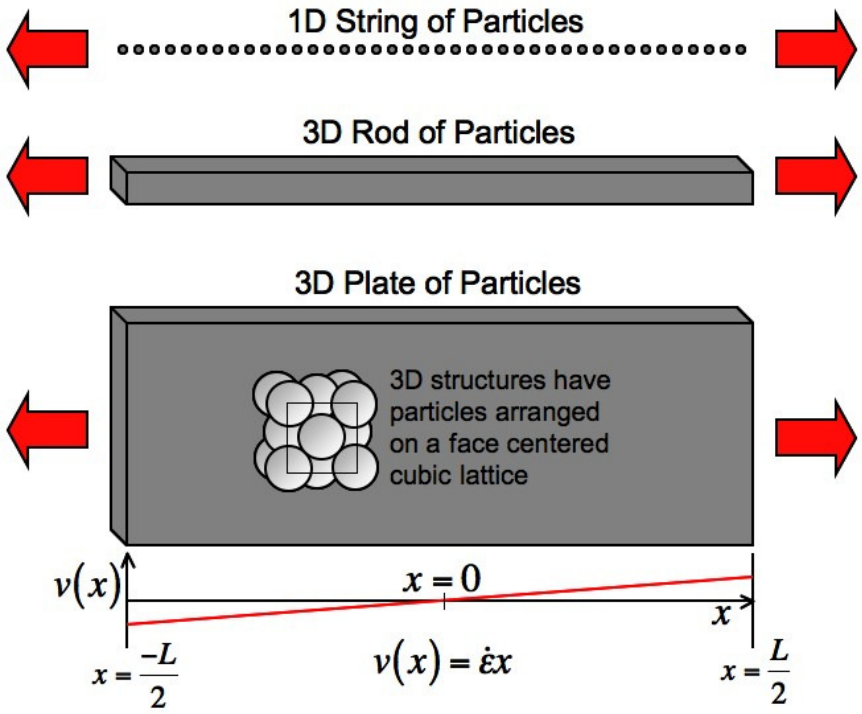

Figure 2.3: The 1D string, 3D rod, and 3D plate samples are all loaded in uniaxial tension. The direction of the load is indicated by the arrows. An initial velocity profile is added to remove initial stress waves, and the simulation boundaries perpendicular to the loading direction are moved with constant velocity $v = \pm\frac{\dot{\epsilon}L}{2}$, where L is the length of the sample in the x direction. The 3D bar and plate have particles arranged on a face centered cubic lattice aligned as shown in the diagram.

A small random velocity, v_r, generated from a uniform distribution, was initially applied to each particle to break symmetry. From a statistical mechanics perspective this is equivalent to as assigning an initial temperature to the system, $T = \overline{v_r}^2 m/3k_B$ where $\overline{v_r}$, m, and k_B is the instantaneous average particle random velocity, particle mass, and Boltzmann constant, respectively. In all simulations the specimens reach a thermal equilibrium within a few thousand steps after the initial velocities are applied. Thus, the equilibration process is complete before the sample is strained to one-tenth of its failure strain (1D string and 3D bar geometries), or is done before straining the sample (3D plate

geometry).

The choice of T can have a significant effect on the fragmentation process. If T is chosen to be small, all loaded bonds stretch nearly to their maximum allowable strain before fragmentation occurs. The large amount of stored strain energy transfers to a large amount of fracture energy and consequently leads to a large number of fragments. Increasing the initial value of T from zero increases the amount of thermal energy available to assist the nucleation of cracks, thus promotes the occurrence of fragmentation at lower strain energies leading to a smaller number of fragments. At high initial values of T, thermally activated crack nucleation becomes significant in that higher initial temperatures lead to a larger number of fragments, with the maximum stored strain energy playing a less significant role. The relationship between the equilibrated temperature (1/2 the initially assigned temperature) and the number of fragments created at 200% strain for an unclustered 3D plate simulation is shown in Figure 2.4. In general, for the simulations performed in this work, the initial temperature was chosen high enough to avoid extraordinarily high strain energies, but low enough to avoid the initial thermal energy resulting in excess fragment formation. For example, the majority of the 3D bar and 3D plate simulations were conducted at a temperature of $T = 0.360$. As a point of reference, surface sublimation of our model material occurs at $T = 0.571$.

For computational efficiency and universality, our simulations and analysis utilize unitless quantities, with the particle mass (m), the particle separation distance at which the interaction potential is zero (σ), the energy required to break a particle-particle bond (ϵ), and the Boltzmann constant set to unity. Thus the distances, energies, rates, and temperatures reported in this manuscript are

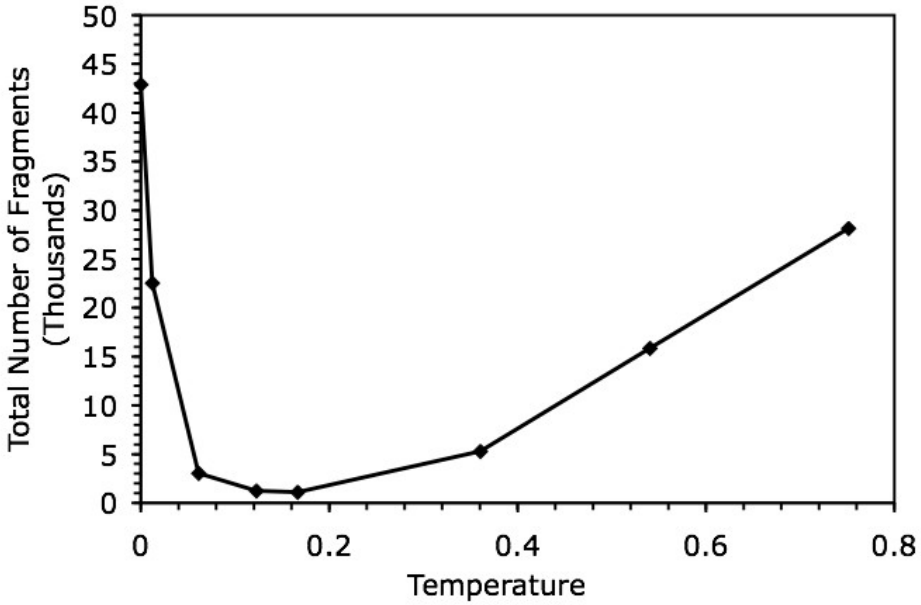

Figure 2.4: The total number of fragments with respect to the temperature, for fragmentation of the 3D plate. The strain rate and sample size are identical to the simulations described in the results section.

functions of σ, ϵ, and m for a given material of interest. For example, the reduced distances reported herein can be converted to standard units by multiplying by the value of σ for the material of interest.

For convenience, we provide several quantities relevant to our simulations in standard units in Table 2.1 for three popular materials: bulk PMMA, bulk silicon nitride, and Lennard-Jones copper. The Lennard-Jones copper parameters were directly extracted from the literature [45, 66], while the Silicon Nitride and PMMA parameters were derived from the finite element studies of Molinari et al. 2007 [73]. Specifically, m was taken to be the average mass of a finite element; ϵ was taken as the fracture energy release rate times the surface area of the average finite element, and σ was taken as a representative length (depending on the dimension) of an average finite element in Molinari et al. 2007 [73]. We note

that the loading rates are consistent with typical molecular dynamics loading rates and those used by Molinari et al. 2007 [73] in the case of finite element simulations. While the applied expansion velocity was well below the wave speed of the material in all cases, it was significant with respect to the specimen length scale and wave speed such that the loading can be considered dynamic.

Table 2.1: Simulation parameters with respect to three materials. (v_{exp} is the applied expansion velocity)

Material	Lennard-Jones Copper	PMMA	Silicon Nitride
σ (m)	2.277×10^{-10}	2.400×10^{-5}	5.000×10^{-8}
ϵ (J)	6.649×10^{-20}	2.262×10^{-2}	1.000×10^{2}
m (kg)	1.055×10^{-25}	5.383×10^{-7}	1.375×10^{-4}
T (^{o}K)	1834	-	-
T/T_{melt}	0.631	-	-
L (m)	2.277×10^{-6}	0.240	5.000×10^{-4}
$\dot{\epsilon}$ (1/sec)	1.026×10^{9}	2514	5.020×10^{6}
v_{exp} (m/sec)	1168	301.7	1255
v_{exp}/c	0.309	0.183	0.126

2.4 1D String

We begin by discussing the fragmentation of a 1D string of particles. The results primarily serve to provide a foundation upon which the 3D bar and 3D plate simulations can be better understood. Considering the 1D geometry, where crack branching cannot occur, a power law distribution of fragment size is not expected when elastic crack-crack interactions are not important [54]. In this limit the fragment size distribution can be simply modeled as a string independently cut in multiple random locations along its length. In this vein, both Mott

and Linfoot (1943) [74] and Grady and Kipp (1985) [37] have suggested modeling fragment creation as a continuous Poisson processes, with the probability of finding a fragment of mass, m, being

$$pdf(m) = \frac{e^{-m/m_0}}{m_0}, \tag{2.5}$$

where m_0 is the average fragment mass. Correspondingly the complementary cumulative fragment mass distribution can be written as

$$ccdf(m) = e^{-m/m_0}. \tag{2.6}$$

The 1D string simulation consisted of a uniaxial tensile load applied by moving the edges of the simulation cell with a constant velocity of $v = \pm\frac{\dot{\epsilon}L}{2}$, as shown in Figure 2.3. As stated in the methods section, an initial velocity profile was employed to avoid initial loading waves, and an initial random velocity distribution was utilized to break the symmetry of the lattice. The simulation was conducted to 200% strain. During the simulation, the motion of the particles were constrained to a single direction, and the string was periodic in only that direction. The strain rate was 2.94×10^{-4} and the equilibrated temperature was $T = 0.036$. We note that this temperature is one order of magnitude lower than what was used in the majority of the 3D simulations. The lower temperature was necessary to avoid thermally activated fragment creation in the 1D specimens.

The complementary cumulative distribution of fragment sizes associated with this simulation is shown in Figure 2.5. The distribution is measured at 200% strain, at which point it is stationary. The solid line in Figure 2.5 represents Equation 2.6 with m_0 set to the average fragment mass measured in the simulation, 3.0 particles per fragment. While the simulation results clearly fol-

low a linear exponential distribution, they do not quantitatively match Equation 2.6. We attribute this discrepancy to the fact that a significant portion of the fragment size distribution impinges on the particle size. The importance of this aspect, i.e. discrepancy between the continuous exponential fragmentation model and the discrete simulation, can be illuminated by considering a complementary cumulative geometric distribution, which is the discrete analog to the exponential distribution (Figure 2.5),

$$ccdf(m^D) = (1 - \frac{1}{m_0^D})^{m^D}, \tag{2.7}$$

with m^D and m_0^D being the discrete versions of the continuous variables m and m_0, where the mass of a single particle is 1. While the geometric distribution certainly corresponds more closely with the simulation data, a systematic discrepancy is present at large fragment sizes where the distribution predicts a larger population of large fragments. This difference is most likely due to dynamic effects inherent in the simulation, causing additional fractures due to elastic wave interactions with defects or each other [36].

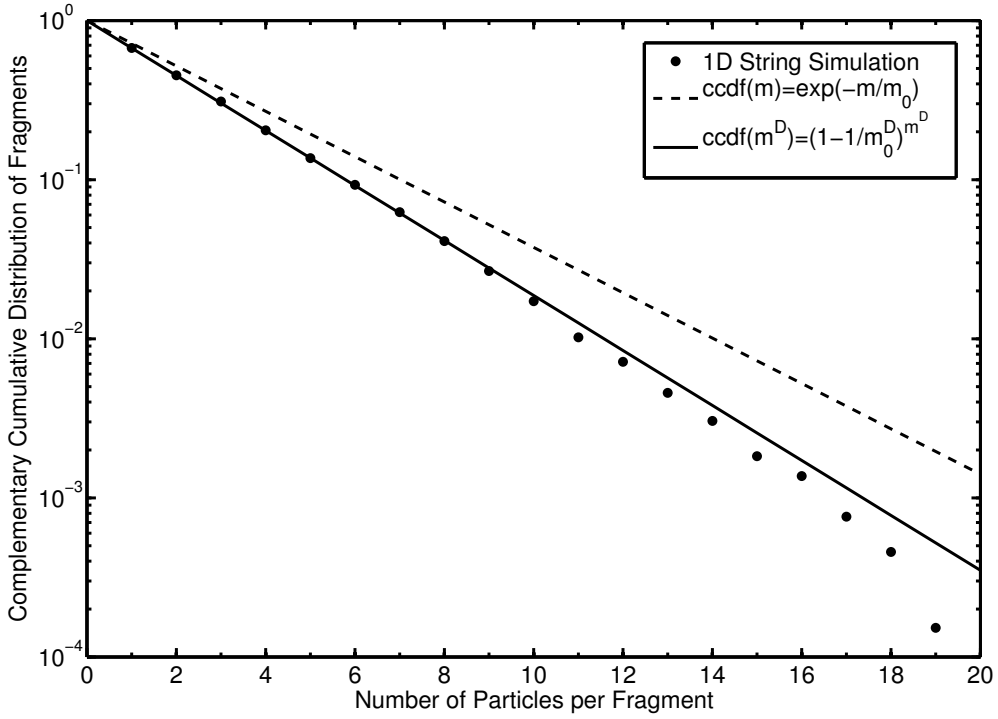

Figure 2.5: Complementary cumulative fragment mass distribution for a simulation of a 1D string of particles, compared to analytic theories of a line broken randomly along its length.

2.5 3D Bar

Analogous simulations were performed with a 3D bar of particles. The bar was composed of $2 \times 2 \times 10,000$ face centered cubic unit cells with a total of 160,000 particles. The strain rate was 2.94×10^{-4}. The effects of T, permanent damage (irreversible bond breaking), particle clustering, and cluster size were examined.

Clustered Particles

As shown in Figure 2.2a, particles were grouped into clusters such that a string of clusters existed along the bar length. In this way, the simulations represent a 1D string of clusters being pulled in uniaxial tension. Thus, when cracks formed during the simulation they were confined to locations between clusters, opening perpendicular to the loading direction, much like how cracks formed between the particles in the 1D string simulation. Simulations were performed with cluster sizes of 24, 52, 128, and 256 particles.

Figure 2.6 shows the complementary cumulative distribution of fragment masses for a set of simulations performed with various cluster sizes at an equilibrated temperature of T=0.360. For each cluster size, two separate simulations were performed and the averaged result of the two is reported. In the figure, the fragment mass is normalized by the average fragment mass, which ranged from 3,810 to 4,638 particles, significantly larger than the maximum cluster size that was examined. Equation 2.6 is plotted for comparison. For fragment sizes below 2 times the average fragment size, the process is described very well by Equation 2.6. In accordance with the discussion in the previous section, this result can be attributed to the average fragment size being significantly larger

than the cluster size. Thus, the portion of the fragment size distribution that experiences finite cluster size effects is insignificant with regard to the important characteristics of the process such as the mean fragment size or total surface area. Fragment sizes above 2 times the average fragment size do not correspond well with Equation 2.6. This discrepancy qualitatively coincides with that observed for the 1D string. In both cases the behavior is not thought to result from specimen boundary effects, but most likely from large fragments fracturing by dynamic waves interacting with the defect structure in the bar [36].

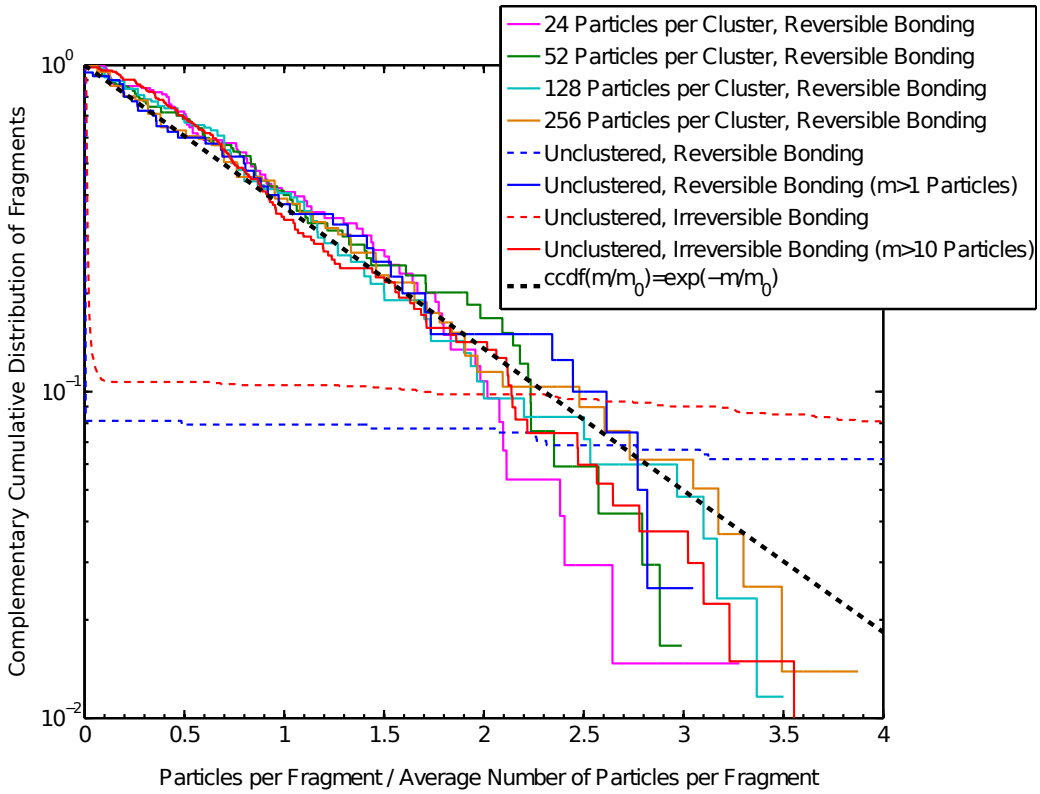

Figure 2.6: Complementary cumulative fragment mass distribution, as a function of the normalized fragment mass, for simulations of a 3D bar in uniaxial tension divided into clusters. The fragment mass is normalized by the average fragment mass. The complementary cumulative distribution for the unclustered simulations, and equation 2.6, are plotted for comparison.

Over the range of the cluster sizes examined here, i.e. cluster lengths at least

40 times smaller than the average fragment size, cluster size did not appear to influence the fragmentation process, both with respect to the number of fragments (and fracture energy) and the distribution. Considering that the process can be described fairly well with an exponential distribution, this result is consistent with computing the expected fragment size from the distribution, i.e. the expectation integral is insensitive to its lower bound between values of zero and $\approx 10\%$ of the average fragment size. This conclusion is in agreement with that of Molinari et al. (2007) [73] who suggested a discretization size at least one order of magnitude below the average fragment size to achieve numerical convergence in 1D. However, we note that the 1D fragmentation events studied by Molinari et al. (2007) [73] did not follow a linear exponential distribution below the mean fragment size.

Unclustered Particles

A 3D bar simulation was conducted with the cluster assignments removed so that a particle was the smallest discrete unit. The fragment distribution from the unclustered particle simulation was found to differ significantly from what was observed in the clustered particle simulations in that there was a large population of single particle fragments as shown in Figures 2.6 and 2.7. Interestingly, if the single particle fragments of the unclustered simulation are ignored, the fragment distribution can again be well described with a linear exponential distribution, consistent with a Poisson process (Figure 2.6). Moreover, the average fragment size of the multi-particle fragments was consistent with the average fragment size in the clustered simulations, i.e. $4,210$ particles per fragment. This suggests that the mechanism responsible for the multi-particle fragment

distribution is the same whether the particles are clustered or not. Thus, it is reasonable to assume that the primary difference between the fragmentation event in the unclustered and clustered particle simulations is the operation of an additional mechanism that leads to the formation of a large population of single particle fragments in the unclustered simulations.

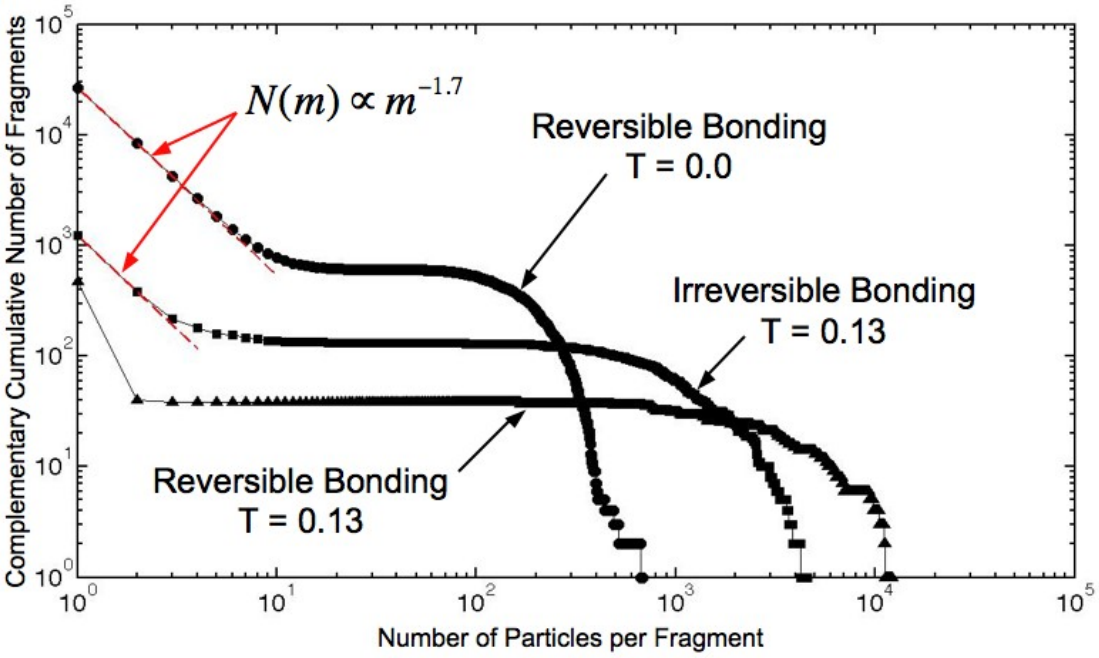

Figure 2.7: Complementary cumulative number of fragments as a function of the fragment mass for simulations of an unclustered 3D bar in uniaxial tension simulated with and without irreversible bonding, or with T=0.0 (no defects).

An explanation for this behavior can be formulated by considering the uncorrelated nonexpansive kinetic energy in the system as the primary culprit for the creation of single particle fragments within a thermal activation context. In this vein, the most significant difference between the clustered and unclustered simulations is that the energy required to create the smallest fragment in the unclustered simulations is significantly less than that in the clustered simulations, i.e. an isolated particle resting on a [100] surface can be decohered to create a

fragment with only 1/8 of the energy required to decohere the cross-section of the 3D bar. Considering the nonexpansive uncorrelated kinetic energy after the bar begins to fragment ($T = 0.416$) and the amount of energy, E_{coh}, required to remove single isolated particles from a [100] surface (4.00 from breaking of 4 bonds), the presence of many single particle fragments (but not single cluster fragments, which have a cohesive energy of 32.00 from breaking of 32 bonds) can be justified via thermal activation, $\propto e^{E_{coh}/k_B T}$.

This explanation hinges on the assumption that the fracture surfaces created when the large particles fragment are not smooth [100] surfaces. The energy to eject the first particle from a perfect [100] surface is 8.00 (from breaking 8 bonds), a value that implies that such an event would be extremely rare considering the thermal energy present in the simulation performed here. Thus, the creation of rough fracture surfaces via dynamic instabilities in the initial fracture process during the creation of large fragments is key. Figure 2.8 shows an image captured during the unclustered particle simulation that supports this hypothesis. While dynamic fracture instabilities are necessary for single fragment creation, we have not been able to resolve whether the majority of single particle fragments created in this simulation were the result of the dynamic fracture instability itself or the ejection of single particles from rough fracture surfaces, or a combination of the two.

To gain deeper insight into the fragmentation process associated with the 3D bar simulations examined here, the effect of irreversible bond breaking was studied in an unclustered particle simulation by replacing the interaction potential of broken bonds with a purely repulsive potential. First, irreversible bond breaking is found to not influence the character of the fragment size distribu-

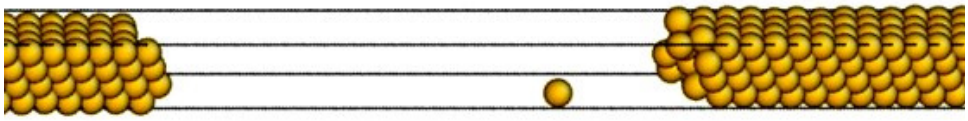

Figure 2.8: Snapshot during 1D bar fragmentation process with unclustered particles. Note the rough fracture surface and the single particle fragment that was created.

tion. Fragments of more than 10 particles follow a linear exponential size distribution. However, the average size of these large fragments (1,203 particles) is significantly smaller than in the corresponding simulation without irreversible bond breaking (Figure 2.6 and 2.7). This suggests that irreversibility is similar in effect to increasing the strain rate, i.e. it changes the mean of the fragment size distribution but does not change its character [43].

In contrast to the unclustered, reversible bonding simulation, the irreversible simulation showed significant populations of not only single particle fragments but also fragments composed of two and three particles. Moreover, the population of these smallest fragments was still evolving at 200% strain, whereas all the previous simulations reached a steady state with regard to the fragment distribution. At 200% strain the population of fragments consisting of less than 1000 particles per fragment continued to increase, while the population of the larger fragment sizes continued to decrease.

As an additional point of reference, a reversible unclustered simulation was performed with $T = 0.0$. The complementary cumulative fragment size dis-

tribution is shown in Figure 2.7. As with all the unclustered simulations, the distribution shows two populations of fragments. The small fragments with fewer than ten particles per fragment follow a power law distribution with the same exponent as the unclustered irreversible damage simulation. However in this case, the large fragment distribution cannot be well characterized by a linear exponential distribution or a power law distribution. Instead, the large fragment distribution is similar to that observed by Molinari and coworkers [62, 116, 118, 117] who examined the dynamic fragmentation of a 1D linear elastic line with cohesive element methodologies,

$$ccdf(m) = N_0 \exp\left(-\left(\frac{m - m_{min}}{m_0}\right)^2\right) (m > m_{min}). \tag{2.8}$$

The large fragment distribution from the $T = 0.0$ simulation is fit with $N_0 = 607$, $m_{min} = 25$, and $m_0^2 = 36,000$, as shown in Figure 2.9.

The source of the difference in fragment size distributions between the $T = 0$ simulation and the finite T simulations can be attributed to the absence of thermal fluctuations at $T = 0$. At $T = 0$ the strain energy can build to a significantly higher level before fragmentation ensues, relative to the finite temperature simulations. The increased amount of stored strain energy results in a more energetic fragmentation event that produces a smaller average fragment size relative to the finite T simulations. With the decreased fragment size, one expects increased dynamic interactions between neighboring cracks. However, this increased interaction does not appear to be the cause of the non-exponential (or geometric) distribution at $T = 0$, as the fragment distribution of the finite T 1D string simulations was accurately described by an exponential distribution, even though the average fragment size was very small (3 particles per fragment).

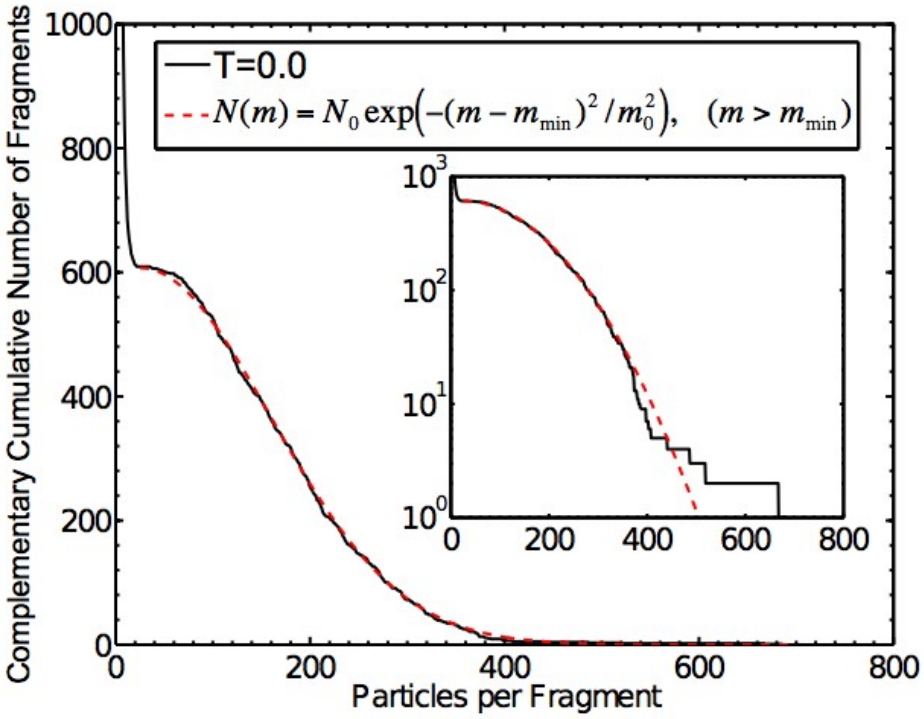

Figure 2.9: Complementary cumulative number of fragments for the simulation of a 3D bar in uniaxial tension with T=0.0 (no defects), reversible bonding, and unclustered particles. The data is plotted with Equation 2.8. The subfigure is the same data plotted on semi-log axes. Note that Equation 2.8 was not fit to the small fragment distribution (fragments smaller than 20 particles).

The difference in the $T = 0$ and finite T fragment size distributions is more likely due to the wide distribution of pre-stretched bonds present in the finite T simulations resulting from thermal fluctuations. Following standard statistical mechanics arguments, the effective bond length at finite T is distributed normally with a standard deviation of $\sqrt{kk_bT}$. As the load increases in the finite T simulations the rate of crack nucleation slowly increases from zero in accordance with a normal distribution of defect strengths. This is in contrast to the $T = 0$ simulation where a large number of cracks nucleate almost simultaneously once a critical load is reached. While the physical mechanism that connects crack nucleation rate and the resulting fragment size distribution is

not yet apparent, the existence of such a link is supported by other results in the literature such as the 1D fragmentations studies of Molinari and coworkers [117, 63, 62, 116, 118]. Molinari's studies repeatedly have resulted in fragment size distributions consistent with Equation 2.8 for a wide range of simulation parameters. However, in all of their studies the defect strength distributions have sharp rises in the defect population with increasing strength, relative to the effective normal distribution of defect strengths that is present in the finite T simulations performed in this work.

For both the $T = 0.0$ reversible simulations, and the irreversible bond breaking simulations, the distribution of the smallest fragments followed a power law distribution with an exponent of $\tau = -2.7$. This distribution of the smallest fragment sizes contrasts the previously given explanation of their formation via a random thermal activation process, i.e. $\propto e^{E_{coh}/k_B T}$. Often power law mass distributions are taken as indicators of a continuous phase change [14, 21, 6, 58, 38, 80, 97] or a first order phase change (like sublimation or melting) influenced by finite size effects [21, 38, 80]. In the former case of a continuous phase transformation, physical and numerical experiments and percolation theory suggest a power law exponent of near -2.2 [14, 21, 38, 80]. In the case of a first order phase transition influenced by finite size effects, power law mass distributions with exponents between -2 and -∞ are expected depending on the temperature and density of the system [80]. The observed power law exponent of $\tau = -2.7$ in the simulations presented here is consistent with these results [80], and thus may suggest that the formation and evolution of the smallest fragments could be consistent with phase change processes, i.e. surface sublimation.

2.6 3D Plate

A set of 3D plate simulations was performed that paralleled the 3D bar simulations of the previous section. The simulation geometry consisted of $200 \times 200 \times 2$ face centered cubic unit cells with a total of $\approx 320,000$ particles subjected to uniaxial tension. Due to the reduced length of the specimen in the loading direction, necessitated for computational feasibility, a higher strain rate (2.94×10^{-3}) relative to the bar simulations was required so that a sufficient population of fragments would be created. The effects of permanent damage (irreversible bond breaking), particle clustering, and cluster size were examined.

The dynamic fragmentation of the plate geometry can involve multiple additional physical processes beyond those possible in the bar. In the plate geometry, material decohesion involves crack orientations and stress concentrations. This allows separately nucleated cracks to directly interact and intersect. It also means that crack nucleation location does not necessarily control fragment size, as it does for in the bar geometry. Furthermore, cracks can branch and create fragments without interacting with separately nucleated cracks [13, 1, 119]. By considering the results of this section in light of the previous section where these mechanisms could not occur, one can better understand their importance during a dynamic fragmentation event.

2.6.1 Clustered Particles with Reversible Bonding

Clusters of particles were created in the 3D plate simulations using two interaction potentials designed to produce a homogeneous, brittle, linear elastic solid,

where cracks can only grow between clusters, analogous to the bar simulations. Simulations in this section were performed with clusters constructed from 24, 48, and 80 particles per cluster. The clusters extended through the thickness of the plate and were self-similar in shape (Figure 2.2). The shape of the clusters will affect the crack paths in a similar manner to the particle lattice in a particle simulation. In this case, vertical and horizontal cracks will have to follow a zig-zag path to grow, while diagonal cracks will have smooth surfaces with small steps. These details can be seen in Figure 2.10.

The plate of clustered particles acted like an infinitely thick, 2D, continuous system until failure, at which point cracks nucleated, grew, and created fragments throughout the plate. In contrast to the bar geometry, the largest fragments did not span the specimen width. Rather cracks coalesced on a length scale significantly smaller than the specimen width (Figure 2.10). Thus, the formation of the largest fragments can be attributed to a distinctly different mechanism in the plate simulations. Nonetheless, the length scale over which separately nucleated cracks intersect or coalesce is a function of the density at which cracks nucleated and therefore could potentially be describable within the context of a Poisson process [37]. However, this point could not be assessed in the current work due to the limited plate dimensions that were required considering our limited computational resources (a 3D plate simulation took approximately 15 hours with 36 2.66 GHz Intel Xenon quad core processors and InfiniBand connections).

The stationary complementary cumulative distribution of fragments, recorded at 200% strain, is shown in Figure 2.11a. For each cluster size, the data is averaged from three separate simulations. Fragments with fewer than 1,000

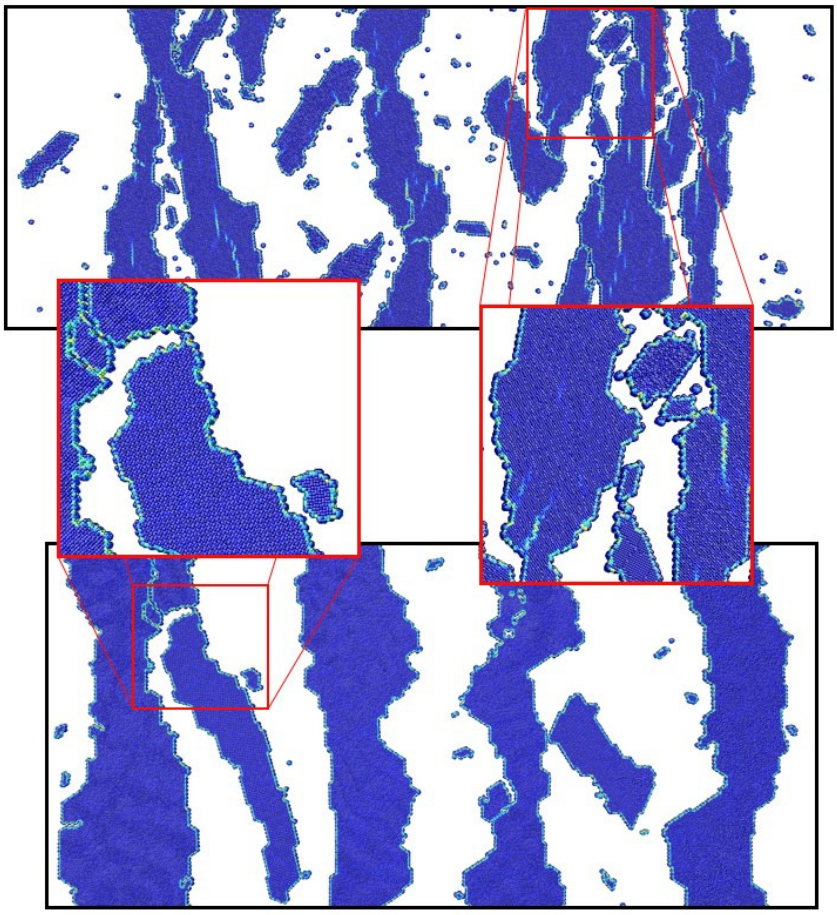

Figure 2.10: Two images of 3D plates fragmenting. The top picture is a simulation with 24 particles per cluster and irreversible damage. The bottom picture is a simulation with 24 particles per cluster with reversible damage. The enlarged sections of the images show the affect of the discretization on the crack paths and the range of fragment sizes. The color of each atom is determined by its local von mises shear strain invariant [64], and is helpful in showing interior cracks surfaces and the separation of nearby fragments.

particles can be described well with a power law distribution with an exponent of $\tau = -1.3$. While this value certainly falls within the wide range of values reported in the literature when using discrete element and molecular dynamics methods (from $\tau = -1$ [3] to $\tau = -2.3$ [58]), it is different than the value of -1.5 often observed in experiment and predicted from crack branching theory.

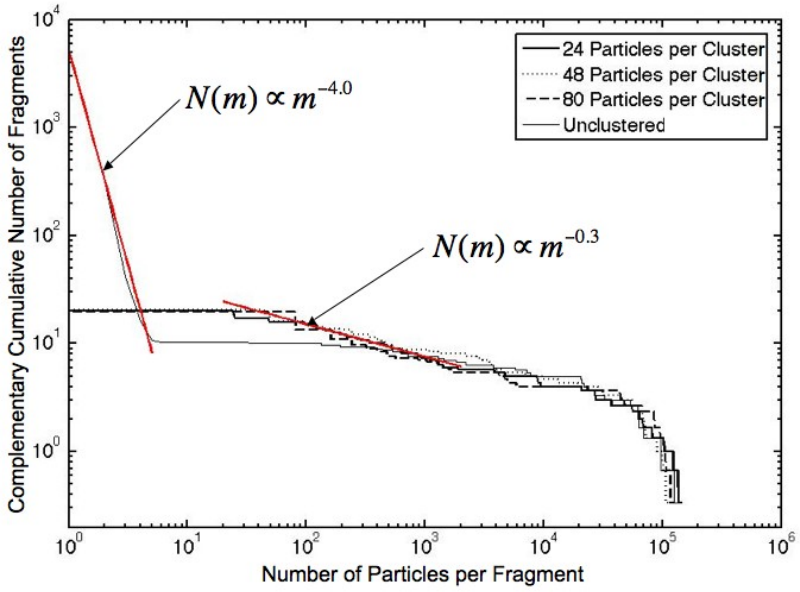

(a)

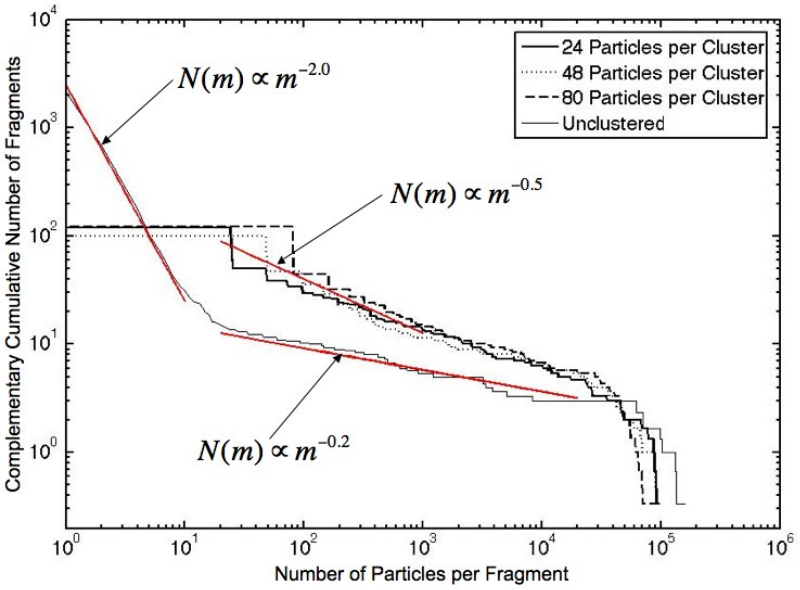

(b)

Figure 2.11: a) Complementary cumulative number of fragments for the simulation of a 3D plate in uniaxial tension simulated with reversible bonding, and b) irreversible bonding.

Interestingly the shape of the complementary cumulative distribution and average fragment size do not seem to be correlated with the cluster size. The average fragment size over the three simulations performed for each cluster size (24, 48, and 80 particles) were 15,681, 15,328, and 16,596 particles respectively. Considering the power law nature of the fragment size distribution, a converged average fragment size is unexpected. It was observed in the simulations due to a localized deviation from the power law distribution in the population of the smallest possible fragments. It should be emphasized that the average fragment size (or total number of fragments) to which the three cluster sizes examined converge does not seem to have physical significance; and, it is unclear if cluster sizes outside of this range would also converge to the same value based on the data in Figure 2.11a. Accordingly, in the following section we examine the limit of the cluster size equaling the particle size.

2.6.2 Unclustered Particles with Reversible Bonding

Three analogous plate simulations were performed without particle clustering. In these simulations the fragment size distribution did not reach a steady state at 200% strain as was observed in the 3D bar example with $T = 0.0$ and the 3D bar example with permanent damage. Accordingly the reported results correspond to a still evolving distribution at 200% percent strain (Figure 2.11a). As with the 3D bar simulations, the unclustered plate simulations also displayed a distinct population of small fragments (less than 5 particles per fragment). At 200% strain, no fragments existed between 5 and 300 particles per fragment.

The fragments consisting of less than 5 particles per fragment followed a

power law mass distribution with a slope of $\tau = -5.0$. In this way, the existence of these fragments is consistent with the occurrence of a first order phase transition subjected to finite size effects [80], as was observed and discussed for the fragmented bar simulations. The power law distribution of the smallest fragments suggests that their formation cannot be explained as a thermally activation process as pointed out earlier. Nonetheless, the occurrence of a large population of very small fragments and the slope of the distribution is still expected to be a function of E_{coh}, as a large population of small fragments was not observed in the clustered particle simulations.

The absence of fragments having between 5 and 300 particles in the unclustered simulations suggests that fragments with less than $\approx$ 300 particles either do not form, are not stable, or re-bond with other fragments. Being unable to unequivocally identify the source of this feature, we merely list three potential sources. First, due to crack tip length scale effects, the energy associated with smaller fragments formed via crack branching would be expected to have higher energies than larger fragments. Thus, the smallest particles with the highest energies are more susceptible to breaking down. Second, finite size effects and the increased surface to volume ratio of small fragments would make smaller fragments more susceptible to further decomposition, akin to melting point depression (Gibbs-Thompson effect). Third, the increased surface to volume ratio of small fragments coupled with the surface dissolution phenomenon discussed in the previous paragraph suggests that small fragments (5 to 300 particles) may dissolve into very small fragments (< 5 particles) which may then be absorbed by larger fragments (Ostwald ripening) or contribute to the small fragment distribution. While the latter two phenomena would also be expected to occur in the bar and string simulations, no evidence of such events

was observed, however, the lack of a power law fragment size distribution in these simulations already implies the existence of fewer small fragments capable of undergoing these effects.

While the formation of very small fragments, and the phenomena associated with it, clearly impacts the distribution of small fragments (consisting of fewer than $\approx$ 300 particles), it does not significantly influence the exponent of the power law distribution of larger fragments over the range of fragment sizes which it is meaningful to compare (300 to 20,000 particles per fragment). However, the unclustered particle simulations do show an increased population of larger fragments up to the point at which the populations of these fragments deviates from the power law distribution. Interestingly this suggests that the formation of the very small fragments in the unclustered particle simulations may affect crack branching behavior and thus has an effect on the large fragment population.

Irreversible Bonding

Simulations with irreversible bond breaking were performed both with clustered and unclustered particles. Again, the fragment distribution of unclustered particles changes in time, so the complementary cumulative fragment mass distribution at 200% strain is shown in Figure 2.11b. In general, irreversible bond breaking does not allow any opening created during the fragmentation event to heal, and ultimately results in the creation of more fragments of all sizes. The unclustered particle simulation with irreversible bonding produced a power law fragment size distribution for the large fragments of $\tau = -1.2$. Consistent with all previous simulations, small fragments consisting of less than 10 parti-

cles followed a separate power law distribution with a strongly negative exponent, $\tau = -3.0$, closely resembling the corresponding bar simulation $\tau = -2.7$. Interestingly, these two distributions are not separated by a range of fragment sizes over which no fragments exist as in the corresponding reversible damage case. This result contradicts the arguments given in the previous section regarding the instability of fragments smaller than ≈ 300 particles, and suggests an alternative explanation (like re-bonding of small fragments) for the lack of fragments with that range of sizes.

The complementary cumulative number of fragments at 200% uniaxial strain is shown in Figure 2.11b for clustered particle simulations with irreversible bond breaking. Qualitatively the fragment size distribution is not affected by the irreversibility. As with the reversible bonding simulations, the total number of fragments created (and thus the average fragment size) are not affected by cluster size due to a localized deviation in the power law distribution where the fragment size approaches the cluster size. Interestingly there is a distinct difference in the exponent of the power law distribution relative to the reversible bond breaking case. The exponent for these simulations, $\tau = -1.5$, matches macro-scale experiments and the predictions of 2D analytic theories. This better correspondence with macro-scale experiment and theory is not surprising considering that crack healing is unlikely in macroscopic experiments and that it was not included in the theoretical models that are cited. Moreover, the power law exponent associated with the large fragment population resulting from a 2D fragmentation event has been observed to become more negative with increasing amounts of energy input energy [3, 18, 88]. This is consistent with Figure 2.11 considering the assertion that we make here, that simulations with irreversible bond breaking differ from reversible bonding simulations similarly to

increasing the input energy between two simulations. Finally, we highlight that the current results, which correspond well with existing experimental data and theory, are only achieved in the clustered particle simulations where the phase change (sublimation) surface phenomenon is suppressed. This clearly shows that the smallest fragments in the unclustered simulations affect the entire distribution of fragments.

We confirm that the exponent $\tau = -1.5$ corresponds to crack branching phenomena by performing a similar set of simulations (clustered particles with irreversible damage), but with an initial large vertical crack in the center. The crack acts as a critical flaw, limiting the nucleation of other cracks throughout the plate. Upon loading the center crack grows, branches, and connects with itself across the periodic boundaries. Accordingly the fragments that are produced in this simulation are solely the result of crack branching phenomena. The stationary complementary cumulative distribution of fragments is plotted (recorded at 100% strain) in Figure 2.12 along with the distributions from the fragmented plate. The cracked plate simulation produces a fragment size distribution with the same power law exponent, $\tau = -1.5$, as the fragmenting plate, experimental measurements, and crack branching theories.

2.7 Discussion

The simulations conducted in this work have illuminated three distinct physical processes that control the fragment distribution created during a dynamic fragmentation event: crack nucleation, free surface sublimation (phase changes), and crack branching. The relative significance of each of these processes in

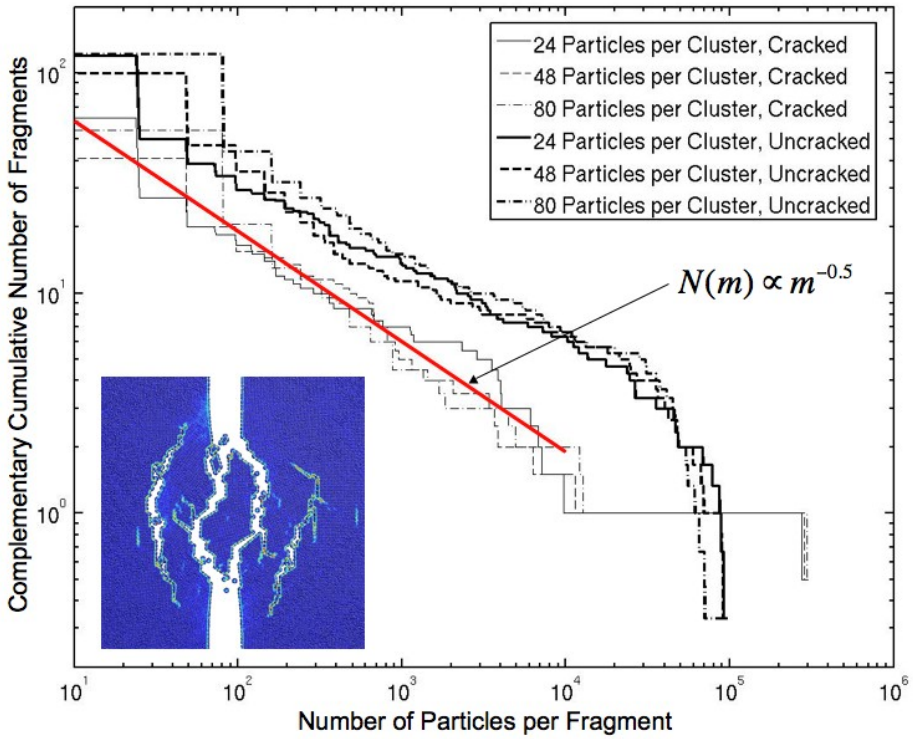

Figure 2.12: Comparison of complementary cumulative fragment mass distributions of a fragmented plate and a plate that had a single initial crack, both with irreversible bonding. The fragment distribution associated with the initially cracked plate has a power law exponent of $\tau = -1.5$ for nearly all of its range, while the fragmenting plate shows the same power law exponent for fragments below ≈ 1000 particles per fragment. The inset shows a snapshot of the cracked plate at 8% strain using 24 particles per cluster.

the resulting fragment size distribution is controlled by the material properties, boundary conditions, and discretization associated with the simulated fragmentation event.

At finite T, the 1D string and clustered particle 3D bar simulations produced fragment size distributions consistent with a Poisson fragmentation process. Accordingly the fragment distribution is well described by a geometric distribution, which in the limit of the particle size being small relative to the

expected fragment size, can be accurately approximated with a linear exponential distribution. The Poisson process fragmentation model did break down for fragments considerably larger than the mean size, where an upper limit on fragment size was observed. A quantitative analytic explanation of this upper limit remains an outstanding question. At $T = 0$, the 3D bar simulation did not produce a linear exponential or geometric fragment size distribution, but rather a distribution with a minimum fragment size. This difference in response, relative to the finite T simulations, was attributed to the simultaneous nucleation of a large population of cracks at the critical load and was consistent with other studies in the literature where the material defects strength distribution sharply increases from zero with increasing strength.

In 2D, the plate geometry differed in that fragmentation did not occur via nonintersecting cracks extending across the domain. Rather fragments were formed via the branching and coalescence of separately nucleated cracks. In accordance with analytic theories and experiments, the primary character of the fragment size distribution was observed to be a power law. The population of the largest fragment sizes deviated from a power law distribution, but insufficient statistics were acquired to determine if this part of the distribution can be described by a linear exponential distribution, which might be expected when considering the coalescence of separately nucleated cracks.

Both the bar and plate simulations produced a distinct population of very small fragments when particles were not clustered, i.e. the smallest possible fragment size was a single particle. We proposed that the occurrence of this phenomenon is linked to the cohesive energy associated with small fragment creation. In other words, a large population of small fragments was not formed

in the clustered particle simulations because the energy required to form the smallest fragment is significantly greater than that required to form single particle fragments. In the plate simulations where the highest energies are associated with stress concentrations at crack tips, the length scale associated with cluster decohesion is also hypothesized to be intertwined in this effect. The distribution of the very small fragments was consistently found to follow a power law distribution with an exponent between $\tau = -2$ and $-\infty$, which parallels first order phase transition physics with finite size effects. Nonetheless, a quantitative understanding of this phenomenon is also an outstanding question.

The component of the fragment size distribution associated with a linear exponential (or geometric) distribution occurring in 1D fragmentation events can accurately be captured with a discretized numerical simulation. Specifically, if the level of discretization is one order of magnitude below the mean fragment size the energy associated with the fragmentation event and mean fragment size can be expected to quickly converge as the level of discretization is refined. However, the component of the fragment size distribution associated with the formation of very small fragments following the power law distribution does not bode well for numerical simulation when the level of discretization cannot be connected to the structure of the material. For 1D fragmentation events, we found that ignoring the very small fragments will not influence the distribution of the larger fragments, and thus may be an acceptable approach in some circumstances. However for fragmentation events that involve crack coalescence and branching, the formation of very small fragments influences the population of the larger fragments by affecting crack tip behavior. Thus, the discretization of such simulations must be linked to the relevant material length scale. This is true even when not considering the production of a large population

of small fragments due to the power law fragment distribution associated with crack branching. While the mean fragment size and fragmentation energy were shown to be convergent when the very small fragment creation was suppressed in the clustered particle simulations, the physical meaning of the converged values is not clear. A future investigation that probes the existence of a potential linkage between crack tip energy and length scale would be very valuable in this regard.

With respect to the dynamic fragmentation process in general, we have found that irreversible bond breaking leads to a smaller average fragment size but does not significantly influence the fragment size distribution (noting that the power law exponent of the clustered particle plate simulations increased with irreversible bond breaking). In this way, comparing a reversible bond breaking simulation with an irreversible bond breaking simulation is analogous to comparing a fragmentation event conducted at lower energies with one conducted at higher energies. Additionally, we find that the initial temperature non-monotonically affects the resulting mean fragment size of a fragmentation event. Initial increases in temperature from zero decrease the maximum capacity of strain energy that the material can store before fragmentation commences, which consequently leads to an increased mean fragment size. However, at higher temperatures, increases in initial temperature act primarily to thermally assist fragmentation.

2.8 Conclusions

In general, the simulation of dynamic fragmentation events presents a substan-

tial challenge due to interactions between the artificial length scale associated with the discretization of the model system and the underlying physical processes. Two and three dimensional geometries present substantial challenges due to the power law fragment size distributions that result from crack branching and surface sublimation phenomena. A prevailing challenge associated with modeling fragmentation in any number of dimensions is surface sublimation. In 2D, we find that ignoring this small scale phenomenon, via coarse discretization, can artificially influence the fragment distribution at larger scales by interfering with crack tip behavior. In 1D, ignoring surface sublimation, via coarse discretization, may be a practical solution as it was not found to influence the distribution of large fragment sizes. In the absence of surface sublimation, 1D fragmentation events can be fully resolved if the physics dictates a minimum fragment size, as is the case when the material defect population sharply increases from zero with increasing strength. In cases where this does not occur, 1D fragmentation events generate an exponential fragment size distribution and are amenable to numerically convergent modeling with respect to average fragment size and energy dissipation, while the population of fragments below the scale of the discretization is discarded.

CHAPTER 3

EXTENDED TIMESCALE ATOMISTIC MODELING OF CRACK TIP BEHAVIOR IN ALUMINUM

By Kristopher Baker and Derek H. Warner

As published in *Modelling and Simulation in Material Science and Engineering*, **20** (2012) 065005

3.1 Abstract

Traditional molecular dynamics (MD) simulations are limited not only by their spatial domain, but also by the time domain that they can examine. Considering that many of the events associated with plasticity are thermally activated, and thus rare at atomic timescales, the limited time domain of traditional MD simulations can present a significant challenge when trying to realistically model the mechanical behavior of materials. A wide variety of approaches have been developed to address the timescale challenge, each having their own strengths and weaknesses dependent upon the specific application. Here, we have simultaneously applied three distinct approaches to model crack tip behavior in aluminum at timescales well beyond those accessible to traditional MD simulation. Specifically, we combine concurrent multiscale modeling (to reduce the degrees of freedom in the system), parallel replica dynamics (to parallelize the simulations in time), and hyperdynamics (to accelerate the exploration of phase space). Overall, the simulations (1) provide new insight into atomic-scale crack tip behavior at more typical timescales and (2) illuminate the potential of com-

mon extended timescale techniques to enable atomic-scale modeling of fracture processes at typical experimental timescales.

3.2 Introduction

The domain of traditional molecular dynamics (MD) simulations of materials is limited in both the temporal and spatial dimensions. The spatial scale is limited by the number of atoms in the simulation, while the temporal scale is limited by the small time step required to accurately capture atomic vibrations. With current computational resources and algorithms, these limitations usually restrict traditional MD simulations of materials to nanometer sizes and, at most, nanosecond timescales. Thus, MD modeling of materials with defects, e.g. cracks and dislocations, can present a significant challenge when the defects are associated with long-range stress fields and evolve via thermal activation (are controlled by events that are rare on atomic time scales).

In studies concerning a spatially localized region of interest, e.g. investigations of crack tip behavior, concurrent multiscale modeling can be a valuable tool to help alleviate temporal and spatial scaling challenges. By utilizing a more computationally efficient modeling framework, such as continuum mechanics, in regions away from the key area of interest, a multiscale approach often requires significantly fewer degrees of freedom relative to an equivalent fully atomistic simulation. By reducing the degrees of freedom and resulting computational expense, multiscale methods provide two distinct benefits. The first is that significantly larger specimens can be simulated, reducing the often undesired interactions between long range elastic fields and the simulation

boundaries. The second benefit is that more time steps can be conducted allowing for the simulation of longer time durations.

The successful application of a concurrent multiscale approach requires understanding the errors associated with the method. Of general concern are the errors resulting from the coupling methodology connecting the atomistic and continuum regions, and the errors resulting from the inadequacies of a continuum description of material response relative to a fully atomistic representation [71]. A particular challenge associated with multiscale modeling of metallic crack tips, is that dislocation defects are often driven into the atomistc-continuum interface. Several strategies exist for addressing this challenge. For example, in the Quasicontinuum method [91] remeshing is performed to ensure that dislocations never contact the atomistic-continuum interface. In the Embedded Statistical Coupling Method [87], the atomistic details of the connectivity at the atomistic-continuum interface are updated so that when a dislocation approaches the interface it is instantaneously moved far outside the specimen on its current slip plane. In the Coupled Atomistic Discrete Dislocation (CADD) Method [93, 84], when a dislocation reaches the atomistic-continuum interface, it is instantaneously moved to the other side of the interface and then explicitly modeled as a discrete dislocation in the continuum domain.

While concurrent multiscale modeling works to address the challenges associated with the limited temporal and spatial domains of atomistic modeling, the timescale of the simulations often remains disconnected from typical experiments. The disconnect in timescales can also be addressed in a brute force manner, by parallelizing the simulation dynamics in time. This approach, known as parallel replica dynamics [109], is effective when the evolution of the system is

controlled by a succession of rare events (or transitions), with the time between events being uncorrelated, i.e. a Poisson process. The parallel replica approach consists of performing simultaneous MD simulations on statistically identical systems (or replicas) and advancing all the systems when a rare event occurs on any one of the systems. At its best, the approach can provide a speedup that scales nearly proportional to the number of replicas used. However, in practice the approach is limited in that sufficient dynamics must be performed on each replica between transitions (rare events) to ensure that transition times remain uncorrelated, i.e. that the Poisson process assumption remains valid. The impact of this restriction can vary significantly dependent upon the application.

While the parallel replica approach accelerates MD time integration by parallelizing the sampling of phase space, most other accelerated timescale approaches operate by biasing the sampling of phase space. The simplest examples of such approaches consist of traditional MD performed at increased loads and/or temperatures relative to experiment. In many applications, increased loads and/or temperatures promote the system to more frequently visit regions of phase space that separate successive metastable states (often referred to as the activated state), thus promoting more frequent transitions (rare events) between metastable states. Due to its utter simplicity, this approach is one of the most common, especially in applications involving the deformation and failure of materials. While performing traditional MD simulations at high loads and/or temperatures certainly can accelerate transitions between metastable states, the results are often difficult to interpret with respect to typical laboratory timescales, temperatures, and loads, both qualitatively and quantitatively [112, 111].

In general, approaches that artificially bias dynamics to promote more frequent sampling of activated states can be categorized into two groups. The first involves approaches that try to mimic the evolution of a normal system but in an accelerated way. The popular hyperdynamics approach [108] fits this description. It consists of using an artificial potential to push the system away from metastable equilibrium states, and thus expedite transitions between states in a quantifiable way. A key challenge, associated with the practical implementation of the approach, is that the artificial biasing potential must be designed such that it goes to zero when the system nears activated states. This can present a considerable challenge considering that the activated states are often not known *a-priori*.

The other category of biased dynamics approaches involves two distinct steps. The first is to illuminate the possible transitions (or rare events) that the system may undergo. In this case, the goal is only to build a catalogue of potential transitions that may occur in the laboratory system. This can be achieved in a variety of ways using MD simulations performed at high loads, high temperatures [96], or with artificial biasing potentials [40, 60, 59]. The second step involves examining each potential transition to predict the rate at which the transition will occur under ordinary laboratory conditions. This task is often carried out using Transition State Theory and chain of states methods [77]. The resulting information can be used to provide a quantitative prediction of how the system will evolve at typical laboratory timescales.

In this work, we have combined several of the aforementioned approaches to study the atomic processes associated with crack growth. The study examines a crack tip in 2024-T3 aluminum alloy, making it particularly relevant to fatigue

prognosis in aerospace applications. By simultaneously employing CADD concurrent multiscale modeling, bond-boost hyperdyanmics, and parallel replica dynamics, the work strives to model crack tip response with atomic scale resolution at loading rates and sample sizes closer to those of typical experiments (Figure 3.1). The approach is validated against and builds off of previous long timescale studies of crack tip behavior [112, 111] that were limited to initial crack tip events. The results provide new insight into the crack growth mechanisms that operate in aluminum across the range of timescales that separate traditional MD and typical experiments. Furthermore the work seeks to provide new perspective on the prospect of using extended timescale techniques to model atomic scale fracture processes at typical experimental timescales. The manuscript is organized into a methods section that describes the techniques employed, followed by a validation section where a comparison is made to existing results in the literature, then an application section that discusses crack growth mechanisms and the performance of our approach.

3.3 Methods

3.3.1 CADD Concurrent Multiscale Method

The underlying theory of the multiscale method is built upon the Coupled Atomistic Discrete Dislocation (CADD) framework of Shilkrot et al. [93, 92], with the molecular static atomistic region of CADD being replaced by a MD atomistic region as detailed in [84]. The CADD coupling methodology consists of solving two distinct problems, involving a MD and continuum region that are

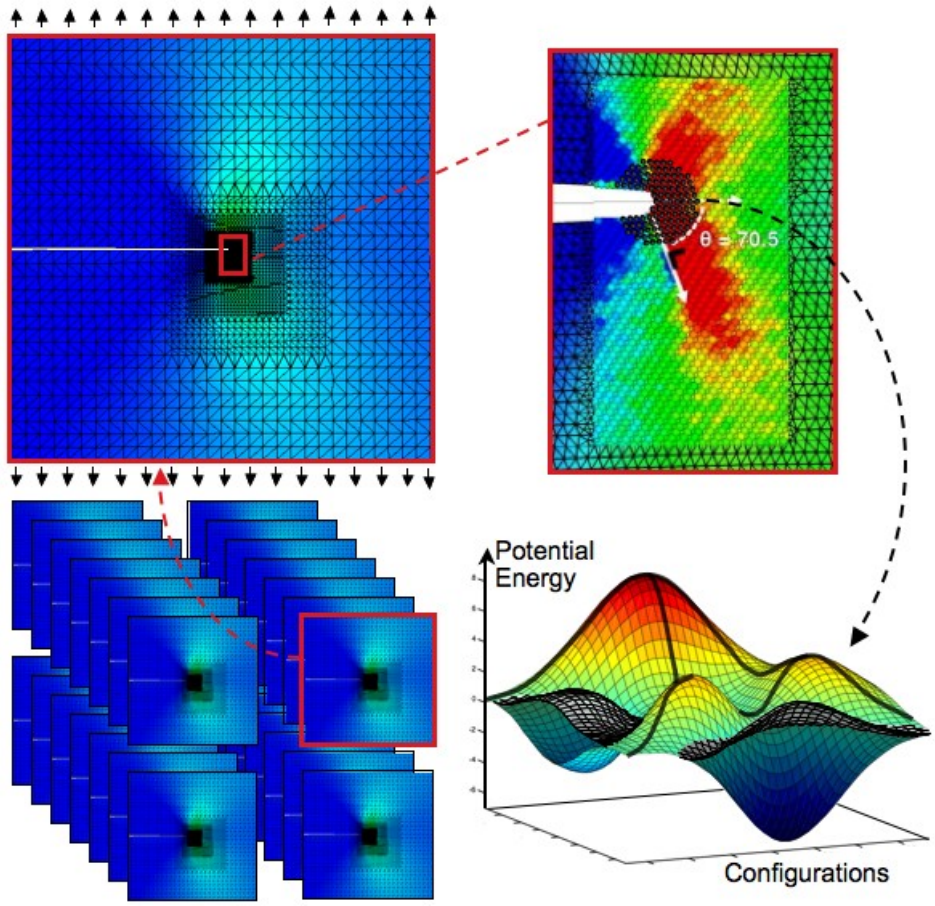

Figure 3.1: A cartoon of the combined time and spatial multiscale scheme. Multiple simulations of CADD are run in parallel using parallel replica dynamics (lower left), while hyperdynamics is used in each atomistic portion of CADD (lower right). A group of atoms around the crack tip in the upper right are colored black to indicate the general size and number of atoms used by bond-boost hyperdynamics. CADD itself replaces atomic degrees of freedom with finite elements to increase computational efficiency and increase the spatial domain of the system (top left).

coupled by self-consistent displacement boundary conditions. The MD region is composed of a set of atoms bounded by a set of interface atoms/nodes. The DD continuum region is approximated by finite elements and thus the fields associated with it are a function of the corresponding nodes. The interatomic force, **F**, experienced by each atom within the MD region results from interactions not only within the MD region and its bounding interface, but also interactions

with pad atoms that extend into the continuum. However unlike the atoms in the MD and interface regions, the positions of the pad atoms are controlled by the continuum solution. Thus the pad atoms provide the necessary nonlocal boundary conditions across the interface to the MD and interface regions. While the CADD methodology is not specific to any particular interatomic force model [76, 75], this work utilizes embedded atom empirical potentials to model interatomic forces [28, 2]. Both the interface atoms and those within the MD region are modeled with Langevin dynamics,

$$\ddot{\mathbf{x}} = \frac{\mathbf{F}}{m} - \gamma\dot{\mathbf{x}} + \chi\frac{\mathbf{F_A}}{m}, \tag{3.1}$$

where $\ddot{\mathbf{x}}$ is the acceleration of the particular atom, $\dot{\mathbf{x}}$ the velocity, $\mathbf{F}$ the force, m the mass, γ is a damping coefficient, χ a uniform random number between $-1 \leq \chi \leq 1$, and $\mathbf{F_A}$ the applied random force. The components of $\mathbf{F_A}$ are

$$F_{Ai} = \sqrt{\frac{6\gamma m k_B T_0}{\Delta t}}, \quad i = x, y, z, \tag{3.2}$$

which produces a canonical ensemble where k_B is Boltzmann's constant, T_0 the desired equilibrium temperature, and Δt the MD time step. The applied damping coefficient, γ, is a function of position,

$$\gamma = \gamma_0 \left[1 - \frac{d(x,y)}{w}\right], \tag{3.3}$$

where γ_0 is the maximum damping coefficient, w is the width of the damped 'stadium' region, and $d(x,y)$ is the minimum distance from the atom to the MD/DD interface,

$$d(x,y) = \text{abs}\left(\min\left(x - x_{min}, x - x_{max}, y - y_{min}, y - y_{max}, w\right)\right). \tag{3.4}$$

The damping coefficient field provides maximum damping (or thermostating) at the MD-DD interface, decreases linearly with distance away from the interface, and is zero at distances greater than w away from the interface. This approach provides a relatively constant equilibrium temperature across the MD

region while minimally affecting the natural dynamics of the system away for the MD-DD interface. A detailed analysis of the approach is given in [84].

The response of the continuum region is local, and therefore, it is only a function of the boundary conditions and the resulting deformation within that region. The continuum region is assumed to be in elastic equilibrium, such that the energy functional associated with the region is always minimized,

$$E^c = \frac{1}{2}\int_{\Omega_c} (\hat{\boldsymbol{\sigma}} + \tilde{\boldsymbol{\sigma}}) : (\hat{\boldsymbol{\epsilon}} + \tilde{\boldsymbol{\epsilon}})\, \mathrm{d}V - \int_{\partial\Omega_T} \mathbf{T_0}\, (\hat{\mathbf{u}} + \tilde{\mathbf{u}})\, \mathrm{d}A, \tag{3.5}$$

where Ω_c represents the continuum domain and $\partial\Omega_T$ represents the boundary of the continuum domain on which a traction boundary condition, $\mathbf{T_0}$, exists. $\tilde{\boldsymbol{\sigma}}$, $\tilde{\boldsymbol{\epsilon}}$, and $\tilde{\mathbf{u}}$, represent infinite medium stress, strain, and displacement fields, respectively, generated from the discrete dislocations at distinct locations. $\hat{\boldsymbol{\sigma}}$, $\hat{\boldsymbol{\epsilon}}$, and $\hat{\mathbf{u}}$ represent the solution fields from an anisotropic linear elastic boundary value problem that when superimposed with the dislocation fields satisfy the overall boundary conditions. $\hat{\boldsymbol{\sigma}}$, $\hat{\boldsymbol{\epsilon}}$, and $\hat{\mathbf{u}}$ are obtained using a standard displacement based finite element approach, while $\tilde{\boldsymbol{\sigma}}$, $\tilde{\boldsymbol{\epsilon}}$, and $\tilde{\mathbf{u}}$ are well known analytic fields [104]. The position of the dislocations within continuum domain evolve following

$$\mathbf{r}^i_{new} = \mathbf{r}^i_{old} + B\left(f^i \frac{\mathbf{b}^i}{|\mathbf{b}^i|}\right) \tag{3.6}$$

where $\mathbf{r}^i_{new}$ is the new position of dislocation i, $\mathbf{r}^i_{old}$ is the position of dislocation i from the previous update step, $\mathbf{b}^i$ is the Burgers vector of dislocation i, B is the mobility factor, and f^i is the Peach Koehler force of dislocation i given by

$$f^i = \left(\mathbf{n}^i\right)^T \left(\hat{\boldsymbol{\sigma}} + \sum_{j\neq i}^{N} \tilde{\boldsymbol{\sigma}}^j\right)\mathbf{b}^i \tag{3.7}$$

where $\mathbf{n}^i$ is the normal vector to the glide plane of dislocation i, $\hat{\boldsymbol{\sigma}}$ is the stress field calculated from the boundary value problem, and $\tilde{\boldsymbol{\sigma}}^i$ is the stress field generated by dislocation i. When a dislocation approaches the MD-DD interface,

dislocations are passed across it via the insertion of a dislocation dipole. The insertion of a symmetric dislocation dipole that spans the interface and lies on the plane of the dislocation to be passed effectively moves the dislocation to the other side of the interface. The details of this procedure are given in [92].

The CADD algorithm used here can be summarized as follows:

1. A brief period (approximately half of the Debye frequency of the material) of MD is performed on the MD and interface regions with the pad atoms remaining fixed to serve as boundary conditions. It is during this period that the simulation time is accumulated.
2. The averaged positions of the interface atoms over the previous period of dynamics are used to define the displacements of interface nodes which serve as Dirichlet boundary conditions for the continuum boundary value problem. The energy functional given in equation 4.5 is then minimized to obtain a solution using standard linear elastic finite element analysis.
3. The position of the discrete dislocations in the continuum region are updated following Equation 4.6.
4. The positions of the pad atoms are updated in accordance with the continuum solution.
5. Return to step 1.

The frequency of the interface updating was chosen to be on the order of half of the Debye frequency of the material to keep thermal pulses from entering the continuum domain [84].

The approach used here consists of several approximations that warrant further discussion. The first involves the mixing of static and dynamic models, i.e.

the atoms in the MD region are fully dynamic, the dislocation positions within the continuum region are dynamic but overdamped, and the elasticity field in the continuum region is placed in static equilibrium at evenly spaced time intervals of half the Debye frequency. This inconsistency, within the context of the application examined in this paper, does not significantly interfere with the natural evolution of the system, since it involves a succession of short fleeting events followed by long periods of equilibrium dynamics. Specifically, during the long periods of equilibrium dynamics the configuration of the DD region would be no different if dynamics were included, as in both cases the region will reside in its minimum energy state. A second significant approximation in the modeling is that the DD region can only accommodate in-plane displacement fields. This creates an inconsistency between the fully 3D MD and 2D DD regions. The effect of the inconsistency is that dislocations with a screw Burgers vector component emitted from the crack tip experience a repulsive image force from the MD-DD interface. For the specific geometry and loading considered in this work, dislocations with screw character play a secondary role and their behavior has been shown to not be significantly affected by the artificial image forces by examining parametric studies involving the size and shape of the MD region. However, the incorporation of out-of-plane displacements in the DD region is important in general, and as such we plan to implement this feature in the future.

3.3.2 Parallel Replica Dynamics

The parallel replica method [109] provides a brute force means for decreasing the disconnect in timescale between MD simulation and typical experiments.

The method requires that the system evolution can be effectively modeled as a Poisson process, in that it evolves in time by a succession of rare events (or transitions) with the time between events being uncorrelated. Accordingly, the probability that the next rare event occurs at a time, t, in the future is given as

$$p(t) = k_{tot} e^{(-k_{tot} t)}, \tag{3.8}$$

where k_{tot} represents the rate at which a particular rare event will occur. Considering that a loaded ductile crack tip, as examined in this work, evolves via a succession of rare events, and that the MD region of the finite temperature CADD model follows canonical NVT dynamics, the parallel replica approach is certainly valid for this problem.

The parallel replica approach consists of performing simultaneous MD simulations on statistically identical systems (or replicas) and advancing all the systems when a rare event occurs on any one of the systems. Therefore, within a parallel replica simulation, the total time t_{sum} since the last transition is given as

$$t_{sum} = S\, t_1, \tag{3.9}$$

where t_1 is amount of time spent simulating dynamics on replica number 1. Correspondingly, the total rate constant, k_{tot}^{super}, can be written as

$$k_{tot}^{super} = S\, k_{tot}^{(1)}, \tag{3.10}$$

where $k_{tot}^{(1)}$ is the rate constant of the rare event in replica number 1. The factor S is given as

$$S = \sum_{i}^{M} s_i, \tag{3.11}$$

with M being the total number of replicas, s_i a scaling factor representing how much more quickly replica i is running compared to replica number 1 (s_1 is

always equal to 1). In the case where all replicas are running at the same speed, then all s_i are equal to s_1, and S is equal to M.

The rate at which rare events occur across M replicas is the weighted sum of all of the rates on each individual replica. Thus, the probability of a single rare event occurring when using M parallel replicas, p_{super}, is:

$$\begin{aligned} p_{super}(t_1) &= k_{tot}^{super} e^{-k_{tot}^{super} t_1} \\ &= S\, k_{tot}^{(1)} e^{-S k_{tot}^{(1)} t_1} \\ &= S\, k_{tot}^{(1)} e^{-k_{tot}^{(1)} t_{sum}} \end{aligned} \tag{3.12}$$

Using $t_1 = \frac{t_{sum}}{S}$ and $p\left(\frac{t}{S}\right) dt = S\, p(t)\, dt$, equation 3.12 can be rewritten as

$$p_{super}(t_{sum}) = k_{tot}^{(1)} e^{\left(-k_{tot}^{(1)} t_{sum}\right)}. \tag{3.13}$$

This indicates that the probability of a rare event occurring on a system of 1 replica is the same as the probability of the same event occurring on a system of M replicas when the total time is taken as the sum of the simulation time on all replicas. This proof holds for replicas sampling at the same or different speeds ($s_i \neq 1$).

Employing the parallel replica dynamics approach is straight forward. First, M statistically independent replicas of the system of interest are created by copying a single system M times and then performing MD for a dephasing period where each replica uses a distinct value of χ. After dephasing, the simulations clocks are started, with the simulations continuing until a transition (or rare event) is detected on one of the replicas. At this point all other replicas are stopped, and the total time elapsed since the last transition event is provide by

equation 3.9. MD is continued on the replica that transitioned for an additional period of time to allow correlated transitions to occur. The transitioned configuration is then copied over all other replicas and the process is repeated. This approach provides a speedup directly proportional to the number of replicas used, minus the time spent dephasing and checking for correlated transitions. Thus, a system that exhibits frequent transitions will be significantly slower than one that does not. An additional cost of the method relative to traditional MD is involved with the computational cost of detecting transitions. A significant advantage of the parallel replica approach is that nothing prohibits it from being combined with other accelerated timescale techniques [107, 108], such as hyperdynamics, as done in this work.

3.3.3 Bond-Boost Hyperdynamics

While the use of CADD and parallel replica dynamics increase the total number of time steps that can be conducted with a given set of resources, the aim of hyperdynamics is to increase the effective time increment associated with each timestep. Hyperdynamics operates by biasing system dynamics so that activated states are explored more frequently. While a brief review of hyperdynamics is given here, we direct the reader to [108] for a more complete discussion.

The hyperdynamics method can be concisely explained by considering a system that transitions from a metastable state in a potential energy basin A to a metastable state in a potential energy basin B. The transition rate between A and B can then be written as

$$k_{A\to B}^{TST} = \langle |v_{A\to B}| \, \delta(r, s) \rangle, \tag{3.14}$$

where $\delta(r, s) = 1$ when the configuration of atoms, r, is on the dividing surface, s, between states A and B. Otherwise $\delta(r, s) = 0$. v_A is the velocity at which configurations crossing from A to B are moving normal to the dividing surface. $\langle \cdot \rangle$ is the ensemble average operator given by

$$\langle x \rangle = \frac{\int_A x e^{-\beta V(r)} dr}{\int_A e^{-\beta V(r)} dr}, \tag{3.15}$$

with $\beta = \frac{1}{k_B T}$, k_B being Boltzmann's constant, T the temperature, and $V(r)$ the potential energy of the system. Expressing the transition rate as equation 3.14 constitutes the basis of traditional transition state theory approaches [105] and is a powerful approach so long as the majority of trajectories leaving A crossing s equilibrate in B.

If a biasing force, given as a positive boost potential, $\Delta V(r)$, is added to the original potential energy landscape the transition state rate can be rewritten as

$$k^{TST}_{A \to B} = \frac{\langle |v_{A \to B}| \, \delta(r, s) \, e^{\beta \Delta V(r)} \rangle_b}{\langle e^{\beta \Delta V(r)} \rangle_b}, \tag{3.16}$$

where $\langle \cdot \rangle_b$ is defined by

$$\langle x \rangle_b = \frac{\int_A x e^{-\beta (V(r) + \Delta V(r))} dr}{\int_A e^{-\beta (V(r) + \Delta V(r))} dr}. \tag{3.17}$$

If the boost energy is defined such that it goes to zero at s, the transition rate (equation 3.16) can then be expressd as

$$k^{TST}_{A \to B} = \frac{\langle |v_{A \to B}| \, \delta(r, s) \rangle_b}{\langle e^{\beta \Delta V(r)} \rangle_b}, \tag{3.18}$$

which corresponds to the measured transition rate in the system with the boosted potential divided by a boost factor $\langle e^{\beta \Delta V(r)} \rangle_b$. Subsequently, the average transition time, $\tau = \frac{1}{k}$, in a system with a boosted potential can be related to the real transition time with the boost factor,

$$\tau^{TST}_{A \to B} = \tau^{TST}_{A_b \to B_b} \langle e^{\beta \Delta V(r)} \rangle_b. \tag{3.19}$$

It is important to point out that this approach preserves the relative rate of transitions to different states,

$$\frac{k^{TST}_{A_b \to B_b}}{k^{TST}_{A_b \to C_b}} = \frac{k^{TST}_{A \to B}}{k^{TST}_{A \to C}}, \tag{3.20}$$

and thus does not artificially influence the systems evolution, provided the ensemble averaging is accurate.

In this work we used the bond-boost potential [72] to bias the system dynamics. The bond-boost potential is based on the bond breaking picture of deformation. It assumes that bonds must stretch or compress beyond a certain threshold in order for a transition to occur. The potential takes the functional form

$$\Delta V(r) = A(\epsilon_1, \epsilon_2, ..., \epsilon_{N_b}) \sum_{i=1}^{N_b} \delta V(\epsilon_i), \tag{3.21}$$

where N_b is the number of bonds tagged to receive the boost potential. Both functions $A(\epsilon)$ and $\delta V(\epsilon)$ depend on the bond strain relative to the bonds equilibrium distance. The strain of bond j, $\epsilon(r_j)$, is defined as

$$\epsilon(r_j) = \frac{r_j - r_j^{eq}}{r_j^{eq}}, \tag{3.22}$$

where r_j is the configuration of the atoms that make up bond j, and r_j^{eq} is the equilibrium configuration of those atoms. The functional form of $\delta V(\epsilon)$ is given as

$$\delta V(\epsilon) = \begin{cases} \frac{\Delta V^{max}}{N_b}\left[1 - \left(\frac{\epsilon}{q}\right)^2\right] & -q \le \epsilon \le q \\ 0 & \text{otherwise,} \end{cases} \tag{3.23}$$

where ΔV^{max} is a free parameter that controls the amount of boost energy applied to the system. This function goes to zero when the bond strain goes to $\pm q$ and is maximum at zero bond strain. The blanket function, $A(\epsilon)$, which is a function of the maximum bond strain, ϵ^{max}, drives the boost potential to zero

when the strain of any bond reaches a value of $\pm q$. Thus, bond-boost hyperdynamics is based on the assumption that at least one bond must strain beyond a value of q for the system to reach the dividing surface, s. This is required so that the bond-boost potential is consistent with the formulation of hyperdynamics, which requires the boost potential to be zero at s. The blanket function used in this study is

$$A(\epsilon^{max}) = \begin{cases} \dfrac{\left[1 - \left(\dfrac{\epsilon^{max}}{q}\right)^2\right]^2}{1 - P_1^2\left(\dfrac{\epsilon^{max}}{q}\right)^2} & -q \leq \epsilon \leq q \\ 0 & \text{otherwise,} \end{cases} \tag{3.24}$$

with both A and its first derivative going to zero at $\epsilon^{max} = \pm q$.

For the hyperdynamics method to be effective, the system must come to equilibrium between each transition to enable the ensemble average in Equation 3.19 to be computed to sufficient accuracy. Furthermore, the accurate computation of the ensamble averages requires that the bond-boost parameters are chosen such that the system does not get stuck in local energy minima created by the boost potential, and that the maximally stretched bond varies. The accuracy of the hyperdynamics method also depends on the boost potential going to zero at s.

The free parameters of the bond-boost potential are N_b, ΔV^{max}, q, and P_1. For maximum effectiveness, N_b should only include the bonds that participate in the transition. As more bonds are included, the volume of phase space to be sampled increases, thus decreasing speedup provided by the method. Alternatively, if N_b does not include all of the bonds that are active in the transition event, the bond-boost potential will not push the relevant degrees of freedom towards s, thus making the method less efficient. In this work we used approximately

6,000 bonds, connecting approximately 700 atoms, in a 15 $\AA$ radius surrounding the crack tip. The area of boosted material encompasses several atomic planes around the crack tip, including atoms along the crack faces and crack tip (Figure 3.1). A future version of the method which boosts only those the bonds near free surfaces and areas with a severely distorted lattice structure may be worth attempting.

As described previously, the parameter q acts as a cutoff strain for the bond-boost potential so that the potential is zero at s. If q is chosen too large, the hyperdynamics approach breaks down, as the measured transition rate on the boosted potential system becomes $\langle |\nu_{A\to B}|\, \delta(r,s)\, e^{\beta\Delta V(r)} \rangle_b$, a quantity which in practice is difficult to relate to the transition rate of the unboosted system. Accordingly the choice of q is constrained in that it must be small enough to ensure that $e^{\beta\Delta V(r)}$ is zero at s, while being maximized so that the boost potential spans a large region of configuration space, maximizing the boost factor and subsequent benefit of the hyperdynamics.

Perhaps the most robust and accurate approach for choosing q would be to perform parametric studies, that show a converged transition rate with a decreasing value of q. However, considering that hyperdynamics is often applied to long computationally expensive simulations, parametric studies on the value of q are often unfeasible. An alternative approach would be to examine individual transitions with chain of states methods [48, 106] *a posteriori* to verify that the chosen value of q is not too large. If q is found to be too large, the hyperdynamics simulation must be restarted from a state prior to the transition with a smaller value of q. Another alternative is to select the value of q based on the bond strains of the saddle states of a set of potential mechanisms that may occur.

For instance, the maximum bond strain observed at the saddle state for surface diffusion in copper is 0.35 [72], and the maximum bond strain associated with the saddle state for stacking fault creation by rigid shearing in an fcc crystal is 0.26. It is worth noting that limiting the choice of q to be below 0.26 would be very conservative for studying dislocation nucleation events where the saddle state often consists of a dislocation loop. In the case of partial dislocation nucleation, the center of the dislocation loop consists of a stacking fault region where bonds are strained to 0.53. In this work, a maximum bond strain of $q = 0.35$ was found to give accurate results for leading, trailing, and twinning partial dislocations nucleating from a free surface (as will be shown in the next section), while providing a significant boost factor.

The parameter P_1 controls how quickly the first derivative of the blanket function goes to zero as the maximum bond strain increases. Studying surface diffusion, Miron and Fichthorn (2003) [72] used $0.9 \leq P_1 \leq 0.98$, which corresponded to an abrupt change to zero. A value of $P_1 = 0.2$ was used in this work. For the system studied here we found that smaller values of P_1 helped increase the rate at which the maximally stretched bond switches, decreasing the time required to get accurate time averages, subsequently raising the overall boost factor.

The choice of P_1 can also act to reduce the errors if q is chosen too large. For example, using typical values for the bond-boost parameters collected from several simulations (number of bonds, equilibrium bond lengths, $\Delta V^{max} = 0.25$, etc.) with $q = 0.35$ and $P_1 = 0.2$, at a bond strain of $\epsilon = 0.3$, $\Delta V = 0.018$, giving an instantaneous boost factor 2.0. When $\epsilon = 0.25$, $\Delta V = 0.06$, giving an instantaneous boost factor of 9.9. This equates to the recorded transition time

being off by a factor of 2.0 if the transition state was at $\epsilon = 0.3$ and off by a factor of 9.9 if the transition state was at $\epsilon = 0.25$. If the transition state was at $\epsilon = 0.3$ or 0.25, the transition time would be by off by a factor of 5.1 or 45.8, respectively, if P_1 were set to 0.9.

The free parameter, ΔV^{max}, is adjusted adaptively as the simulation proceeds. A similar adaptive approach was previously shown to be effective by Perez and Voter (2008) [82] who studied surface diffusion of silver. Since the accuracy of the boost factor is critical for correctly converting the transition time to the unboosted system, the ensemble average in equation 3.19 must be carefully computed [72, 82, 90]. This requires that the simulation trajectory sufficiently visits the high probability regions of phase space. The sampling of phase space was characterized by recording the number of times the maximally stretched bond switches, following [82]. If the bond switches infrequently, dV^{max} was lowered, while if the switching occurred frequently, dV^{max} was increased to raise the boost factor. Over time, the system examined here converged to a value of ΔV^{max} that maintains the frequency of bond switching prescribed. Specifically, for the simulations in this paper, the average number of time steps between maximally stretched bond switches was between 70 and 200. This corresponds to switching frequencies similar to the Debye frequency of the material on the unboosted potential, $\sim$ 100fs, and enable the computation of converged ensemble averages within a few picoseconds.

3.4 Validation of Bond-Boost Hyperdynamics

As a validation of the combined parallel replica and bond-boost approach and parameters used here, we examined the expectation time for dislocation nucleation from a crack tip as was done in [111]. The specimen consisted of an fcc crystal with an edge crack. The crack plane normal direction was [1 1 1] and the crack tip was parallel to the [$\bar{1}$ 1 0] direction. This configuration has a slip plane intersecting the crack plane along the crack front at an angle of 70.5°. The crack tip was created by removing 3 consecutive (1 1 1) planes of atoms.

Using CADD, the crack tip at the center of the specimen was embedded into a 3D atomistic region of $84 \times 147 \times 20$ $\mathring{A}$, which was encompassed by a larger 2D plane strain, DD continuum region spanning $0.2 \times 0.2 \times 0.002$ microns. The elastic constants of the continuum material were $C_{11} = 0.736$, $C_{12} = 0.389$, $C_{44} = 0.229$ eV/Å^3. The temperature of the MD region was controlled via the ramped Langevin thermostat described previously, with T=300K degrees. The lattice constants at 300K were 4.051Å for aluminum and 3.535Å for Nickel. Loads were applied by prescribed displacements at the outer boundary of the DD region corresponding to the continuum solution for a crack in an anisotropic linear elastic material subjected to mode I loading.

The specimen first deviates from an elastic response upon loading by nucleating a leading Shockley partial dislocation of pure edge character from the crack tip. This response occurred for both Al and Ni embedded atom potentials [28, 2], with Ni requiring higher loads for nucleation to occur. The simulation time at which the nucleation event occurred for various loads is plotted in Figure 3.2a alongside of the data from [111]. The degree to which nucle-

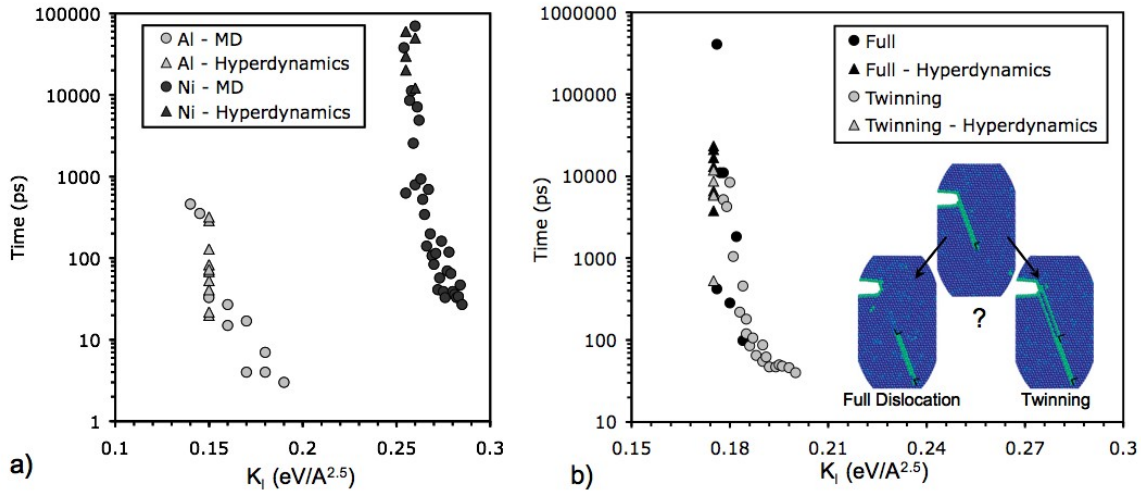

Figure 3.2: Comparison of data from direct MD or parallel replica dynamics to simulations using bond-boost hyperdynamics or combined bond-boost and parallel replica dynamics. The triangular data points are from the current work, and the circular data points are from [111]. Part a) shows the time to nucleate a stacking fault from a crack tip at a fixed stress intensity. The data compares direct MD to bond-boost hyperdynamics for both nickel and aluminum systems. Part b) shows the time to nucleate either a full or twinning partial dislocation (illustrated in the inset) after a stacking fault at a fixed stress intensity. The triangular data from the current work was found with the combined bond-boost and parallel replica scheme while the circular data from [111] uses only parallel replica dynamics.

ation of the leading partial dislocation is thermally activated in aluminum is limited, as a stable equilibrium configuration for the partial dislocation only exists at loads slightly below the critical load where nucleation occurs instantaneously. Nonetheless, the bond-boost hyperdyanmics approach still proves beneficial, providing boost factors between 1 and 10, and results that closely match those of [111] where hyperdynamics was not used. In Ni, where thermal activation can play a much more significant role in dislocation nucleation, the bond-boost hyperdynamics approach is much more beneficial providing a boost factor (speedup) of 300 to 1,900 while still accurately predicting the nucleation time [111].

At higher fixed loads, the thermally activated nucleation of the second partial dislocation can be examined. We define its nucleation time as the time from when the first dislocation nucleates and reaches its equilibrium position. The second nucleation event was examined for the aluminum potential at 300K. For this event, hyperdynamics provides a boost factor of 4 to 77. For the second nucleation event, a range of q values were investigated. The cited boost factor and the results shown in Figure 3.2b correspond to q values between 0.25 and 0.4. q values of greater than 0.45 were also examined (not shown), but as expected the simulations produced erroneous results. The slip plane and character of second partial dislocation nucleation event constitutes a competition between twinning and full dislocation emission. Hyperdynamics did not appear to artificially influence the outcome of the competition.

In total, the above results motivated the choice of $q = 0.35$ for the subsequent simulations presented in this paper. This value provides a significant boost factor, yet does not appear to artificially influence crack tip processes, and is consistent with the strains associated with the critical states involving diffusion and stacking fault creation as discussed earlier.

3.5 Application: Crack Opening at Constant K_I Rate and Temperature

As an initial application of the combined CADD, parallel replica, and bond-boost hyperdynamics framework we examined the response of an aluminum crack tip subjected to a continuously increasing load. The simulations consisted of an atomic region $150 \times 200 \times 20$ angstroms embedded within a DD contin-

uum region extending to 0.2 mm $\times$ 0.2 mm $\times$ 0.002 microns. The orientation and material parameters (elastic constants, lattice parameter, etc.) of the crystal were the same as that used in the validation studies in the previous section. The frictional resistance to dislocation glide in the DD region was chosen to simulate the resistance to dislocation glide in aluminum 2024-T3, i.e. the bulk shear strength (283 MPa [22]) divided by the Taylor factor [101], 3.0. The configuration of atoms near the crack tip differed slightly from those used in the previous section in that a single row of atoms at the crack tip was removed. In initial studies conducted without accelerated MD at zero temperature, the removal of the row of atoms had no effect on the initial nucleation events. Only a slight variation in the number of dislocations was observed, and the transition from dislocation emission to brittle crack growth occurred at the same stress intensity. The advantage provided by removing the row of atoms is mostly justified by the reduced number of atomic bonds needed to be used by the Bond-Boost scheme, thus increasing computational efficiency and lowering the sampling time of the Bond-Boost method. Due to the large computational expense of the extended timescale simulations, only the altered crack tip configuration is studied here. The effect of the new configuration is expected to be small, especially if the first few events are minimally affected.

The use of the parallel replica and hyperdynamics methods requires some care for the ramped loading situation. While both methods can be used in simulations involving slow continuously ramped loading, the two methods will not work for ramped loading when combined [103, 55]. Thus, in this work we approximate continuous loading by a succession of time increments having increased fixed loads. Each time increment consists of multiple replicas with hyperdynamics being performed for a given increment of time at a fixed load.

When the given increment in time is reached, the load is increased by a small amount then the hyperdynamics is restarted at the new load. When a transition occurs, the simulation continues without hyperdynamics on the replica on in which it occurred for a given correlation time, then parallel replicas with hyperdynamics are created. This simple approach requires that the load increment is not too large, and that the time increment is long enough to achieve a sufficient sampling of the boosted phase space. Transitions are detected when the maximum bond strain remains above $|q|$ for 1000 MD steps.

3.6 Results

Simulations were started at intial loads between $K_I = 0.12$ eV/Å$^{2.5}$ and $K_I = 0.14$ eV/Å$^{2.5}$, and were loaded with subsequent load steps of 0.01 eV/Å$^{2.5}$ to a load of at least 0.3 eV/Å$^{2.5}$. The rate of loading was varied by waiting 10ps, 100ps, 1ns, or 10ns between load increments. This equates to effective loading rates of 1×10^9, 1×10^8, 1×10^7, or 1×10^6 eV/Å$^{2.5}$/sec (1 eV/Å$^{2.5}$/sec $\approx$ 1.6 MPa $\sqrt{m}$/sec). The fastest rates are typical of traditional MD simulations spanning subnanosecond time domains. All simulations, except the one performed at the slowest rate were loaded to a maximum stress intensity of 0.3 eV/Å$^{2.5}$, with the slowest rate simulation only loaded to 0.24 eV/Å$^{2.5}$ due to limitations in computational resources. As a reference, simulations used approximately 3, 25, 450, and 8000 CPU hours per load increment for rates of 1×10^9, 1×10^8, 1×10^7, and 1×10^6 eV/Å$^{2.5}$/sec respectively. For the slowest rate, approximately 72000 CPU hours were used on an average simulation, while at the fastest rate approximately 100 CPU hours were used on an average simulation. The simulations were performed using quad core 2.7GHz Intel Xeon Processors.

3.6.1 Performance of Methods

We have attempted to quantify the performance of the parallel replica and bond-boost hyperdynamics techniques with respect to the ramped loading crack tip problem examined here. For this purpose, we have analyzed several relevant quantities across 16 simulations, involving various numbers of parallel replicas, loading rates, and crack tip behaviors (as will be discussed in the following section). Specifically in Table 3.1 we report the

1. Average boost factor: The time averaged boost recorded by all parallel replicas for a particular simulation (noting that the boost factor is only applicable during the periods that hyperdynamics is turned on.)
2. Intertransition speedup factor (ISF): The average boost factor multipled by the number of replicas, i.e. the average speedup of the simulation when both parallel replica and hyperdynamics are active.
3. Overall speedup factor (OSF): The total speedup relative to an unboosted simulation on a single processor.
4. Effectiveness (E): The overall speedup factor divided by the intertransition speedup factor, representing the fraction of wall clock time that bond-boost is active (noting that it is a good approximation to assume that parallel replica dynamics is only active during this time as well).

Table 3.1: Data collected from several accelerated dynamics simulations performed across three orders of magnitude in loading rates. The recorded boost factor is the average value of the boost factor recorded on all replicas throughout the simulation. The intertransition speedup factor is the number of parallel replicas multiplied by the average boost factor. The overall speedup is the simulation time recorded divided by the number of steps on a single parallel replica multiplied by the MD time step of one femtosecond. The effectiveness is the overall speedup divided by the intertransition speedup factor. Rows highlighted in grey used the selective bonding scheme mentioned in the Treating Rapid Transitions section.

K_I Rate (eV/Å$^{2.5}$/sec)	Parallel Replicas	Boost Factor	Intertransition Speedup Factor	Overall Speedup	Effectiveness
1×10^{8}[a]	1	4.6	4.6	1.7	0.37
	1	2.7	2.7	1.4	0.52
	2	6.9	13.8	4.6	0.33
1×10^{7}	5	13.6	68.0	16.0	0.24
	10	7.9	78.5	19.3	0.25
	10	8.8	88.0	14 .0	0.16
	21	15.5	325.5	47.3	0.15
	51	7.7	392.7	43.3	0.11
	100	2.0	200	48.9	0.24
1×10^{6}	1[b]	4.43	4.43	4.2	0.96
	1[c]	13.3	13.3	11.2	0.84
	1[d]	5.7	5.7	5.3	0.93
	1[e]	3.8	3.8	3.4	0.89
	100	31.7	3170	367.8	0.12
	100	13.9	1390	153.9	0.11
	100	12.5	1250	130.1	0.10
	150	21.3	3195	410.0	0.13
	200[f]	8.3	1650	153.2	0.09

[a]Only three of six simulations at this loading rate used the combined parallel replica and hyperdynamics scheme.
[b]This simulation used $P_1 = 0.9$, and was only used to calculate the boost factor in the initial state. This simulation was used to find the average boost factor for all simulations (it uses the same parameters as those used to simulate multiple events), and can be used as a comparison of relative boost factors between simulations with different parameters.
[c]This simulation used $P_1 = 0.2$, and was only used to calculate the boost factor in the initial state. This simulation was not used to find the average boost factor for all simulations, but can be used as a comparison of relative boost factors between simulations with different parameters.
[d]This simulation used $q = 0.3$, and was only used to calculate the boost factor in the initial state. This simulation was not used to find the average boost factor, but can be used as a comparison of relative boost factors between simulations with different parameters.
[e]This simulation used $q = 0.25$, and was only used to calculate the boost factor in the initial state. This simulation was not used to find the average boost factor, but can be used as a comparison of relative boost factors between simulations with different parameters.
[f]This simulation was not included in the Mechanisms section because it was not loaded to a high enough load to be comparable to the other simulations. It is included in the average boost factor calculation and experienced enough transitions to have an effectiveness that follows the trend from the other simulations.

Consistent with the wide variety of crack tip mechanisms that were observed over the set of simulations that were performed, the boost factor varied significantly. The average boost factor across all the simulations was 11.4 with a standard deviation of 7.6. This average value is relatively low with respect to applications of bond boost to surface diffusion [32, 72, 82]. However, the average value measured here is consistent with the work of Hara and Li (2010) [40] who investigated dislocation nucleation in copper at 300K using bond-boost hyperdynamics.

Despite the difference in deformation mechanisms among the simulations, the effectiveness of the method followed a clear trend. Simulations with a large intertransition speedup factor spent a larger percentage of wall clock time performing an unboosted simulation on a single processor. This is a direct result of simulations with greater intertransition speedup requiring fewer steps to find transitions, yet requiring the same amount of steps after each transition on a single replica. As seen in Figure 3.3, the effectiveness of method can be estimated as a power law function of the intertransition speedup factor:

$$E = 0.56\,(ISF)^{-0.22}\,. \tag{3.25}$$

Since the boost factor is relatively constant between simulations loaded at different rates, the overall speedup factor can be predicted from Equation 3.25 as

$$OSF = ISF \times E \tag{3.26}$$

where

$$ISF = \bar{\beta} \times N_{PR}, \tag{3.27}$$

with $\bar{\beta}$ being the average boost factor across all simulations, and N_{PR} the number of parallel replicas used. Figure 3.4 shows the non-linear scaling of the over-

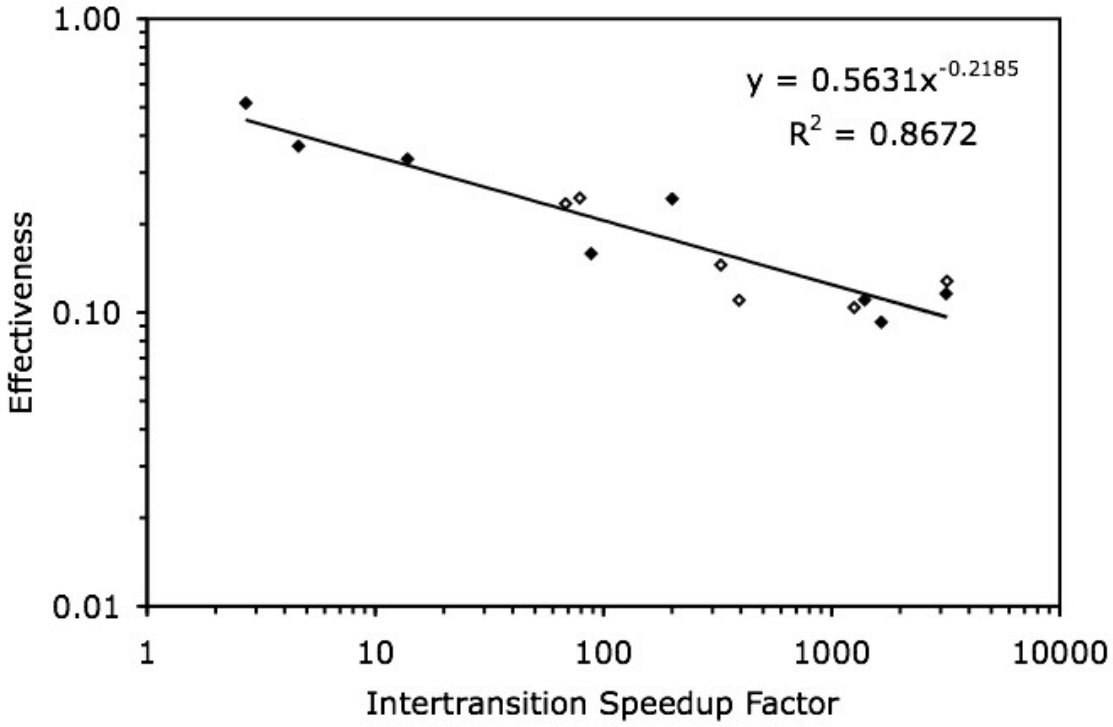

Figure 3.3: The power law relationship of the effectiveness of the combined time acceleration scheme as a function of the intertransition speedup factor. Simulations that used the selective bonding scheme use hollow symbols, while those that did not use solid symbols. Since the intertransition speedup factor can be estimated beforehand (using an average value of the boost factor), the effectiveness of a simulation can be predicted before running it.

all speedup factor with the number of parallel replicas, and illustrates that the overall speedup decreases relative to the intertransition speedup factor. Ultimately, this trend highlights the challenge of scaling extending MD simulations to standard experimental timescales using the parallel replica and bond-boost approaches.

In accordance with the above discussion, the expected wall clock time to complete a simulation at any given loading rate can be predicted. Here, we make predictions assuming a constant average boost factor of 11.4 and consid-

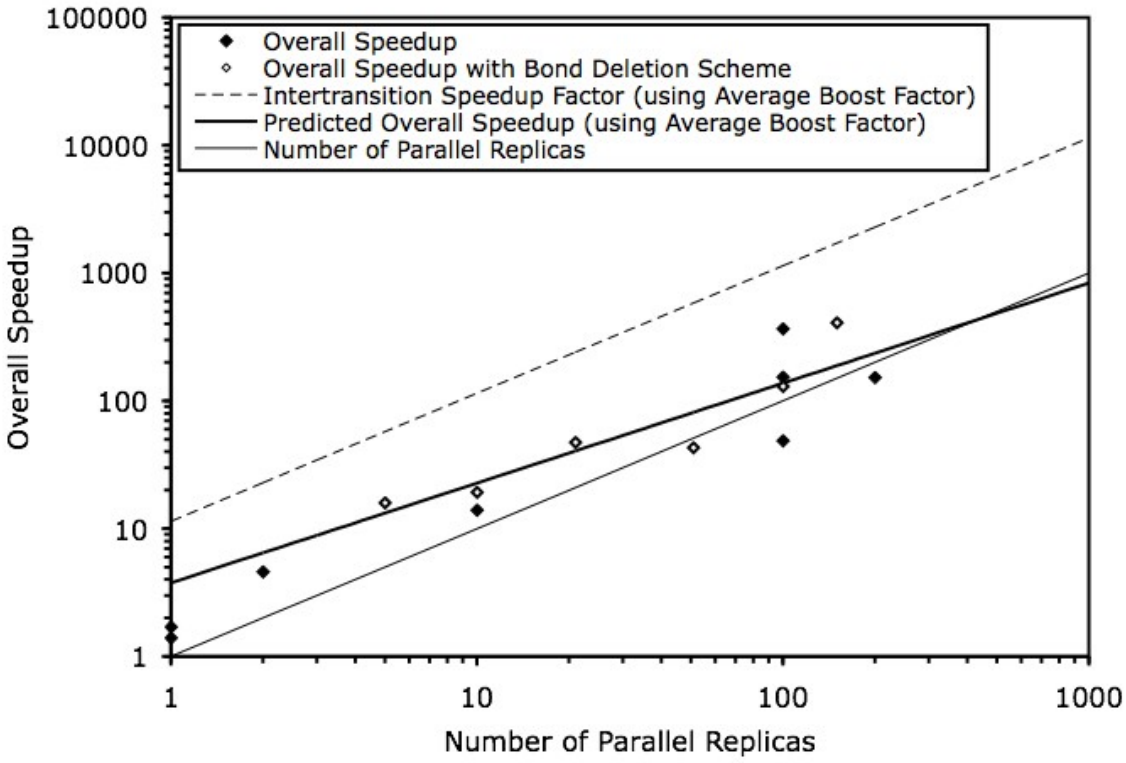

Figure 3.4: The overall speedup as a function of the number of parallel replicas. The thick solid line is the predicted scaling using the average boost factor of 11.4, while the thin solid lines are the scaling with the intertransition speedup factor and the number of parallel replicas. Simulations that used the selective bonding scheme use hollow symbols, while those that did not use solid symbols.

ering the requirement that a minimum number of time steps must be conducted between loading increments so that the approach remains accurate. This limits the number of parallel replicas that can be employed. Here we choose the minimum number of time steps to be 2000. With the boost factor remaining fixed, the maximum number of parallel replicas that can be applied increases as the loading rate is lowered. Figure 3.5 plots the wall-clock time (normalized by the wall-clock time of a simulation with no acceleration loaded at a rate of 1×10^9 eV/Å$^{2.5}$/sec) needed for a simulation at a given loading rate. The scaling is vastly improved from simulations without accelerated molecular dynamics,

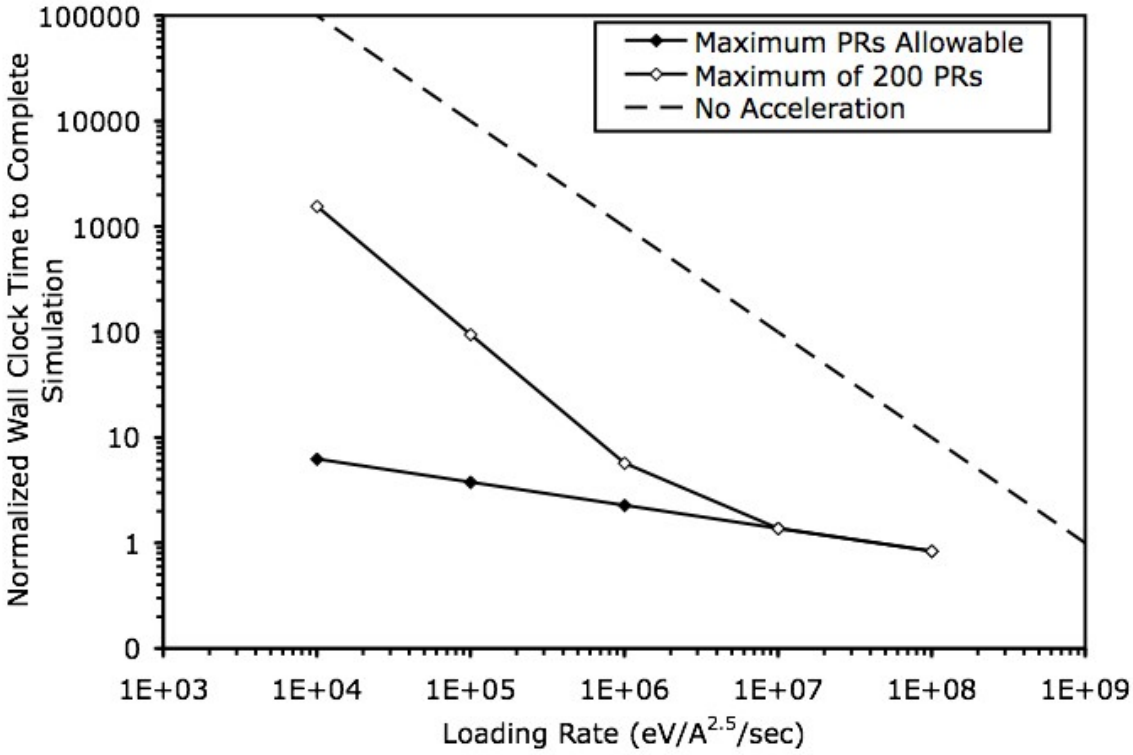

Figure 3.5: The wall-clock time needed to complete a simulation changes with the loading rate. The wall-clock time is normalized by a simulation performed at 1×10^9 eV/Å$^{2.5}$/sec with neither parallel replica dynamics or hyperdynamics (i.e. how much faster than a traditional CADD simulation with no time acceleration). As a comparison, the dashed line shows the scaling if no time acceleration is used, and hollow symbols indicate the scaling when a maximum of 200 parallel replicas are used (as in this study).

however, increasingly large numbers of parallel replicas are needed for slower loading rates (we calculate that 500, 5000, 50000 parallel replicas are need for simulations of 1×10^6, 1×10^5, 1×10^4 eV/Å$^{2.5}$/sec respectively). Our current investigation was limited to a maximum of 200 parallel replicas, which reduces the possible benefit of the method, and causes the wall-clock time to increase dramatically for slow loading rates. Unfortunately, even with the maximum allowable number of parallel replicas, the time needed to complete a simulation at 1×10^4 eV/Å$^{2.5}$/sec is estimated to be approximately 10 times longer than a

simulation performed at a typical MD rate of 1×10^9 eV/Å$^{2.5}$/sec. Even slowdowns of 2-3 times become prohibitive if simulations at 1×10^9 eV/Å$^{2.5}$/sec take several weeks to run on a single processor (as they did in this study).

3.6.2 Treating Rapid Transitions

The creation of an amorphous region near the crack tip from interstitial atoms, and the formation of a sessile Lomer dislocation which transitioned back and forth between core structures frequently triggered the transition detection scheme. Considering that the effectiveness of the combined parallel replica hyperdynamics approach is directly related to the number of transitions, the frequent transitions significantly slowed the rate at which the simulations advanced in time. Furthermore, the sufficientness of the choice of the bond boost parameter q was not tested for these transitions. To address this challenge, some simulations were performed where amorphous bonds were excluded from the hyperdynamics boosting and were not allowed to trigger the transition detection scheme. In other words, only the deformation of the crystalline bonds was tracked, even though they are still influenced by being adjacent to an amorphous zone or interstitial atom. This approach is akin to the super-state parallel replica procedure described in Perez et al. 2009 [81] where a solid material is in contact with a rapidly changing liquid.

The method for choosing which bonds were boosted proceeded as follows. After a transition was detected and subsequent 15 picoseconds of correlation time elapsed, all atoms in the boosted region were checked to see if they sat on crystallographic sites. To do this, all atoms were projected onto the x-y plane,

and all of their neighbors were counted within a small cutoff distance (1.75 Å). If the number of neighbors did not equal the number of planes of atoms along the thickness of the sample, those atoms were removed from the boost zone list. This process removed atoms that formed a 3D structure within the thickness of the sample, or atoms that strayed from their lattice spot into adjacent spots. This left only atoms that rest on a lattice site, with all of the other atoms on the same site through the thickness of the sample, as viable atoms to be have the boost potential added.

A total of eight simulations were conducted with the selective bonding scheme, however two simulations did not exhibit many transitions so they were ignored in the subsequent analysis. The effectiveness and scaling of the simulations with the selective bonding scheme did not change noticeably from the original simulations as seen in Figures 3.3 and 3.4. The lack of improvement can be attributed to the rapid evolution of the disordered zone. Since the disordered zone changed its size and affected atoms at the same time scale as the rapid transitions within the disordered zone, the scheme did not significantly limit the total number of transitions. Clearly, for the methodology used here to be improved, a more effective approach is needed to eliminate or reduce the rapid changes in the bonding of the system.

3.6.3 Crack Growth Mechanisms

The deformation mechanisms observed at the crack tip were dependent on the loading rate. At high rates an amorphous zone developed, and in the majority of simulations brittle crack propagation ensued. At lower rates, no amorphous

zone formed and full dislocations were nucleated. Several mechanisms were observed at all loading rates, such as the formation of twins and Lomer dislocations. The occurrence of these mechanism is dependent upon the geometry of the specimen [39] with some orientations being more favorable than others.

Zero Temperature Simulations

As a reference, a zero temperature simulation was performed using the same simulation setup as described in the Application Section with elastic constants and lattice constant matching the zero temperature interatomic potential. Zero temperature was maintained by scaling velocities by 0.999 each time step, which continuously drove the temperature to zero during the simulation. Each increment of stress intensity was allowed 2000 steps to reach equilibrium before the load was increased. At zero temperature, the first event was the nucleation of a leading partial dislocation with a Burgers vector of $\frac{a}{6}[\bar{1}\bar{1}\bar{2}]$, on the $\left(\bar{1}\bar{1}1\right)$ plane at a stress intensity of 0.35 eV/Å$^{2.5}$. A twinning partial dislocation, with the same Burgers vector, was nucleated at a stress intensity of 0.42 eV/Å$^{2.5}$, which sharpened the crack by breaking the bonds between the upper and lower crack faces. A total of eight twinning partial dislocations were nucleated up to a stress intensity of 0.60 eV/Å$^{2.5}$, each one breaking bonds between the crack faces, sharpening and extending the crack tip (Figure 3.6). At a stress intensity of 0.63 eV/Å$^{2.5}$ the crack begins to open without the nucleation of dislocations, extending the crack tip by less than two nanometers. Observing crack growth at stress intensities near 0.63 eV/Å$^{2.5}$ agrees with the results of a similar study by Farkas et al. 2001 [31], who studied the stress intensity required for crack growth in single crystal Al with the same orientation, but with a different interatomic potential

and dislocation pinning at the simulation cell boundaries. After the crack has grown, two more twinning partial dislocations are nucleated, but they only act to open the crack faces since the tip is at least a full nanometer ahead of the nano-twin. At a stress intensity of 0.72 eV/Å$^{2.5}$ the crack has extended approximately 55Å past the nano-twin, and new stacking faults are formed between the crack tip and the original nano-twin (Figure 3.6). The crack reaches the MD/DD interface at a stress intensity of 0.76 eV/Å$^{2.5}$. The sequence of mechanisms observed in this simulation are consistent with Farkas et al. 2001 [31]. The main difference is the delayed onset of the initial dislocation nucleation since the crack in this study is blunt, rather than perfectly sharp as in Farkas et al. 2001 [31].

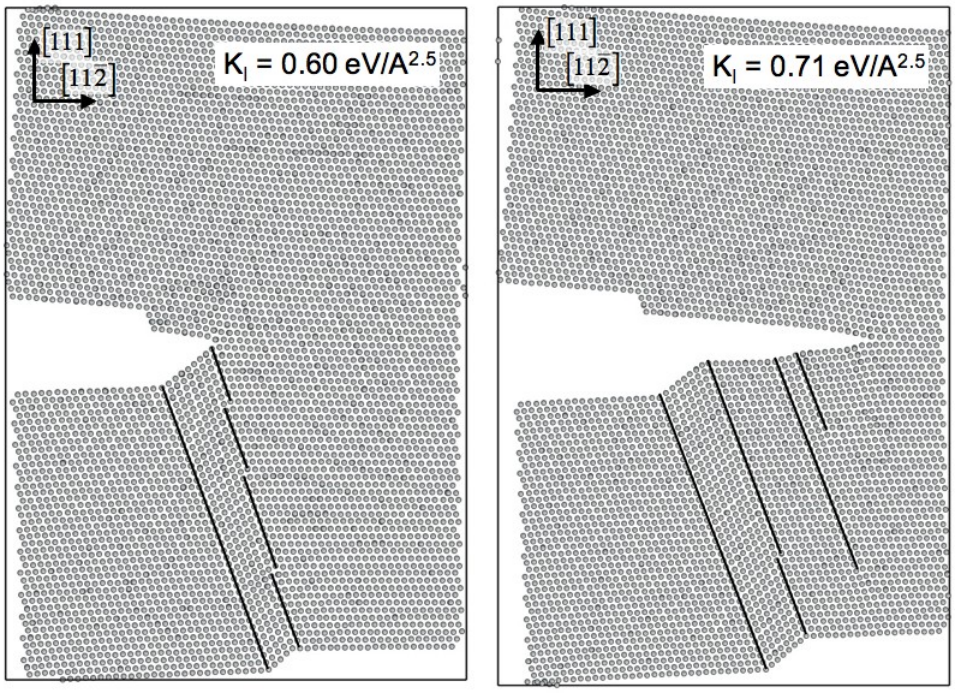

Figure 3.6: Two images from the atomic configuration near the crack tip from the zero temperature simulation. With increasing load, a stacking fault and then several twinning partial dislocations are nucleated at the crack tip, creating a nano-twin. Initially, the crack extends and sharpens by nucleating partial dislocations which break bonds between the upper and lower crack faces, as seen at a load of 0.60 eV/Å$^{2.5}$ in the image on the left. As the load increases to 0.69 eV/Å$^{2.5}$, the crack grows in a purely brittle manner by approximately 20Å along the (111) plane. At a load of 0.71 eV/Å$^{2.5}$ (right) the crack has extended approximately 30Å beyond its original configuration alternating between nano-twinning and brittle crack growth. Lines are drawn on the images to draw attention to twin boundaries and stacking faults. All atomic configurations plotted in this study are displayed using AtomEye [64].

Rate of 1×10^9 eV/Å$^{2.5}$/sec

Eleven simulations were performed at this rate using the original finite-temperature MD capabilities of CADD (no parallel replicas or hyperdynamics). In all cases, the first event consisted of the nucleation of a Lomer dislocation at stress intensities near 0.18 eV/Å$^{2.5}$. The dislocation had a Burgers vector of $\frac{a}{2}[110]$, where a is the lattice constant, and resided on the (001) plane one or two atomic spacings from the crack tip. The Lomer dislocation is sessile in that it cannot easily glide, but does propagate $12-13$Å away from the crack tip in some simulations. In five of eleven cases, the nucleation of the Lomer dislocation involved the movement of at least one surface atom to a subsurface interstitial site near the crack tip, most often in the dislocation core. The remaining six of eleven simulations also formed at least one interstitial atom, though these occurred at stress intensities between $0.23 - 0.34$ eV/Å$^{2.5}$. The nucleation and subsequent movement of the Lomer dislocation appeared to initiate amorphization near the crack tip. In all specimens, glissile Shockley partial dislocations of pure edge character were nucleated at the crack tip on the $(\bar{1}\bar{1}1)$ slip plane (leading partials) intersecting the crack front. The partial dislocations had Burgers vectors of $\frac{a}{6}[\bar{1}\bar{1}\bar{2}]$ and their nucleation usually occurred after the crack tip became amorphous. The nucleation of subsequent partial dislocations of the same character on successive slip planes (twinning partials), led to the formation of nanotwins in ten of the eleven simulations. As the applied loading was increased, the amorphous zone increased in size, extending in the [110] direction, and the width of the twin continued to grow via the nucleation of additional twinning partial dislocations (to a width of at least six dislocations). At loads near 0.36 eV/Å$^{2.5}$ the crack propagated along the [110] direction to the MD-DD interface. The simulation that did not twin on the inclined slip plane instead nucleated a

trailing partial dislocation, forming a full dislocation on the inclined plane, at a stress intensity of 0.27 eV/Å$^{2.5}$, then twinned on the slip plane parallel to the crack plane at a stress intensity of 0.32 eV/Å$^{2.5}$. The evolution of the amorphous zone from the first interstitial atoms to the propagating crack is illustrated in Figure 3.7.

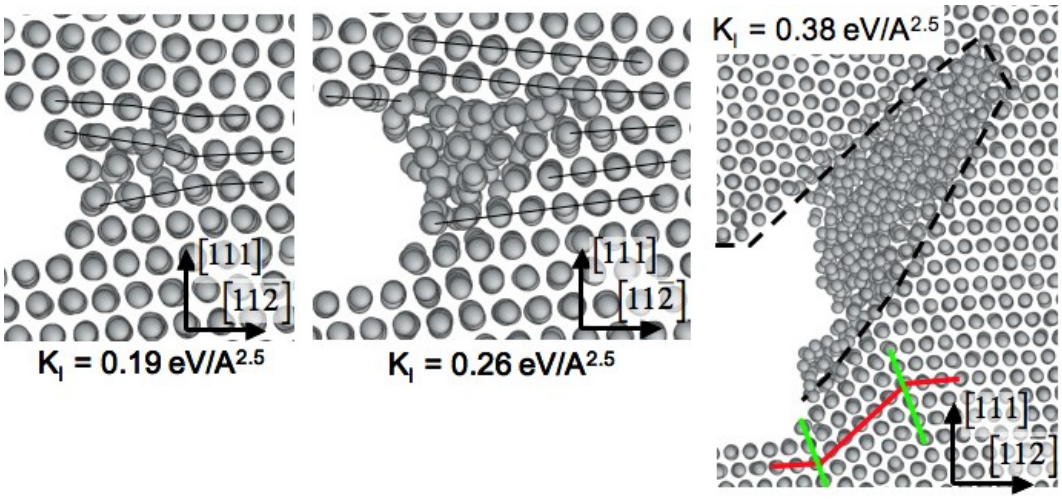

Figure 3.7: A typical progression of the crack tip when simulated at a loading rate of 1×10^9 eV/Å$^{2.5}$/sec. The 3D atomic structure is projected onto 2D for easy visualization. At a load of 0.19 eV/Å$^{2.5}$ a Lomer dislocation is formed along with a few interstitial atoms. As the load is raised to 0.26 eV/Å$^{2.5}$, the Lomer dislocation becomes an amorphous zone extending from the crack surface. At a load of 0.38 eV/Å$^{2.5}$, the sample has formed a small twin (the twin boundaries are highlighted with green lines and the change in lattice orientation with a red line), and the amorphous zone has started to grow in the [1 1 0] direction and detach from the crystalline material propagating the crack front.

Rate of 1×10^8 eV/Å$^{2.5}$/sec

Six simulations were performed at a loading rate of 1×10^8 eV/Å$^{2.5}$/sec using the combined parallel replica hyperdynamics acceleration scheme. At this rate, the deformation mechanisms were similar to the fastest loading rate simulations. A Lomer dislocation nucleated first in three of six simulations, with

at least one surface atom moving to subsurface interstitial sites immediately in one case. All of the simulations produced Lomer dislocations with at least one interstitial atom by a load of 0.22 eV/Å$^{2.5}$, which lead to significant disorder of the crack tip. In three cases, a stacking fault on the inclined slip plane was the first event. In all cases a twin was nucleated on the inclined slip plane by the nucleation of several successive leading partial dislocations. In only one instance out of six did the crack tip nucleate a full dislocation before twinning. In another instance, a full dislocation was nucleated on the $(\bar{1}\bar{1}1)$ plane above the crack after the crack tip had become significantly disordered. In one simulation the crack propagated along the (001) plane in the [110] direction at a load of 0.36 eV/Å$^{2.5}$ as the amorphous region detached from the crystalline region. In three of the six simulations the amorphous zone transitioned into a 3D dislocation structure with stacking faults on slip planes that were oblique to the crack front. These dislocations are constrained by CADD's thin out-of-plane thickness, and are likely an artifact of the periodic boundary conditions. Figure 3.8 includes a snapshot of the 3D dislocation structure from the simulation where the crack propagated. The formation of these oblique dislocations suggests a picture of the system evolving from a high energy configuration with an amorphous zone to a lower energy configuration of dislocations, given enough time for the nucleation kinetics to proceed. The time required for the edge of the amorphous zone to transition into oblique dislocations appears to be on the order of tens of picoseconds, with the transition not having occurred in any of the 1×10^9 eV/Å$^{2.5}$/sec simulations discussed earlier.

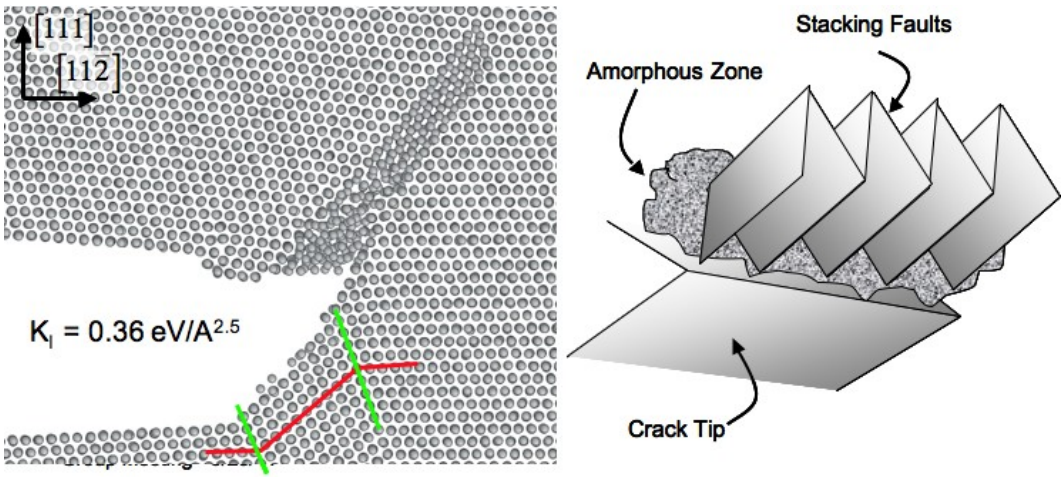

Figure 3.8: A typical amorphous crack tip for a simulation with a loading rate of 1×10^8 eV/Å$^{2.5}$/sec. Twin boundaries are highlighted with green lines and the lattice orientation change is illustrated with a red line. The amorphous zone extends in the [1 1 0] direction and has formed a 3D dislocation structure at the farthest point. The cartoon to the right shows how the dislocation structure would look from an oblique angle given the periodic boundary conditions of the system.

Rate of 1×10^7 eV/Å$^{2.5}$/sec

Six independent simulations were conducted at a loading rate of 1×10^7 eV/Å$^{2.5}$/sec using the combined parallel replica hyperdynamics acceleration scheme. Lomer dislocations and crack tip twinning were again observed. However, at this rate, Lomer dislocations remained near the crack surface and did not lead to the formation of a large amorphous zone. In two simulations interstitial atoms (that accumulated at the Lomer dislocations) eventually moved back to the surface, while in two different simulations only one or two interstitial atoms were formed, making the distortion of the lattice local to the dislocation core. Half of the simulations produced subsurface interstitial atoms with the nucleation of the first Lomer dislocation. In one instance, a full dislocation was nucleated on the $(\bar{1}\bar{1}1)$ slip plane above the crack tip from an undistorted region

of the crack face. The full dislocation decomposed to form a full dislocation on the (111) plane and a Lomer dislocation with Burgers vector $\frac{a}{6}[110]$ on the (001) plane. Figure 3.9 illustrates the event schematically. It is worth noting that the orientation of the plane of maximum shear stress changes with distance away from the crack tip on the $(\bar{1}\bar{1}1)$ plane in a way that is consistent with the dislocation reaction. This behavior did not occur in the simulations conducted at rates of 1×10^9 eV/Å$^{2.5}$/sec or 1×10^8 eV/Å$^{2.5}$/sec. The observance of full dislocation nucleation as opposed to twinning at lower rates is completely consistent with the conclusions of [111, 112].

Rate of 1×10^6 eV/Å$^{2.5}$/sec

Four independent simulations were performed at the lowest loading rate studied here using the combined parallel replica hyperdynamics acceleration scheme. Lomer dislocations, twinning, and subsurface interstitial atoms were still observed, but occurred less frequently. Interstitial atoms were formed in one of four simulations, and twinning was observed in two of four simulations. In three simulations, Lomer dislocations were formed first. In one case, the nucleation coincided with the formation of a few interstitial atoms, while in both of the other cases the Lomer dislocation dissociated into dislocations on glide planes (stacking faults or full dislocations) within 20 nanoseconds. This transition was not observed at any of the lower loading rates, possibly because of a long characteristic reaction time or by the frequent presence of interstitial atoms around the dislocation core observed at higher loading rates. In two cases, no twinning was observed, rather only full dislocation nucleation. In two simulations, full dislocations above the crack plane nucleated full dislocations in the

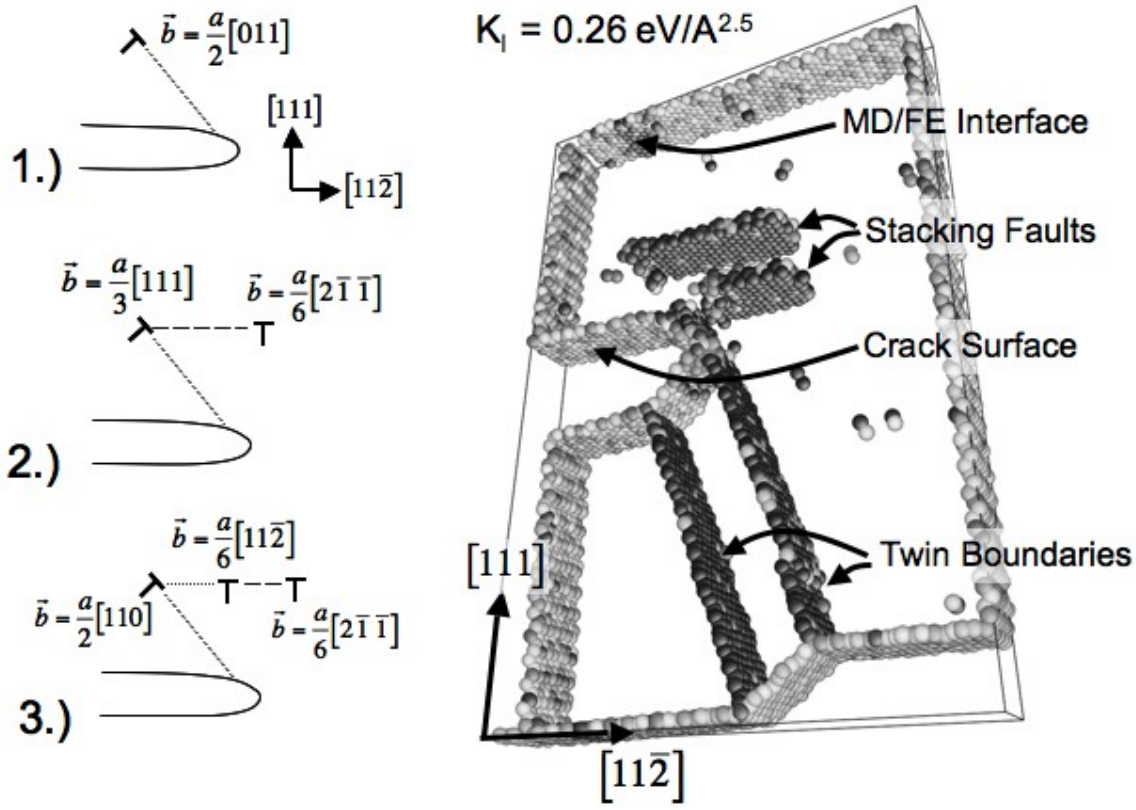

Figure 3.9: A snapshot of the simulation at a loading rate of 1×10^7 eV/Å$^{2.5}$/sec that formed full dislocations. Only the atoms not in perfect fcc stacking are shown [64], e.g. stacking faults, twin boundaries, strong thermal fluctuations, and free surfaces. The twin boundaries extend toward the lower right, while the full dislocations are in the slip plane parallel to the crack plane. The outside surface is the interface between the atomistic and continuum regions. The cartoon to the left shows the dislocation reaction that produced the full dislocations in the image on the right.

(111) plane, leaving Lomer dislocations as observed in the 1×10^7 eV/Å$^{2.5}$/sec sample. Figure 3.10 provides snapshots of full dislocation nucleation and interstitial atoms from theses simulations.

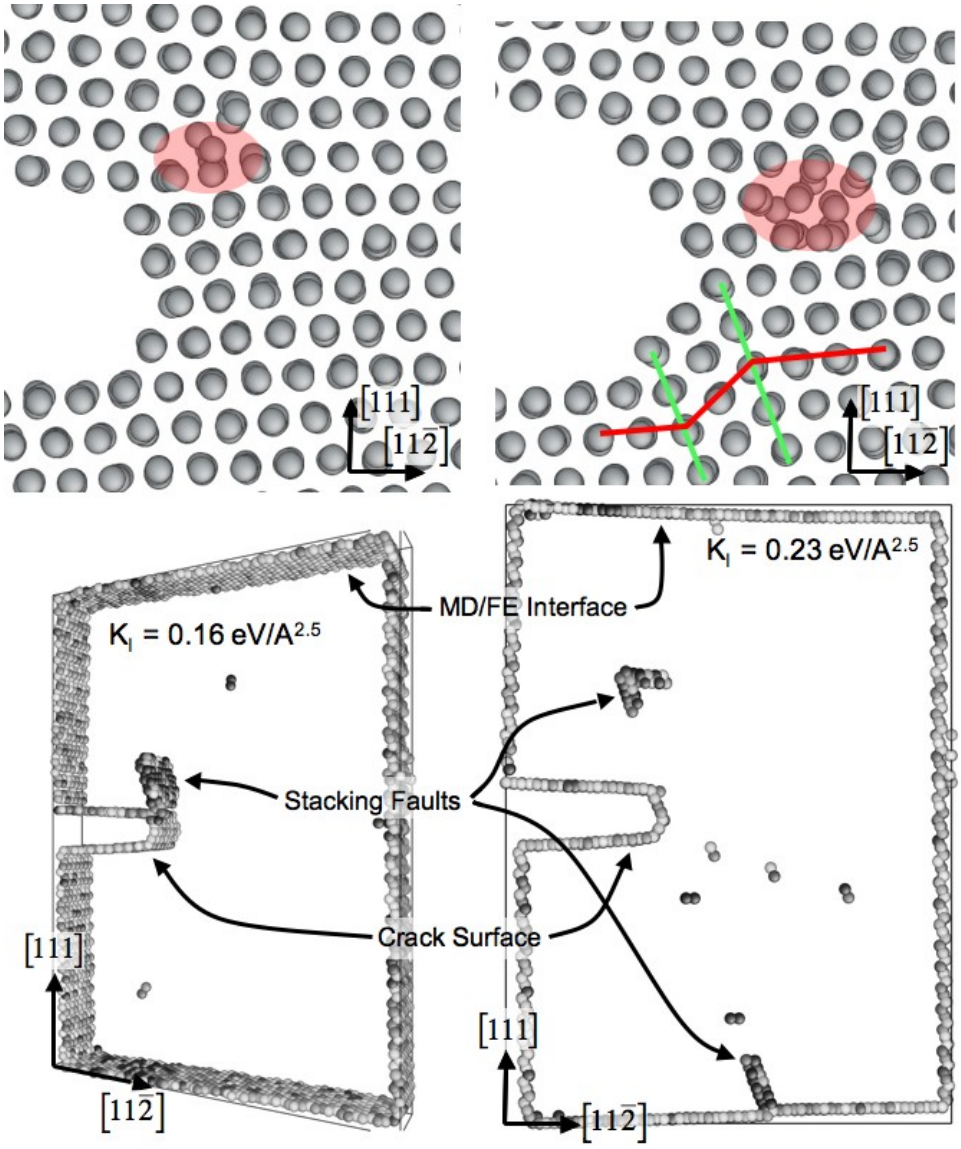

Figure 3.10: Two typical configurations from the simulations performed at a rate of 1×10^6 eV/Å$^{2.5}$/sec. The upper left image shows a Lomer dislocation with an interstitial atom in the highlighted region. The image on the upper right shows the same crack tip where the dislocation has moved and produced more interstitial atoms at the dislocation core. Also, a small twin has formed on the inclined slip plane intersecting the crack front. The bottom images show full dislocations being nucleated above and below the crack tip, with only atoms not in perfect fcc stacking being shown, as in Figure 3.9. The dislocation above the crack tip follows the same dislocation transition as the full dislocations in Figure 3.9.

3.7 Conclusions

In total, this effort sought to simultaneously utilize several techniques to extend the timescale of MD modeling to enable the atomic processes associated with crack tip behavior to be studied at loading rates more typical of experiments. By performing a collection of simulations spanning various loading rates, the work provides new insight into the effects of loading rate on crack tip behavior and more generally illuminates the potential for performing MD studies of the deformation and failure processes at ordinary laboratory timescales in the future.

At the fastest loading rates typical of traditional MD, the crack tip configuration examined here first nucleated a Lomer dislocation upon ramped loading. In conjunction with the nucleation process, surface atoms near the crack tip were observed to move to subsurface interstitial sites. These events were shortly followed by the formation of an amorphous zone that grew in size as the load was increased. Eventually the amorphous zone provided a path for the crack to propagate when the load was raised above 0.3 eV/Å$^{2.5}$. While the amorphous zone was observed in simulations both with and without parallel replicas and hyperdynamics, amorphization at Al crack tips is not well documented in the literature. We believe that its occurrence in these simulations is related directly to the high loading rate at finite temperature. Specifically, the temporary movement of surface atoms to interstitial sites destabilizes the lattice in the presence of a rapidly increasing hydrostatic stress state at the crack tip, relative to the timescale of interstitial migration.

As the loading rate is decreased from 10^9 to 10^6 eV/Å$^{2.5}$/sec, fewer subsur-

face interstitial atoms were observed, the amorphous zone become less prevalent, and dislocation reactions occurred forming mobile dislocations. The trend is indicative of the crack tip region transitioning to lower energy configurations as the timescale increased for thermal activation to occur. Twinning dislocations and Lomer dislocations were observed across all loading rates. However, as the loading rate was decreased the occurrence of full dislocation slip increased relative to twinning, consistent with previous studies. A summary of the observed mechanism across the range of loading rates examined here is given schematically in Figure 3.11.

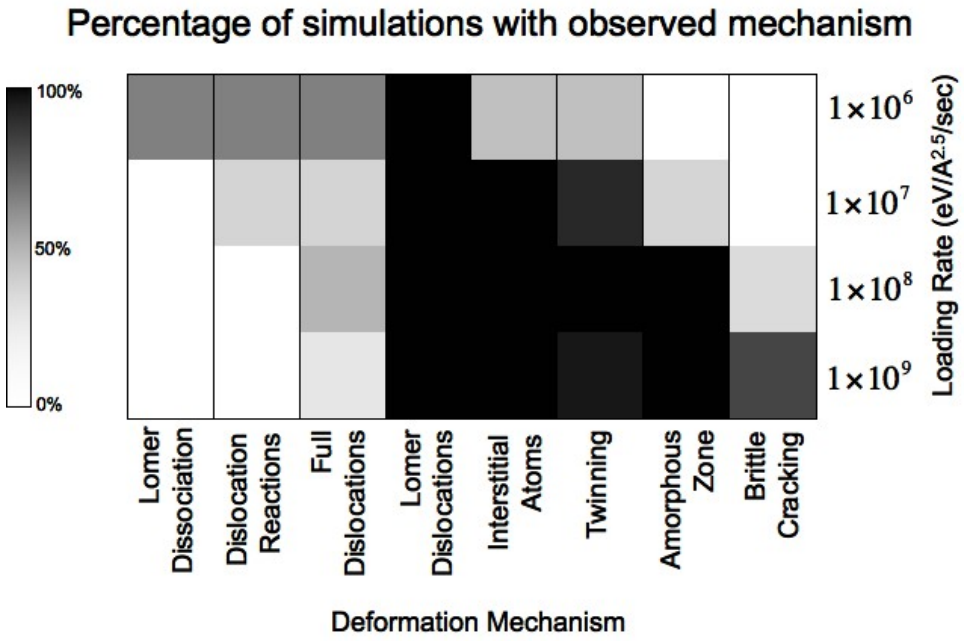

Figure 3.11: A pictorial representation of the mechanisms observed over different loading rates. The color corresponds to the percentage of simulations that contained a given event. Some mechanisms are obviously rate dependent, like full dislocation nucleation and the formation of the amorphous zone which leads to brittle cracking. Mechanisms like Lomer dislocation and twin nucleation are prevalent in the current lattice orientation, however, they show some rate dependance at slow loading rates. The mechanisms are aligned generally so that more common mechanisms at slower rates are towards the left, and mechanisms more common of faster rates are towards the right.

The performance of the bond-boost hyperdynamics method varied widely for the aluminum crack tip system studied here. Average boost factors ranged from 2.0 to 31.7 with a mean of 11.4 and a standard deviation of 7.6. These values are dramatically smaller than those obtained for other systems involving surface diffusion [32, 72, 82] and dislocation nucleation in nickel. In the case of leading partial dislocation nucleation in nickel, the difference between nickel and aluminum at room temperature can be attributed to the relatively high stable stacking fault energy in aluminum. This limits nucleation in aluminum to loads that are a significant fraction of the critical load, where the nucleation energy barrier is small and the bond boost approach is less effective [111]. With regard to surface diffusion, the saddle state can be more effectively described using bond strain compared to the case of dislocation nucleation, thus, a greater benefit from the bond boost can be obtained. Other hyperdynamics approaches, like the adaptive strain-boost method [40], address this issue by specifically focusing on the dislocation nucleation processes. However, such approaches may then be biasing the system away from diffusive processes such as interstitial migration. Other formulations of hyperdynamics have recently been proposed such as path integral hyperdynamics [16] and dividing surface free hyperdynamics [56]. Both aim to remove or lessen the restrictions on the hyperdynamics boost potential. While it is clear for the complex crack tip application studied in this work that further advancements in the methodology and/or application of hyperdynamics are needed to truly enable simulations to connect to everyday experimental timescales, the most effective route forward remains unclear.

While hyperdynamics performance remains consistent across different loading rates, the performance of the combined parallel replica and hyperdynamics methodology deteriorates rapidly as the number of parallel replicas is increased.

This problem is inherent to the method since a fixed amount of time spent using traditional MD is needed after each transition, and transitions happen more rapidly as the amount of acceleration is increased. This problem is hard to remedy since the purpose of the study is to simulate as many transitions as possible at timescales that require accelerated dynamics. Since an increase in the boost factor alone fails to improve the overall effectiveness of the method, a substantial change to the methodology is likely required for the study of timescales beyond those examined here. The most direct solution may be to define coarser less frequent transitions that include several small frequent transitions. For example, the movement of interstitial atoms from the bulk to the crack surfaces may be considered a diffusive transition that is made of several bond breaking events.

In practice, the design of hyperdynamics potentials is quite difficult. First, the mechanisms and transition states are unknown at the outset of the simulation. Second, the creation of a boost potential that does not bias the system toward any particular mechanism seems nearly impossible. Third, it is difficult to develop a boost potential that is efficient for multiple mechanisms. The bond-boost potential has the benefit that it only tracks the stretching of bonds, which is inherent to all configurational changes. However, this generality and inherent scale limits its efficient application to systems that involve transitions where only a few bonds are involved. The crack tip system studied here is particularly challenging since it contains deformation mechanisms with a range of activation volumes having different stress dependencies, e.g. dislocation nucleation v.s. interstitial migration.

Dynamic tests of aluminum alloy 2024-T3 show that rate independent

measurements of bulk critical stress intensities is achieved around 1×10^4 eV/Å$^{2.5}$/sec [79]. This is still two orders of magnitude slower than the stress intensity rates used in this work. While this only gives an estimate of when mechanical property measurements at the nano-scale will be rate independent, there is still hope that accelerated dynamics schemes can be used to study deformation at bulk experimental loading rates. Even at a loading rate of 1×10^6 eV/Å$^{2.5}$/sec plasticity generated by the nucleation and glide of full dislocations is becoming more dominant despite the sample being oriented more favorably for twinning. Further work is clearly needed to develop more efficient methods to explore the deformation of aluminum crack tips at time scales relevant to typical physical experiments performed in the laboratory.

3.8 Acknowledgements

The authors gratefully acknowledge support from Ed Glaessgen and Steve Smith at NASA (Grant No. NNX08BA39A), Paul Hess at the Office of Naval Research (Grant No. N000141010323), and Ali Sayir at the Air Force Office of Scientific Research (Grant No. FA95501110273).

CHAPTER 4

EXAMINING THE MECHANISMS OF NEAR THRESHOLD FATIGUE CRACK GROWTH IN ALUMINUM ALLOYS WITH ATOMISTIC SIMULATIONS

By Kristopher Baker and Derek H. Warner

4.1 Abstract

Though numerous experiments and numerical models have been used to study fatigue crack growth in aluminum alloys, the atomic-scale mechanisms by which a fatigue crack will grow still remains unclear. Using CADD, a multiscale approach combining molecular dynamics and discrete dislocation dynamics, the effect of dislocation pileups on atomic-scale mechanisms of fatigue crack growth is investigated by varying the friction force applied to dislocation glide. The simulations indicate that the threshold for fatigue crack growth increases with an increase in monotonic friction force, and a transition from stage I to stage II type fatigue crack growth is observed when dislocations shield the crack tip from nucleating dislocations on the primary slip system. Three main mechanisms of fatigue crack growth are observed: cleavage along the primary slip plane followed by blunting, crack extension by bond breaking with the activation of multiple slip systems at the crack tip, and incremental growth of the crack by opening along nearby lattice defects. It is proposed that the threshold for fatigue crack growth is controlled by spacing of the copper precipitates, and that material heterogeneity must be considered to accurately model fatigue crack growth in aluminum alloys.

4.2 Introduction

Al-Cu alloys continue to serve as the primary material system for many critical components in aircraft structures. Accordingly, a key aspect of aircraft safety involves the prediction of fatigue crack growth (FCG) in these materials. This technological motivation has spurred the growth of a vast library of experimental and theoretical studies on FCG over the past decades. Nonetheless, one critical aspect of the phenomenon has remained particularly unclear, i.e. the atomistic mechanism by which the crack tip propagates forward under cyclic subcritical loadings.

Considering the atomic nature of crack tip processes, atomistic modeling can offer significant insight into the process. However, interpreting the model results relative to FCG in real Al-Cu alloys involves many significant challenges. One of the largest challenges is the limited spatial domain of atomistic models, which can artificially influence the movement of dislocations away from the crack tip and ultimately bias crack tip behavior [31]. Discrete dislocation (DD) dynamics simulations are not generally plagued by this problem as they enable a much larger spatial domain to be simulated, while still explicitly modeling every dislocation. However, DD models do not explicitly represent the atomic scale complexities that occur at a crack tip [23, 24, 25, 26, 17], and thus cannot illuminate the atomic mechanisms by which a crack tip evolves to cause FCG.

In this work, a concurrently coupled atomistic-discrete dislocation multiscale method (CADD) is used to resolve the shortcomings of tradition atomistic and DD simulations with the specific goal of illuminating the atomic scale mechanisms that occur at a crack tip during FCG. The model involves a pristine

aluminum crystal with a crack loaded in mode I. Upon loading, dislocations are nucleating at the crack tip in the atomistic region of the model. In most cases, the dislocations then glide into the nearby DD region where their motion is inhibited by an imposed glide resistance, which is taken as a variable parameter which we study. For Al-Cu alloys, the glide resistance can be associated with Cu solutes and precipitates inhibiting dislocation motion. Thus, by studying how the resistance to dislocation glide effects crack tip response under cyclic loading, this work investigates the effect of age hardening on FCG, something for which experimental results exist.

The manuscript focuses on two key components of the results emerging from our models. The first is the identification of the atomistic mechanisms by which a crack tip propagates forward in a ductile metal subjected to cyclic loading. The second is the dependence of the crack tip mechanisms on dislocation glide resistance, which leads us to propose that it is the heterogeneity of glide resistance that is responsible for the dependence of the near threshold FCG rate on aging time observed in experiments.

4.3 Methods

A concurrent multiscale simulation approach, described in the next section, is used to connect an atomistic region encompassing an aluminum crack tip with discrete dislocation dynamics capable of holding dislocation pileups microns in length. This methodology allows the direct interaction of the crack tip deformation and the dislocations nucleated naturally by the crack tip. Pileups of dislocations are caused by a friction force applied homogeneously throughout

the discrete dislocation portion of the simulation. Only when the driving force is greater than the friction force is the dislocation allowed to move.

In the simulations from this work, the friction force can be thought of in two ways based on the proximity to the crack tip. Close to the crack tip, just past the MD and DD interface, the immediate application of the friction force can represent an immediate interaction with an obstacle, or field of obstacles, with a prescribed resistance to dislocation motion, i.e. a precipitate with a given dislocation cutting strength. As a reference, Singh and Warner have calculated the resistance of copper precipitates or solid solution to dislocation glide with MD or *ab initio* methods [95]. They find that a field of copper solute atoms provides a resistance of approximately 75 MPa, GP zones a resistance of 100-300 MPa, and θ'' precipitates a resistance of 100-500 MPa depending on their size and density. As a contrast, far from the crack tip when dislocations must move through a large field of precipitates, the friction force can be thought of as an average slip resistance provided by the larger-scale precipitate microstructure. In this case, age hardness data can be used to find an average shear strength of the material, which can be applied as a friction force. In the current simulations, the closest dislocations are the most relevant to the crack tip processes, however the pileup can often reach microns into the material. Since a constant friction force is used throughout the simulation domain, one must consider both near and far interpretations of the friction force.

4.3.1 CADD Concurrent Multiscale Method

The underlying theory of the multiscale method is built upon the Coupled Atomistic Discrete Dislocation (CADD) framework of Shilkrot et al. [93, 92], with the molecular static atomistic region of CADD being replaced by a MD atomistic region as detailed in [84]. The CADD coupling methodology consists of solving two distinct problems, involving a MD and continuum region that are coupled by self-consistent displacement boundary conditions. The MD region is composed of a set of atoms bounded by a set of interface atoms/nodes. The DD continuum region is approximated by finite elements and thus the fields associated with it are a function of the corresponding nodes. The interatomic force, $\mathbf{F}$, experienced by each atom within the MD region results from interactions not only within the MD region and its bounding interface, but also interactions with pad atoms that extend into the continuum. However unlike the atoms in the MD and interface regions, the positions of the pad atoms are controlled by the continuum solution. Thus the pad atoms provide the necessary nonlocal boundary conditions across the interface to the MD and interface regions. While the CADD methodology is not specific to any particular interatomic force model [76, 75], this work utilizes embedded atom empirical potentials to model interatomic forces [28].

Both the interface atoms and those within the MD region are modeled with Langevin dynamics,

$$\ddot{\mathbf{x}} = \frac{\mathbf{F}}{m} - \gamma\dot{\mathbf{x}} + \chi\frac{\mathbf{F_A}}{m}, \tag{4.1}$$

where $\ddot{\mathbf{x}}$ is the acceleration of the particular atom, $\dot{\mathbf{x}}$ the velocity, $\mathbf{F}$ the force, m the mass, γ is a damping coefficient, χ a uniform random number between

$-1 \leq \chi \leq 1$, and $\mathbf{F_A}$ the applied random force. The components of $\mathbf{F_A}$ are

$$F_{Ai} = \sqrt{\frac{6\gamma m k_B T_0}{\Delta t}}, \quad i = x, y, z, \tag{4.2}$$

which produces a canonical ensemble where k_B is Boltzmann's constant, T_0 the desired equilibrium temperature, and Δt the MD time step. The applied damping coefficient, γ, is a function of position,

$$\gamma = \gamma_0 \left[1 - \frac{d(x,y)}{w}\right], \tag{4.3}$$

where γ_0 is the maximum damping coefficient, w is the width of the damped 'stadium' region, and $d(x,y)$ is the minimum distance from the atom to the MD/DD interface,

$$d(x,y) = \text{abs}\left(\min\left(x - x_{min}, x - x_{max}, y - y_{min}, y - y_{max}, w\right)\right). \tag{4.4}$$

The damping coefficient field provides maximum damping (or thermostating) at the MD-DD interface, decreases linearly with distance away from the interface, and is zero at distances greater than w away from the interface. This approach provides a relatively constant equilibrium temperature across the MD region while minimally affecting the natural dynamics of the system away for the MD-DD interface. A detailed analysis of the approach is given in [84].

The response of the continuum region is local, and therefore, it is only a function of the boundary conditions and the resulting deformation within that region. The continuum region is assumed to be in elastic equilibrium, such that the energy functional associated with the region is always minimized,

$$E^c = \frac{1}{2}\int_{\Omega_c} (\hat{\boldsymbol{\sigma}} + \tilde{\boldsymbol{\sigma}}) : (\hat{\boldsymbol{\epsilon}} + \tilde{\boldsymbol{\epsilon}})\, \mathrm{d}V - \int_{\partial\Omega_T} \mathbf{T_0}\,(\hat{\mathbf{u}} + \tilde{\mathbf{u}})\, \mathrm{d}A, \tag{4.5}$$

where Ω_c represents the continuum domain and $\partial\Omega_T$ represents the boundary of the continuum domain on which a traction boundary condition, $\mathbf{T_0}$, exists. $\tilde{\boldsymbol{\sigma}}$, $\tilde{\boldsymbol{\epsilon}}$,

and $\tilde{\mathbf{u}}$, represent infinite medium stress, strain, and displacement fields, respectively, generated from the discrete dislocations at distinct locations. $\hat{\boldsymbol{\sigma}}$, $\hat{\boldsymbol{\epsilon}}$, and $\hat{\mathbf{u}}$ represent the solution fields from an anisotropic linear elastic boundary value problem that when superimposed with the dislocation fields satisfy the overall boundary conditions. $\hat{\boldsymbol{\sigma}}$, $\hat{\boldsymbol{\epsilon}}$, and $\hat{\mathbf{u}}$ are obtained using a standard displacement based finite element approach, while $\tilde{\boldsymbol{\sigma}}$, $\tilde{\boldsymbol{\epsilon}}$, and $\tilde{\mathbf{u}}$ are well known analytic fields [104]. The position of the dislocations within continuum domain evolve following

$$\mathbf{r}^i_{new} = \mathbf{r}^i_{old} + B\left(f^i \frac{\mathbf{b}^i}{|\mathbf{b}^i|}\right) \tag{4.6}$$

where $\mathbf{r}^i_{new}$ is the new position of dislocation i, $\mathbf{r}^i_{old}$ is the position of dislocation i from the previous update step, $\mathbf{b}^i$ is the Burgers vector of dislocation i, B is the mobility factor, and f^i is the Peach Koehler force of dislocation i given by

$$f^i = \left(\mathbf{n}^i\right)^T \left(\hat{\boldsymbol{\sigma}} + \sum_{j \neq i}^{N} \tilde{\boldsymbol{\sigma}}^j\right) \mathbf{b}^i \tag{4.7}$$

where $\mathbf{n}^i$ is the normal vector to the glide plane of dislocation i, $\hat{\boldsymbol{\sigma}}$ is the stress field calculated from the boundary value problem, and $\tilde{\boldsymbol{\sigma}}^i$ is the stress field generated by dislocation i. When a dislocation approaches the MD-DD interface, dislocations are passed across it via the insertion of a dislocation dipole. The insertion of a symmetric dislocation dipole that spans the interface and lies on the plane of the dislocation to be passed effectively moves the dislocation to the other side of the interface. The details of this procedure are given in [92].

The CADD algorithm used here can be summarized as follows:

1. A brief period of MD is performed on the MD and interface regions with the pad atoms remaining fixed to serve as boundary conditions. It is during this period that the simulation time is accumulated.

2. The averaged positions of the interface atoms over the previous period of dynamics are used to define the displacements of interface nodes which serve as Dirichlet boundary conditions for the continuum boundary value problem. The energy functional given in equation 4.5 is then minimized to obtain a solution using standard linear elastic finite element analysis.
3. The position of the discrete dislocations in the continuum region are updated following Equation 4.6.
4. The positions of the pad atoms are updated in accordance with the continuum solution.
5. Return to step 1.

A significant approximation in the current modeling framework is that the DD region can only accommodate in-plane displacement fields. This creates an inconsistency between the fully 3D MD and 2D DD regions. The effect of the inconsistency is that dislocations with a screw Burgers vector component relative to the planar FE region emitted from the crack tip experience a repulsive image force from the MD/DD interface. For the specific geometry and loading considered in this work, dislocations with screw character play a secondary role and their behavior has been shown to not be significantly affected by the artificial image forces by examining parametric studies involving the size and shape of the MD region. However, the incorporation of out-of-plane displacements in the DD region is important in general, and as such we plan to implement this feature in the future.

4.3.2 Simulation Setup

Even though thermal activation is important for fatigue crack growth in aluminum alloys [113], the simulations conducted in this study use zero temperature. Considering that fatigue at colder temperatures tend to raise threshold values from less thermal activation and more reversibility [67], one must be careful when relating zero temperature MD simulations to experimental data. Initial attempts were done using an combined time and spatial multiscale method [9], however the method proved to be far too inefficient for the observed mechanisms of fatigue crack growth.

The specimen consisted of an FCC crystal with an edge crack. The crystal lattice was oriented such that the horizontal axis corresponded with $\left[47\bar{1}\right]$, the vertical axis with $\left[\bar{1}13\right]$, and the out of plane direction with $\left[2\bar{1}1\right]$. The crack was created by removing 3 consecutive planes of atoms. The crack plane was normal to the vertical axis with the crack front aligned with the $\left[2\bar{1}1\right]$ direction. The $\left(\bar{1}\bar{1}1\right)$ slip plane intersected the crack plane at an angle of 58.5 degrees from the horizontal, with the [011] slip direction in the x-y plane. All other slip planes are oblique to the x-y plane, so that the primary slip plane is the $\left(\bar{1}\bar{1}1\right)$ plane and the primary slip direction is the [011] direction. This orientation was chosen because full dislocations with no screw component are nucleated from the crack tip, thus no artificial image force acts on dislocations approaching the MD/DD interface.

Using CADD, the crack tip at the center of the specimen was embedded into a 3D atomistic region of approximately 150 × 150 × 10 Å, which was encompassed by a larger 2D plane strain, DD continuum region spanning 2 × 2 × 0.001 microns. The elastic constants of the continuum material were $C_{11} = 0.682$,

$C_{12} = 0.331$, $C_{44} = 0.180$ eV/Å^3, while the atomistic region is defined by an aluminum potential from Ercolessi and Adams (1994) [28]. The temperature of the MD region was controlled via the ramped Langevin thermostat described previously, with T=1 K. The lattice constant at 0 K was 4.03208 Å. Loads were applied by prescribed displacements at the outer boundary of the DD region corresponding to the continuum solution for a crack in an anisotropic linear elastic material subjected to mode I loading. The interface updating in CADD was done in every MD step. The simulation setup was the same for all simulations, with a range of different friction forces used for each loading condition. The simulations include prescribed loads of $\Delta K_I = 0.4, 0.5, 0.6$ eV/Å$^{2.5}$ with $R = 0$, and $\Delta K_I = 0.2, 0.3, 0.4, 0.5$ eV/Å$^{2.5}$ with $R = 0.25$.

In order to simulate precipitation hardening a friction force is added to the DD region of CADD that corresponds to the shear stress required for dislocations to pass through a field of obstacles. Using age hardness data from aluminum alloy 2024 and Al-4% Cu systems, vickers hardness, H_v, can be related to uniaxial yield stress, σ_y, with

$$H_v = c_{vp}\sigma_y. \tag{4.8}$$

The constant c_{vp} usually falls between 0.21 and 0.4 [95]. The value of $c_{vp} = 0.31$ is used as an average value. Using the uniaxial yield stress, the shear stress required for dislocation motion, τ_y, can be calculated by

$$\sigma_y = \sigma_{y0} + T\tau_y, \tag{4.9}$$

where the Taylor factor, T, is taken as $T = 3.06$, and $\sigma_{y0} = 20$ MPa as a representative value as used by Singh and Warner [95]. Using Equations 4.8 and 4.9, vickers hardness values of $H_v = 100$, $H_v = 122.6$, and $H_v = 141.6$ correspond to dislocation flow stresses of $\tau_y = 75.76$ MPa, $\tau_y = 94.33$ MPa, $\tau_y = 110.00$ MPa

respectively. As a reference, the peak hardness of aluminum alloy 2024-T3 is around 137 [22], while the hardness of Al-4% Cu systems with primarily GP zone precipitates is around 100 [94]. The hardness value of 122.6 was used as an intermediate to these values. Using line tension models of dislocations cutting line-segment obstacles, Singh and Warner [95] calculate the shear stress needed for dislocations to overcome copper precipitates corresponding to different age hardnesses. They use Equations 4.8 and 4.9 and find excellent agreement with experimental age hardness curves of Al-4% Cu systems. To simulate the immediate interaction with a precipitate, friction forces of 200, 300, 400, 500, 600, 700, 800, 900, and 1000 MPa were also used. Values from 200-300 MPa correspond to the cutting strength of GP zones, while values up to 500 MPa correspond to θ'' precipitates. Values above 500 MPa represent other possible obstacles like large inter-metallic particles, or θ' precipitates.

4.4 Results and Discussion

At low friction forces, multiple dislocations are nucleated along the inclined slip plane. They glide away from the crack tip, and do not significantly shield the nucleation of subsequent dislocations. As bonds break at the crack tip from dislocation nucleation, dislocations on slip planes oblique to the crack front can be nucleated. The oblique dislocations do not travel far, and some interact with dislocations nucleated on the primary slip plane creating sessile dislocation junctions. In some cases, dislocations nucleated on an oblique slip plane will compress to a tight core and nucleate another full dislocation on the primary slip plane. This dislocation reaction creates a sessile Lomer dislocation and the newly nucleated full dislocation will propagate easily away from the

crack tip. This mechanism is observed using the same interatomic potential in a similar study at finite temperature [9]. Often, large crack tip shape changes will cause atoms near the crack surface to deform by localized bond breaking and shifting as seen in Figure 4.1. As the region of bond shifting grows, the crack shape tends to blunt. When loaded further, crack nucleation along the inclined slip plane $\left(\bar{1}\bar{1}1\right)$ is observed in many cases. Considering that distant dislocations do not significantly shield the crack tip, it seems that the change in mechanisms from dislocation nucleation to brittle crack growth is due to a change in crack tip shape with dislocation nucleation. This is consistent with literature that has suggested the importance of crack tip shape on crack tip deformation mechanisms [10, 33, 100, 39]. Figure 4.2 shows the creation of a sharp crack tip from the nucleation of three dislocations that later propagates along the primary slip plane.

The competition between brittle cracking along the inclined $\left(\bar{1}\bar{1}1\right)$ slip plane versus the $\left(\bar{1}13\right)$ crack plane can be predicted based on the surface energy and angle of the crack planes. Since the surface energy of the $\left(\bar{1}13\right)$ plane is nearly an order of magnitude larger than the $\left(\bar{1}\bar{1}1\right)$ plane, brittle crack growth is always preferred on $\left(\bar{1}\bar{1}1\right)$ slip plane. This, however, does not prevent the crack from growing along the $\left(\bar{1}13\right)$ plane, since bonds are broken at the crack each time a dislocation is nucleated. If the atomic lattice at the crack tip is heavily populated with defects created from dislocation nucleation, the surface energy for the crack tip to propagate forward through the defected lattice can be lowered to make crack growth more favorable along the $\left(\bar{1}13\right)$ plane (Figure 4.3). When the crack does propagate in a brittle manner in the primary slip plane, the propagation arrests within a few nanometers. The interaction of the crack with sessile lattice defects, like the dislocation junctions and bond shifting men-

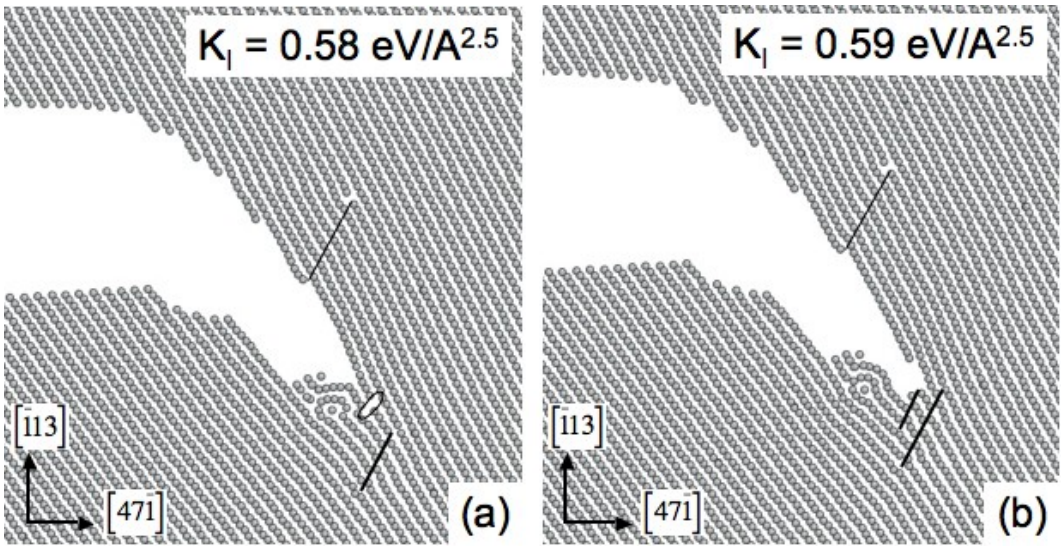

Figure 4.1: Snapshot of simulation with $\Delta K_I = 0.6$ eV/Å$^{2.5}$, $R = 0$, and friction force = 400 MPa showing the crack opening along a lattice defect in the second cycle. Bond breaking and shifting of the lattice at the crack surface is observable on the lower crack face near the crack tip. a) The crack has a sharp tip, and a small void is present near the tip, circled with a solid line. Solid straight lines indicate slip on oblique slip planes. b) The crack has opened along the slip plane and connected with the lattice defect. Again, straight lines indicate slip on planes oblique to the crack plane. All images of the atomistic region are plotted with AtomEye [64].

tioned previously, often stops the crack. Conversely, depending on the specific character and location to the crack tip, lattice defects can also act as weak areas promoting continued crack growth, also illustrated in Figure 4.1. When a crack has interacted with a defect, it may arrest or nucleate dislocations, usually on the inclined slip plane (since the primary slip plane is blocked). Figure 4.4 shows a defect blocking dislocation propagation leading to brittle crack growth, and the resulting blunted crack configuration after the nucleation of oblique dislocations.

Upon unloading, if the cracks along the $\left(\bar{1}\bar{1}1\right)$ plane have blunted the crack will not close and permanent crack growth is observed at the end of the cy-

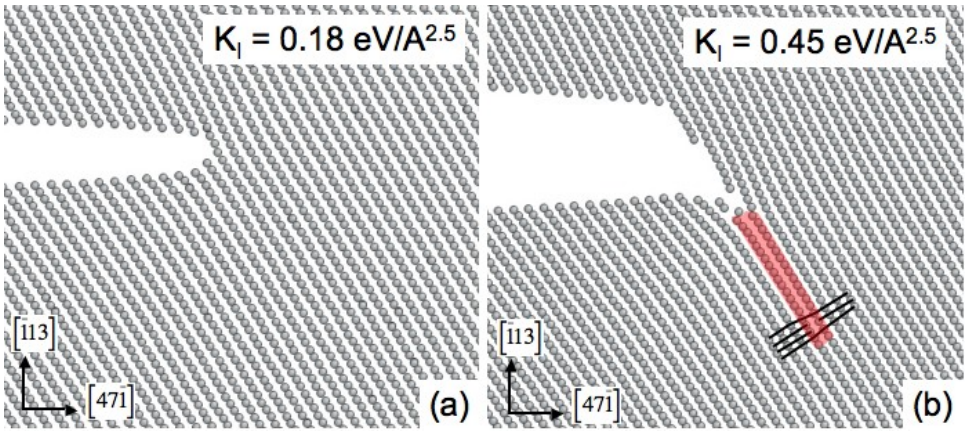

Figure 4.2: Snapshot of simulation with $\Delta K_I = 0.6$ eV/Å$^{2.5}$, $R = 0$, and friction force = 110 MPa showing crack tip sharpening by multiple dislocation emission in the first cycle. a) The initial crack tip before any dislocations have nucleated. b) The same crack tip after the nucleation of two full dislocations and a stacking fault. The highlighted area is a stacking fault created by the nucleation of a leading partial dislocation from the sharpened crack tip. The solid lines on the image show the slip created by the dislocation. The creation of a large stacking fault is rare since full dislocations are most commonly nucleated in this orientation.

cle (seen in Figure 4.4). This mechanism of permanent crack growth implies that mobile dislocations emitted from the crack tip travel far enough away from the tip that when the load is reduced, the driving force pulling the dislocations back to the tip is less than the resistance to slip they experience in their current positions. If the crack has grown but not blunted, unloading causes the crack to close in a reversible manner and no permanent crack growth is observed in that cycle. The reversibility of bonds shifting at the crack surfaces can create a sharper and cleaner crack tip than at peak load, lowering the stress intensity needed for dislocation nucleation and crack growth on the primary slip plane, promoting further deformation upon reloading. Furthermore, irreversibility of the crack tip is caused by the difference in mobility of dislocations on the primary versus oblique slip planes. Since dislocations on oblique planes contain a jog, they move more slowly than dislocations in the primary slip plane. When

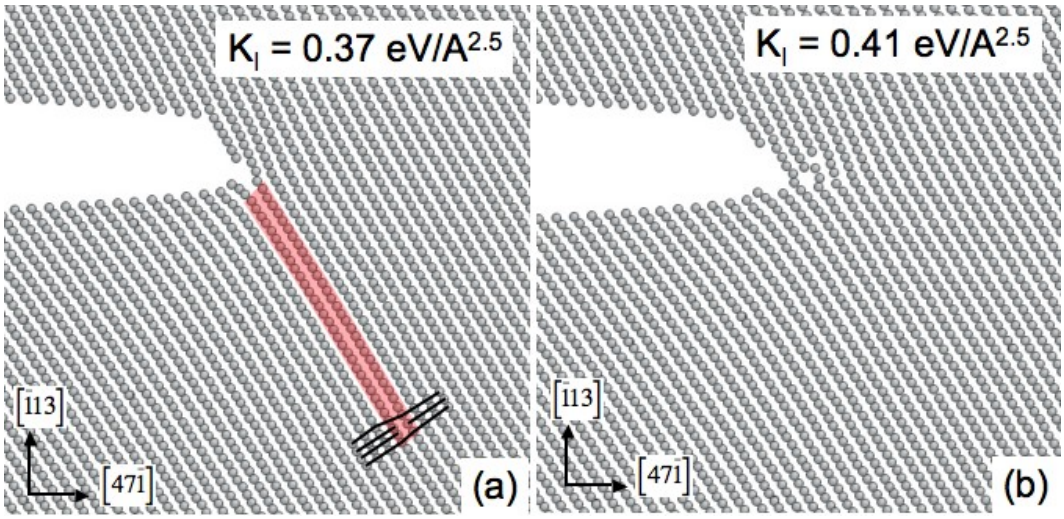

Figure 4.3: Snapshot of simulation with $\Delta K_I = 0.6$ eV/Å$^{2.5}$ and $R = 0$ showing crack tip shielding by the initial nucleated dislocation in the first cycle. The subsequent crack tip behavior is controlled by friction force, i.e. the distance of the initial dislocation from the crack tip. a) Simulation with friction force = 110 MPa. The initial dislocation has travelled over 1300 Å from the crack tip along the slip plane, allowing the crack to nucleate a second dislocation in the same slip system. Notice that the crack grows by a small increment along the $(\bar{1}13)$ plane by bonds breaking from the nucleation of the dislocation. The highlighted area is a stacking fault created by the nucleation of a leading partial dislocation from the sharpened crack tip. Like Figure 4.2, the creation of a large stacking fault is rare in comparison to the nucleation of full dislocations at higher loads. The solid lines on image show the slip created by the dislocation. b) Simulation with friction force = 500 MPa. The initial dislocation remains close to the crack tip (within 500 Å along the slip plane). Instead of nucleating a dislocation, bonds break at the crack tip extending the crack by a few Angstroms along the original crack plane.

the nucleation of several dislocations on multiple slip planes is observed, the order in which they return to the crack tip may be different than the order in which they were nucleated, changing the shape of the crack tip from one load cycle to the next. Furthermore, when a crack grows into a defect (as in Figure 4.1), the crack tip shape will be different when unloaded since the crack will find a minimum energy state different than that state with the defect that was present before the crack grew.

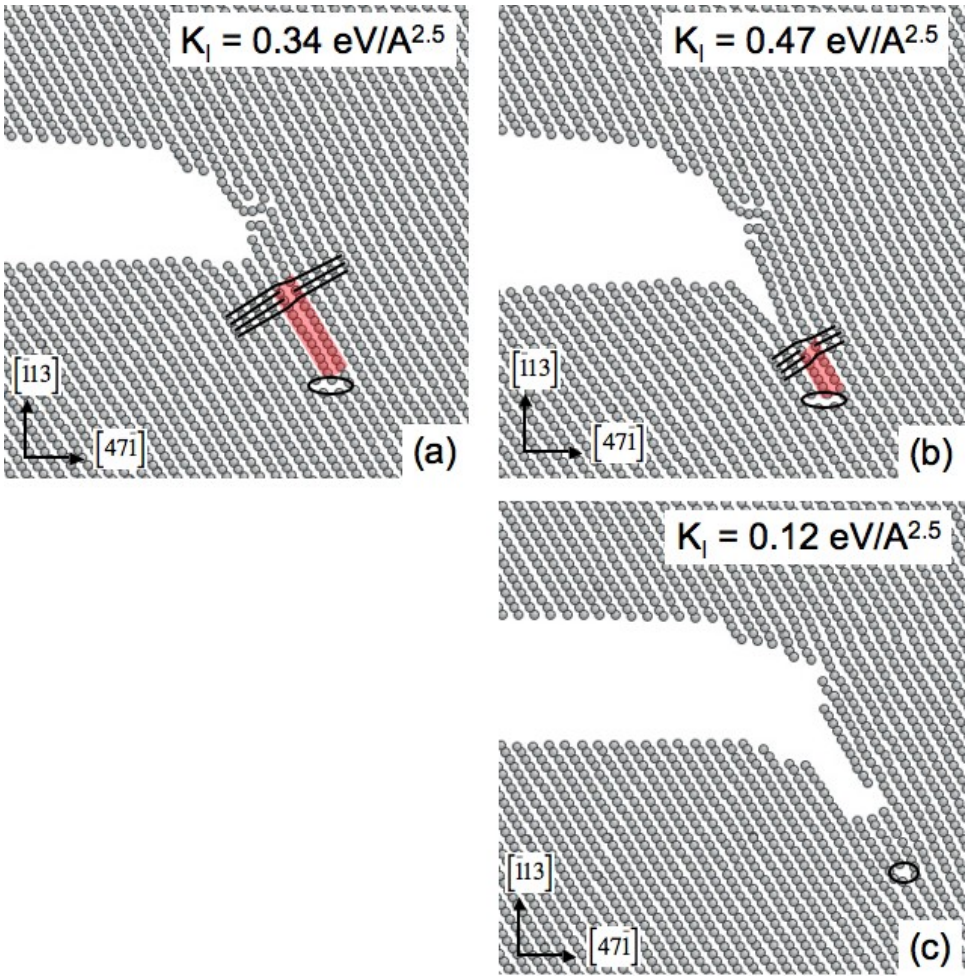

Figure 4.4: Snapshot of simulation with $\Delta K_I = 0.6$ eV/Å$^{2.5}$, $R = 0$, and friction force = 700 MPa showing effects of lattice defects near the crack tip in the second cycle. a) The crack tip has nucleated a full dislocation that propagates away from the tip, but is stopped by a defect. The defect, circled by a solid line, contains some increment of slip on an oblique slip plane. Also, lattice shifting at the top crack surface is observable. The highlighted area is a stacking fault created by the nucleation of a leading partial dislocation. The solid lines on the image show the slip created by the dislocation. The slip near the defect is difficult to visualize, thus is not shown with guiding lines. b) After the dislocation has stopped, the crack tip begins to propagate along the $\left(\bar{1}\bar{1}1\right)$ plane. The defect also arrests the crack, which blunts by nucleating oblique dislocations instead of propagating further. c) After reaching the peak load of the second cycle, the system is unloaded. The snapshot shows the extended and blunted crack tip, and the lattice defect circled with a solid line. The lattice shifting on the top crack face has disappeared as the load is removed.

In medium friction force simulations, since the friction force is increased, dislocations in the DD region remain closer to the crack tip. Closer dislocations lead to more dislocation nucleation on oblique slip systems and the creation of more dislocation junctions and permanent lattice defects. The increase in shielding from nearby dislocations and the presence of many defects promotes the growth of the crack along the $\left(\bar{1}13\right)$ crack plane. Since the number of defects increases, more dislocations along the primary slip system are blocked, which leads to more dislocations close to the tip, leading to the creation of more lattice defects. Thus, cracks that grow along the primary slip plane generally do not propagate far before being arrested by a defect. Similarly, at high friction forces, even more dislocations on oblique slip planes are nucleated, creating an abundance of lattice defects. The nearby dislocations on the primary slip plane shield the crack tip significantly, inhibiting crack growth and dislocation nucleation on the $\left(\bar{1}\bar{1}1\right)$ plane, leading to more crack growth on the $\left(\bar{1}13\right)$ plane. Since most of the dislocations do not travel far from the crack tip, most of the deformation is reversible at high friction forces.

Some of the observed mechanisms may be created artificially by the 2D nature or zero temperature of the simulations. With respect to the near-2D atomistic region, many defects maintain a 2D structure not representative of a real material. Dislocations on the primary slip plane, bond shifting at crack surfaces, dislocation junctions, and bond breaking at the crack tip are all expected to have a 3D structure, but are confined to 2D in these simulations. The artificial structure of these defects can influence the deformation observed throughout the simulations. For example, the stress required to nucleate a dislocation loop is lower than for a linear dislocation segment, and the mobility of dislocations with jogs is influenced by the periodic nature of the dislocation line. With

respect to zero temperature, all effects of thermal activation are removed. Including thermal activation will cause the nucleation of more dislocations, thus more permanent deformation, and the development of dislocation pileups at lower loads. Therefore, zero temperature simulations act as a lower limit to the number of dislocations that can be nucleated, and will reach higher loads before failure. It is worth noting that complex dislocation reactions, like dislocations changing slip planes to propagate in directions of high shear strain, are consistent with observations from thicker specimens at finite temperature [9]. While these mechanisms do not appear to be an artifact of zero temperature, they may be influenced by a thin atomistic region because large, curved dislocations may not compress into Lomer dislocations as easily as a straight dislocation line.

The FCG averaged over all recorded cycles, or all but the first cycle, is compiled for each ΔK_I and R, and plotted in Figure 4.5. The crack growth is measured along the crack path, not along the horizontal direction as in larger-scale experiments. Since the first cycle usually produces an anomalously large crack growth increment, the averaged data for all but the first cycle is a more representative value for the average FCG per cycle. The average value including the initial cycle provides more data and smoother curves, but it also increases the amount of crack growth recorded. The total number of cycles simulated ranged from 3 to 10 depending on the total crack growth accumulated over all of the cycles. Once the crack approached the MD/DD interface, the simulations were stopped. Only three cycles were run for $\Delta K_I = 0.6$ eV/Å$^{2.5}$ with $R = 0$ and $\Delta K_I = 0.5$ eV/Å$^{2.5}$ with $R = 0.25$, around 5 cycles were used for $\Delta K_I = 0.4 - 0.5$ eV/Å$^{2.5}$ with $R = 0$ and $\Delta K_I = 0.4$ eV/Å$^{2.5}$ with $R = 0.25$, and around 10 cycles were simulated for $\Delta K_I = 0.2 - 0.3$ eV/Å$^{2.5}$ with $R = 0.25$. The most variability occurs in results averaged over the fewest cycles.

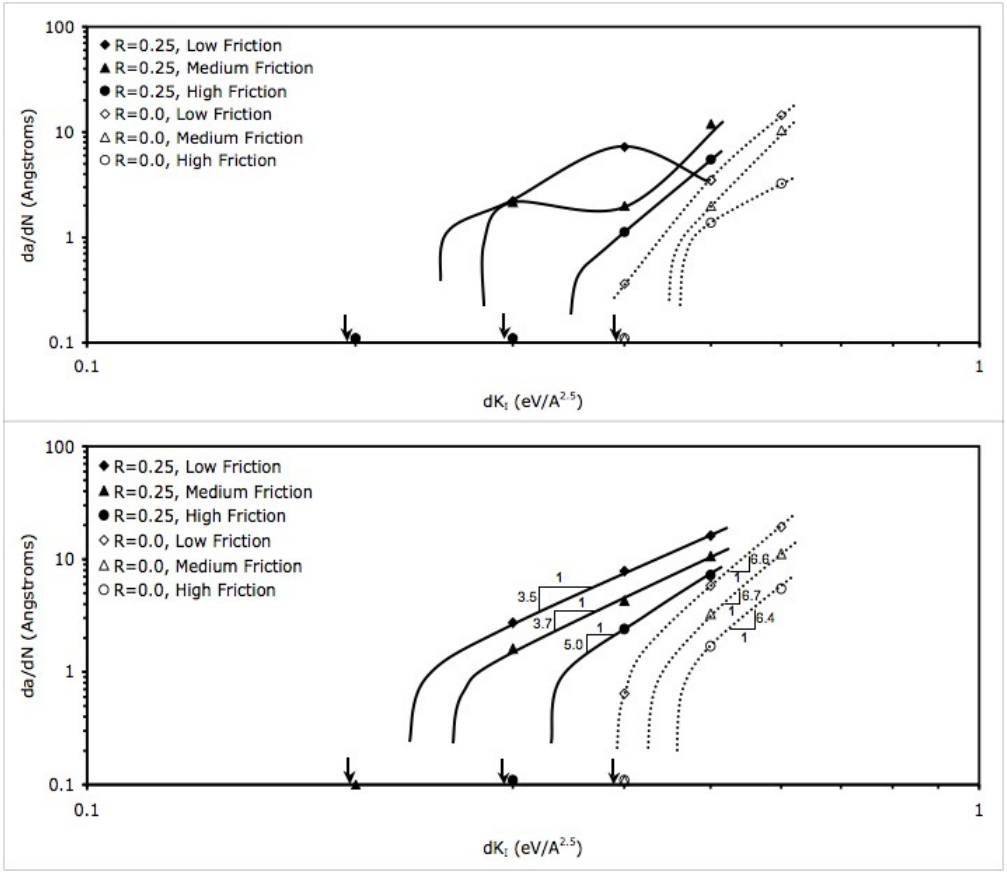

Figure 4.5: Plot of the crack growth per cycle, da/dN, as a function of the stress intensity range, ΔK_I, load ratio, R, and the friction force. The data corresponds to the average crack growth over as many cycles as were simulated at the given stress intensity range, friction force, and load ratio. The bottom plot includes crack growth values from all recorded cycles, while the top plot excludes data from the first cycle. The lines through the data are drawn to guide the eye and are not analytical functions. The downward arrows near data points indicate below-threshold values. Low friction force values correspond to 75.76, 94.33, 110, and 200 MPa. Medium friction force values correspond to 300, 400, 500, and 600 MPa. High friction force values correspond to 700, 800, 900, and 1000 MPa. The data suggests that the threshold stress intensity range decreases as the friction force decreases. Assuming that an increase in hardness corresponds to an increase in the average friction force experienced by dislocations, this trend is opposite of experimental measurements of threshold fatigue behavior in aluminum alloys [98].

The data shows an expected shift in threshold values with an increase in R, followed by an increasing amount of crack growth per cycle after threshold.

The data also indicates that the presence of a higher friction force raises ΔK_I^{th} by shifting in a similar manner to changing R. The trend is more clear when the first cycle is included in the average value, however, the change in threshold values remains the same if the first cycle is included or not. When including the first cycle, the data is fit well with a power law function for the two lowest friction force values with $R = 0.25$ (where three data points are available), and is assumed to be a power law function for the other data until the threshold value is reached. The best fit slope of the curves (the power law exponent) range between 6.4 to 6.7 for $R = 0$ and from 3.5 to 5.0 for $R = 0.25$. Using the power law crack growth functions and the threshold stress intensities, this data can be used in meso-scale simulations for near-threshold fatigue crack growth instead of a cohesive law. The crack growth mechanisms can also guide the direction of the crack path between the original crack plane or along crystallographic planes.

Interestingly, by increasing the resistance to dislocation glide more dislocations are present to shield the crack tip causing reversible bond breaking, increasing the threshold stress intensity range. This indicates that as a crack approaches an obstacle, shielding confines crack growth to the initial crack plane rather than allowing rapid growth along the primary slip plane, highlighting the importance of modeling a heterogeneous microstructure. Furthermore, if the density of dislocations is low (no large obstacles are present), then dislocation emission sharpens the crack and creates a substantial amount of irreversible deformation. Therefore, microstructures with more widely spaced obstacles to dislocation motion will show larger increments of crack growth, especially along the primary slip plane. This prediction is confirmed with experiments by Suresh (1984) who shows a decreasing fatigue threshold with an increase of precipitation spacing in aluminum alloy 7075 [99]. Laird (1967) also predicts larger

crack growth per cycle when the precipitate-free region increases in Al-4% Cu when aged from peak-aged to over-aged conditions [61].

4.5 Conclusions

Using a multiscale simulation approach combining molecular dynamics and discrete dislocation dynamics, the effect of dislocation pileups on fatigue crack propagation is investigated. The results show a transition from stage I type (single slip and crystallographic crack growth) to stage II type (multiple slip systems and smooth crack growth in the original crack plane) FCG is caused by shielding of the crack tip from dislocations on the primary slip system. Furthermore, increasing the friction force (creating smaller, more dense dislocation pileups) caused the threshold stress intensity range to increase.

The simulations also highlight several observations and mechanisms for fatigue crack growth in aluminum alloys. Initially, dislocation nucleation along the primary slip plane is favored, but changes in the crack tip geometry and local stress field (from nearby dislocations) can make crack growth more favorable. Crack growth can occur by brittle opening of a low-energy crystallographic plane (the primary slip plane), or incremental growth along the crack plane as bonds are broken from dislocation nucleation. When dislocations move far away from the crack tip, bonds broken at the crack tip during nucleation are permanently opened. Crack growth in the slip plane also occurs by opening along lattice defects, but the defects often limit the size of the crack increment. Permanent crack growth each cycle can be caused by one of several mechanisms: crack opening along the primary slip system followed by blunting, crack

tip bond breaking from the nucleation of dislocations on oblique slip systems when dislocation shielding is observed, and the duel role of lattice distortion near the tip in promoting and arresting crack propagation on the primary slip system. Crack growth aided by lattice defects occurs in all simulations, while crack propagation on the primary slip system mainly occurs in simulations with a low friction force, when dislocation shielding is low.

Using the friction force trends and mechanisms of crack growth illustrated by the simulations, it is proposed that fatigue crack growth threshold values are controlled by the spacing of obstacles to dislocation motion. A larger spacing of copper precipitates creates more room for a coarsely spaced dislocation pileup, allowing a large crack growth increment per cycle. Also, crack increments can be larger with coarser precipitation since there is more room for crack growth without interference from precipitation. An equivalent trend is observed in the literature for larger obstacles [110], and experimental observations confirm that increasing the precipitation spacing decreases the FCG threshold [99]. It is clear that material heterogeneity is important in the FCG process and must be included in models to produce accurate simulations of fatigue in aluminum alloys. If it is assumed that increasing age hardness can be accurately modeled by increasing the homogeneously applied friction force the opposite trend from experiments would be observed.

Using the crack growth per cycle measurements and threshold values from this work, mesoscale simulations can include a FCG law generated by atomistic mechanisms influenced by large scale dislocation structures. Some guidance is also available to determine whether the crack will grow along the initial crack plane or along a crystallographic plane based on proximity of nearby disloca-

tions and the size of the dislocation pileup.

Last, a detailed study of the interaction of growing fatigue cracks with damaged or pristine copper precipitates is necessary to fully understand the FCG process in aluminum alloys. It is clear that precipitation will influence the crack propagation [89], but the magnitude of the influence is still unknown.

4.6 Acknowledgements

The authors gratefully acknowledge support from Ed Glaessgen and Steve Smith at NASA (Grant No. NNX08BA39A), Paul Hess at the Office of Naval Research (Grant No. N000141010323), and Ali Sayir at the Air Force Office of Scientific Research (Grant No. FA95501110273).

APPENDIX A

FINITE TEMPERATURE, LOW STRAIN RATE SIMULATIONS OF FATIGUE CRACK GROWTH

This appendix describes attempts to use the combined spatial and temporal multiscale method developed by Baker and Warner [9] documented in Chapter 3 to study fatigue crack growth in aluminum. Other researchers have studied experimentally the effect of frequency on fatigue crack growth of aluminum alloy 2024-T3 [44]. The amount of crack growth at a fixed stress intensity range is within experimental variation for frequencies as high as 20KHz and as low as 20Hz [44]. Given the computational time constraints of the mutiscale method, a minimum frequency of 2500 KHz was simulated. This frequency is three orders of magnitude faster than the experiments, however, it is approximately three orders of magnitude slower than standard molecular dynamics methods are capable of achieving. Based on the the work from Chapter 3, slow strain rate simulations are needed to accurately model fracture behaviors in aluminum. Therefore, efforts using the combined multisale approach were attempted before performing simulations at zero temperature and high loading rates. The rest of Appendix A describes the simulation setup and results of the fatigue crack growth simulations conducted at slow loading rates at room temperature.

A.1 Simulation Setup

The specimen consisted of an fcc crystal with an edge crack very similar to that used in Chapter 3. The crystal lattice was oriented such that the horizontal axis corresponded with $\left[47\bar{1}\right]$, the vertical axis with $\left[\bar{1}13\right]$, and the out of plane di-

rection with $\left[2\bar{1}1\right]$. The crack was created by removing 3 consecutive planes of atoms. The crack plane was normal to the vertical axis with the crack front aligned with the $\left[2\bar{1}1\right]$ direction. The $\left(\bar{1}\bar{1}1\right)$ slip plane intersected the crack plane at an angle of 58.5 degrees from the horizontal, with the [011] slip direction in the x-y plane. All other slip planes are oblique to the x-y plane, so that the primary slip plane is the $\left(\bar{1}\bar{1}1\right)$ plane and the primary slip direction is the [011] direction. Since primarily full dislocations are nucleated from the crack tip, no out-of-plane displacements are created when transferring slip from the MD region to the DD region.

Using CADD, the crack tip at the center of the specimen was embedded into a 3D atomistic region of approximately $105 \times 140 \times 35$, which was encompassed by a larger 2D plane strain, DD continuum region spanning $200 \times 200 \times 0.0035$ microns or $1 \times 1 \times 0.0035$ microns. In no simulations did the dislocations approach the boundaries of the finite element region. The elastic constants of the continuum material were $C_{11} = 0.682$, $C_{12} = 0.331$, $C_{44} = 0.180$ eV/Å^3, while the atomistic region is defined by an aluminum potential from Ercolessi and Adams (1994) [28]. The temperature of the MD region was controlled via the ramped Langevin thermostat described previously, with T=300 degree K. The lattice constant at 300K was 4.051Å. Loads were applied by prescribed displacements at the outer boundary of the DD region corresponding to the continuum solution for a crack in an anisotropic linear elastic material subjected to mode I loading. The frequency of the interface updating was chosen to be on the order of half of the Debye frequency of the material (50 MD steps) to keep thermal pulses from entering the continuum domain [84]. The simulation setup was the same for all simulations except for the variation in applied friction forces.

In order to simulate precipitation hardening a friction force is added to the DD region of CADD that corresponds to the shear stress required for dislocations to pass through a field of obstacles. As mentioned in Chapter 3, vickers hardness values of H_v = 100, H_v = 122.6, and H_v = 141.6 correspond to dislocation flow stresses of τ_y = 75.76 MPa, τ_y = 94.33 MPa, τ_y = 110 MPa respectively. The simulations referenced in this Appendix only use friction force values of 110, 94.33, and 75.76 MPa. As a reference, the peak hardness of aluminum alloy 2024-T3 is around 137 [22], while the hardness of Al-4% Cu systems with primarily GP zone precipitates is around 100 [94]. The hardness value of 122.6 was used as an intermediate to these values. Using line tension models of dislocations cutting line-segment obstacles, Singh and Warner [95] calculate the shear stress needed for dislocations to overcome copper precipitates corresponding to different age hardnesses. They use Equations 4.8 and 4.9 and find excellent agreement with experimental age hardness curves of Al-4% Cu systems.

The crack tip was loaded from an unstressed state at a rate of 1×10^6 eV/Å$^{2.5}$/sec. The peak load of 0.2 eV/Å$^{2.5}$ was used because at higher loads oblique slip was observed in 2 of the 3 simulations. The oblique slip did not glide away from the tip in one case, and could not be passed by CADD into the DD region in either case. Therefore, the simulations were then unloaded from the peak load to K_I = 0.0 or K_I = 0.1 eV/Å$^{2.5}$ (R ratio of 0.0 or 0.5 respectively). The same set of simulations was run at a rate of 1×10^9 eV/Å$^{2.5}$/sec with no time acceleration so that multiple cycles could be completed.

A.2 Results

A.2.1 Loading Rate of 1×10^6 eV/Å$^{2.5}$/sec

In all three simulations, full dislocations were nucleated on the $\left(\bar{1}\bar{1}1\right)$ plane coincident with the crack plane near the peak load. The simulations with the two highest friction forces (94.33 MPa and 110 MPa) nucleated three dislocations, while the lowest friction force (75.76 MPa) simulation nucleated four dislocations. This difference is most likely due to the randomness of thermally activated nucleation at the crack tip, but it is observed in the literature that lower friction forces generally coincide with more dislocations nucleated at sources near a crack tip than higher friction forces in DD simulations [17]. Since these simulations require a substantial computational investment (see Chapter 3), only the simulation with a friction force of 94.33 MPa was unloaded and received a second loading-unloading cycle. Upon unloading, the closest dislocation was re-absorbed back into the crack tip, while the remaining two dislocations stayed stationary. In the second cycle, near the peak load, a full dislocation was nucleated on the same slip plane and traveled to approximately the same distance as the dislocation that was re-absorbed. The outer dislocations moved only minimally away from the crack tip when the nucleated dislocation reached its equilibrium position. Again upon unloading, the closest dislocation was re-absorbed into the crack tip, leaving only two dislocations at the end of the second loading-unloading cycle. The simulation with a friction force of 75.76 MPa was unloaded until the closest dislocation (the fourth full dislocation that was nucleated in this case) was re-absorbed back into the crack tip. The distance traveled by the dislocations away from the crack tip in each simulation is given

as a function of time in Figure A.1.

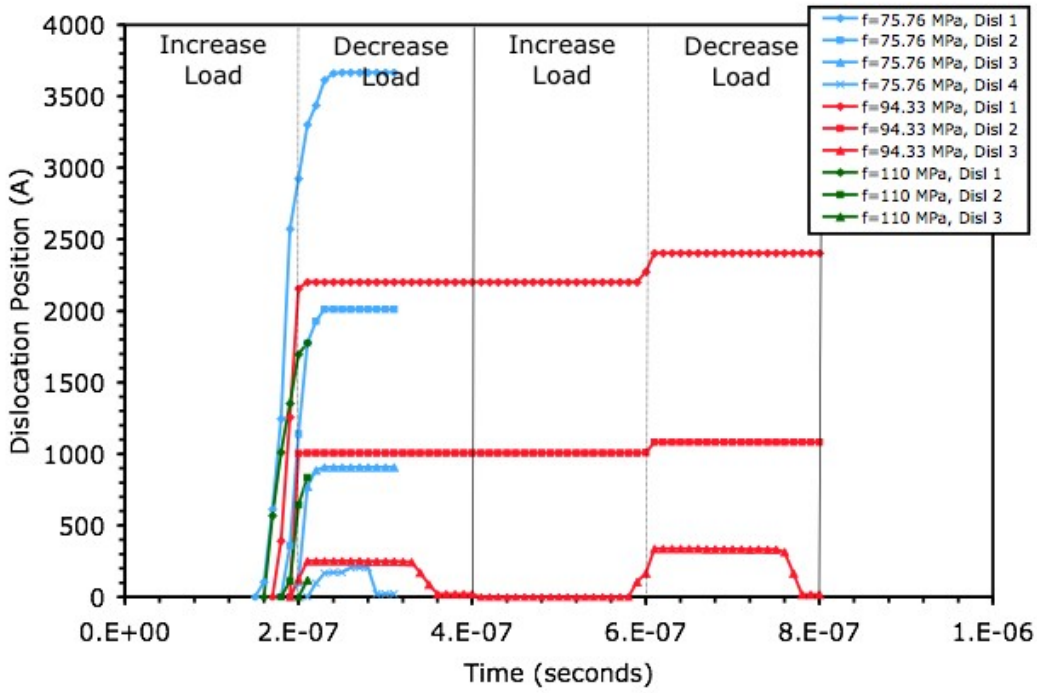

Figure A.1: Distance of all dislocations away from the crack tip along their slip plane as a function of time in fatigue simulations conducted at a loading rate of 1×10^6 eV/Å$^{2.5}$/sec, with $\Delta K_I = 0.2$ eV/Å and $R = 0$. The unloading and loading portion of each cycle are labeled for clarity.

A.2.2 Loading Rate of 1×10^9 eV/Å$^{2.5}$/sec

At this loading rate three cycles were performed with R=0.5, and two cycles were performed with R=0.0 for all three friction force settings. When cycled twice at R=0.0 all three simulations with different friction forces nucleated a single dislocation near the peak load of 0.2 eV/Å$^{2.5}$. The dislocations moved away from the crack tip until the load was reduced enough upon unloading that the driving force for the dislocation glide dropped below the friction force, leaving the dislocations stationary. When the crack tip was reloaded for a second cycle,

the existing dislocations moved away from the crack tip and reached a stationary position upon the unloading portion of the second cycle. In all cases no new dislocations were nucleated in the second cycle. The distance traveled by the dislocations away from the crack tip in each simulation is given as a function of time in Figure A.2a.

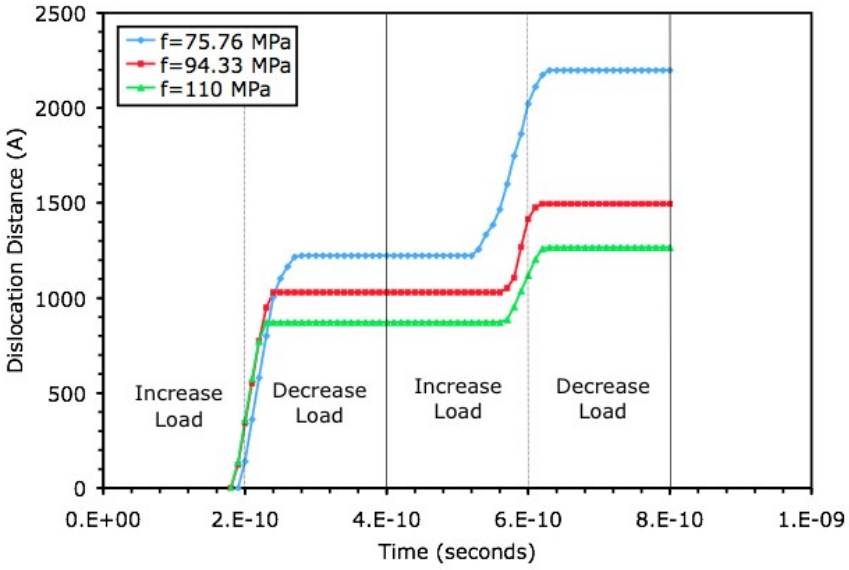

(a)

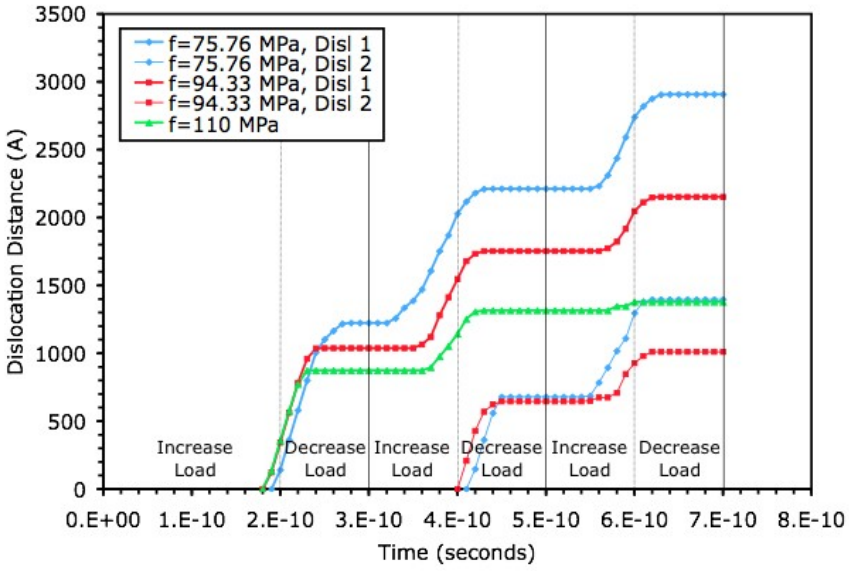

(b)

Figure A.2: Distance of all dislocations away from the crack tip along their slip plane as a function of time in fatigue simulations conducted at a loading rate of 1×10^9 eV/Å$^{2.5}$/sec. The unloading and loading portion of each cycle are labeled for clarity. a) Simulation with $\Delta K_I = 0.2$ eV/Å and $R = 0$. b) Simulation with $\Delta K_I = 0.1$ eV/Å and $R = 0.5$.

When cycled at R=0.5 all three simulations with different friction forces again nucleated a single dislocation. The dislocations were driven away from the crack tip, then remained stationary as the load was reduced in the unloading portion of the first cycle. In the second cycle, another dislocation was nucleated in the two simulations with friction forces of 75.76 MPa and 94.33 MPa. Again, the reason each friction force did or did not nucleate a second dislocation may be due to the randomness of the nucleation process, however, the closest dislocation was within the range mentioned in Chapter 3 where shielding of the crack tip could occur. During the second cycle, the existing dislocations were driven away from the crack by the crack tip stress field or the stress field from the crack and the other nucleated dislocations. During the unloading portion of the second cycle, all dislocations remained stationary and were not re-absorbed back into the crack tip. In the third cycle, no new dislocations were nucleated. The only dislocation in the simulation with the highest friction force moved only slightly indicating that it had reached its equilibrium position at the peak load. The two dislocations with the other friction forces moved outward to find their equilibrium positions, and again remained stationary in the unloading portion of the third cycle. The distance traveled by the dislocations away from the crack tip in each simulation is given as a function of time in Figure A.2b.

A.3 Discussion and Conclusions

From the figures, it is clear that a change in friction force changes the equilibrium distance of the dislocations nucleated from the crack tip. This behavior is observed at both strain rates and for all loading conditions, and is consistent with observations from Chapter 3. Also in agreement with results from Chapter

3, the finite temperature simulations show the nucleation of dislocations from the crack tip only when the closest dislocation is beyond 500 from the crack tip. The influence of dislocations shielding the crack tip from nucleating a dislocation on the primary slip plane may be different at finite temperature due to thermal fluctuations, however, the minimum distance of the closest dislocation at which another dislocation was nucleated from the crack tip was approximately 640 (in simulation with friction force = 110 MPa and a loading rate of 1×10^6 eV/Å$^{2.5}$/sec).

Despite the nucleation of several dislocations along the primary slip plane in the slower loading rate simulations, the results indicate that the applied stress intensity range is below the threshold value. For the simulations with the two lowest friction forces (75.76 and 94.33 MPa) the closest dislocation returns to the crack tip, and in the simulation with a friction force of 94.33 MPa the dislocation structure is nearly identical in both loading cycles. Since some irreversible dislocation motion is needed for fatigue crack growth [23], the fully reversible dislocation structure indicates that no crack growth is expected. Unfortunately, the stress intensity range of $\Delta K_I = 0.2$ eV/Å^2.5 may be above the threshold value for this simulation, but may require many cycles to see a single increment of crack growth. It is observed in the simulation with two cycles at the slowest loading rate that the dislocations that do not return to the crack tip move away slightly in the second cycle, then remain there upon unloading. This process could continue for many cycles, with slow incremental movement of the outer dislocations until the innermost dislocation becomes trapped by the friction force. In this case, depending on the distance of the innermost dislocation, another dislocation could be nucleated and added to the pileup. This process may be limited, however, by the strength of the friction force holding the pileup

in place. In other words, the pileup may reach a critical number of dislocations that it will be too difficult to move the outer dislocations to make room for the nucleation of another.

Simulations conducted at slower loading rates and finite temperatures produce distinctly different results as those at high loading rates or zero temperature. At higher loading rates, dislocations do not reach their equilibrium distance from the crack tip until at least another cycle is completed. If approximating slower loading rates with a faster loading rate simulation, the distance of the closest dislocation may not be representative of a slower loading rate which changes the number of dislocations nucleated, and thus the crack growth, per cycle. Furthermore, more dislocations were nucleated by thermal activation at slower loading rates. This will likely change the possible crack growth mechanisms and therefore the crack growth per cycle. Similarly, simulations at zero temperature do not include thermal activation, therefore they differ greatly in the number of dislocations present at a given load. It is clear that finite temperature, slow loading rate simulations are needed to accurately model fatigue crack processes in aluminum alloys, but the combined multiscale scheme developed in Chapter 3 is insufficient to handle the observed mechanisms of fatigue crack growth above the threshold level.

BIBLIOGRAPHY

[1] Farid F. Abraham, D. Brodbeck, R. A. Rafey, and W. E. Rudge. Instability dynamics of fracture: A computer simulation investigation. *Physcial Review Letters*, 73(2):272–275, 1994.

[2] James E. Angelo, N. R. Moody, and M. I. Baskes. Trapping of hydrogen to lattice defects in nickel. *Modelling and Simulation in Material Science and Engineering*, 3:289–307, 1995.

[3] L. E. Araripe, J. S. Andrade Jr., and R. N. Costa Filho. Memory effects on the statistics of fragmentation. *Physical Review E*, 71(036119):1–5, 2005.

[4] Wm. T. Ashurst and Brad Lee Holian. Droplet formation by rapid expansion of a liquid. *Physical Review E*, 59(6):6742–6752, 1999.

[5] Jan stöm, Markku Kellomäki, and Jussi Timonen. Dynamic fragmentation of a two-dimensional brittle material with quench disorder. *Physical Review E*, 55(4):4757–4761, 1997.

[6] J. A. ström, B. L. Holian, and J. Timonen. Universality in fragmentation. *Physical Review Letters*, 84(14):3061–3064, 2000.

[7] J. A. ström, F. Ouchterlony, R. P. Linna, and J. Timonen. Universal dynamic fragmentation in d dimensions. *Physical Review Letters*, 92(24):24506–1–4, 2004.

[8] Jan ström and Jussi Timonen. Fragmentation by crack branching. *Physical Review Letters*, 78(19):3677–3680, 1997.

[9] K.L. Baker and D.H. Warner. Extended timescale atomistic modeling of crack tip behavior in aluminum. *Modelling and Simulation in Material Science and Engineering*, 20:065005, 2012.

[10] Glenn E. Beltz, Don M. Lipkin, and Lisa L. Fischer. Role of crack blunting in ductile versus brittle response of crystalline materials. *Physical Review Letters*, 82:4468–4471, 1999.

[11] W. Benz and E. Asphaug. Simulations of brittle solids using smooth particle hydrodynamics. *Computer Physics Communications*, 87:253–265, 1995.

[12] Aldo Bonasera. Hydrogen clusters get critical. *Physics World*, 12(2):20, 1999.

[13] Markus J. Buehler and Huajian Gao. Dynamical fracture instabilities due to local hyperelasticity at crack tips. *Nature*, 439:307–310, 2006.

[14] Xavier Campi. Multifragmentation: nuclei break up like percolation clusters. *Journal of Physics A: Mathematical and General*, 19(15):L917–L921, 1986.

[15] H. A. Carmona, F. K. Wittel, F. Kun, and H. J. Herrmann. Fragmentation processes in impact of spheres. *Physical Review E*, 77(051302):1–10, 2008.

[16] L. Y. Chen and N. J. M. Horing. An exact formulation of hyperdynamics simulations. *Journal of Chemical Physics*, 126:224103, 2007.

[17] Q. Chen, V.S. Deshpande, E. Van Der Giessen, and A. Needleman. Friction stress effects on mode i crack growth predictions. *Scripta Materialia*, 48:755–759, 2003.

[18] Emily S.C. Ching, Y.Y. Yiu, and K.F. Lo. Energy dependence of mass distributions in fragmentation. *Physica A*, 265:119–128, 1999.

[19] John D. Clayton. A model for deformation and fragmentation in crushable brittle solids. *International Journal of Impact Engineering*, 35:269–289, 2008.

[20] Robert D. Cook, David S. Malkus, Michael E. Plesha, and Robert J. Witt. *Concepts and Applications of Finite Element Analysis*. John Wiley & Sons, Inc., 2002.

[21] M. D'Agostino, F. Gulminelli, Ph. Chomaz, M. Bruno, F. Cannata, R. Bougault, N. Colonna, F. Gramegna, I. Iori, N. Le Neindre, G. V. Margagliotti, P. F. Mastinu, P. M. Milazzo, A. Moroni, and G. Vannini. Negative heat capacity in the critical region of nuclear fragmentation: an experimental evidence of the liquid-gas phase transition. *Physics Letters B*, 473(3–4):219–225, 2000.

[22] MatWeb Material Property Data. Aluminum 2024-t3. www.matweb.com/search/SpecificMaterial.asp?bassnum=MA2024T3. Provided by the Aluminum Association, Inc.

[23] V.S. Deshpande, A. Needleman, and E. Van Der Giessen. A discrete dis-

location analysis of near-threshold fatigue crack growth. *Acta Materialia*, 49:3189–3203, 2001.

[24] V.S. Deshpande, A. Needleman, and E. Van Der Giessen. Discrete dislocation modeling of fatigue crack propagation. *Acta Materialia*, 50:831–846, 2002.

[25] V.S. Deshpande, A. Needleman, and E. Van Der Giessen. Discrete dislocation plasticity modeling of short cracks in single crystals. *Acta Materialia*, 51:1–15, 2003.

[26] V.S. Deshpande, A. Needleman, and E. Van Der Giessen. Scaling of discrete dislocation predictions for near-threshold fatigue crack growth. *Acta Materialia*, 51:4637–4651, 2003.

[27] A. Diehl, H. A. Carmona, L. E. Araripe, J. S. Andrade Jr., and G. A. Farias. Scaling behavior in exposive fragmentation. *Physical Review E*, 62(4):4742–4746, 2000.

[28] F. Ercolessi and J. B. Adams. Interatomic potentials from 1st-principles calculations – the force-matching method. *Europhysics Letters*, 26(8):583–588, 1994.

[29] Michael L. Falk, Alan Needleman, and James R. Rice. A critical evaluation of cohesive zone models of dynamic fracture. *Journal de Physique IV France*, 11:Pr5–43–50, 2001.

[30] B. Farizon, M. Farizon, M. J. Gaillard, F. Gobet, M. Carré, J. P. Buchet, P. Scheier, and T. D. Märk. Experimental evidence of critical behavior in cluster fragmentation using an event-by-event data analysis. *Physical Review Letters*, 81(19):4108–4111, 1998.

[31] D. Farkas, M. Duranduru, W.A. Curtin, and C. Ribbens. Multiple-dislocation emission from the crack tip in the ductile fracture of al. *Philosophical Magazine A*, 81:1241–1255, 2001.

[32] Kristen A. Fichthorn, Radu A. Miron, Yushan Wang, and Yogesh Tiwary. Accelerated molecular dynamics simulation of thin-film growth with the bond-boost method. *Journal of Physics: Condensed Matter*, 21:084212, 2009.

[33] Lisa L. Fischer and Glenn E. Beltz. The effect of crack blunting on the

competition between dislocation nucleation and cleavage. *Journal of the Mechanics and Physics of Solids*, 49:635–654, 2001.

[34] M. E. Fisher. The theory of equilibrium critical phenomena. *Reports on Progress in Physics*, 30:615–730, 1967. See page 708 for critical droplet critical exponents.

[35] F. Gobet, B. Farizon, M. J. Gaillard, J. P. Buchet, M. Carré, P. Scheier, and T. D. Märk. Cluster multifragmentation and percolation transition: A quantitative comparison for two systems of the same size. *Physical Review A*, 63(033202):1–5, 2001.

[36] D. E. Grady. Fragment size distributions from the dynamic fragmentation of brittle solids. *International Journal of Impact Engineering*, 35:1557–1562, 2008.

[37] D. E. Grady and M. E. Kipp. Geometric statistics and dynamic fragmentation. *Journal of Applied Physics*, 58(3):1210–1222, 1985.

[38] F. Gulminelli and Ph. Chomaz. Critical behavior in the coexistence region of finite systems. *Physical Review Letters*, 82(7):1402–1405, 1999.

[39] S. Hai and E.B. Tadmor. Deformation twinning at aluminum crack tips. *Acta Materialia*, 51:117–131, 2003.

[40] Shotaro Hara and Ju Li. Adaptive strain-boost hyperdynamics simulations of stress-driven atomic processes. *Physical Review B*, 82:184114, 2010.

[41] Yoshinori Hayakawa. Impact fragmentation of an ideal brittle crystal. *Physical Review B*, 53(22):14828–14833, 1996.

[42] A. S. Hirsch, A. Bujak, J. E. Finn, L. J. Gutay, R. W. Minich, N. T. Porile, R. P. Scharenberg, B. C. Stringfellow, and F. Turkot. Experimental results from high energy proton-nucleus interactions, critical phenomina, and the thermal liquid drop model of fragment production. *Physical Review C*, 29:508–525, 1984.

[43] Brad Lee Holian and Dennis E. Grady. Fragmentation by molecular dynamics: The microscopic "big bang". *Physical Review Letters*, 60(14):1355–1358, 1988.

[44] B. Holper, H. Mayer, A.K. Vasudevan, and S.E. Stanzl-Tschegg. Near

threshold fatigue crack growth at positive load ratio in aluminum alloys at low and ultrasonic frequency: influences of stran rate, slip behaviour and air humidity. *International Journal of Fatigue*, 26:27–38, 2004.

[45] Ho Jung Hwang, Oh-Keun Kwon, and Jeong Won Kang. Copper nanocluster diffusion in carbon nanotube. *Solid State Communications*, 129:687–690, 2004.

[46] A. R. Ingraffea. *Computational Fracture Mechanics, Volume 2, Chapter 11*. John Wiley & Sons, Inc., 2007.

[47] Tsukasa Ishii and Mitsugu Matsushita. Fragmentation of long thin glass rods. *Journal of The Physical Society of Japan*, 61(10):3474–3477, 1992.

[48] Hannes Jónsson, Greg Mills, and Karsten W. Jacobsen. *Classical and Quantum Dynamics in Condensed Phase Simulations*, chapter Nudged elastic band method for finding minimum energy paths of transitions, pages 385–404. World Scientific, 1998.

[49] Toshihiko Kadono. Fragment mass distribution of platelike objects. *Physical Review Letters*, 78(8):1444–1447, 1997.

[50] Toshihiko Kadono and Masahiko Arakawa. Crack propagation in thin glass plates caused by high velocity impact. *Physical Review E*, 65(035107(R)):1–4, 2002.

[51] Hiroaki Katsuragi, Satoshi Ihara, and Haruo Honjo. Explosive fragmentation of a thin ceramic tube using pulsed power. *Physical Review Letters*, 95(095503):1–4, 2005.

[52] Hiroaki Katsuragi, Daisuke Sugino, and Haruo Honjo. Scaling of impact fragmentation near the critical point. *Physical Review E*, 68(046105):1–6, 2003.

[53] Hiroaki Katsuragi, Daisuke Sugino, and Haruo Honjo. Crossover of weighted mean fragment mass scaling in two-dimensional brittle fragmentation. *Physical Review E*, 70(065103(R)):1–4, 2004.

[54] P. Kekäläinen, J. A. ström, and J. Timonen. Solution for the fragment-size distribution in a crack-branching model of fragmentation. *Physical Review E*, 76(026112):1–7, 2007.

[55] W.K. Kim and M.L. Falk. Accelerated molecular dynamics simulation of low-velocity frictional sliding. *Modelling and Simulation in Materials Science and Engineering*, 18:034003, 2010.

[56] Woo Kyun Kim and Michael L. Falk. Reformulating hyperdynamics without a transition state theory dividing surface. arXiv:1004.4703v1, April 2010.

[57] Ferenc Kun and Hans J. Herrmann. A study of fragmentation processes using a discrete element method. *Computer Methods in Applied Mechanics and Engineering*, 138:3–18, 1996.

[58] Ferenc Kun and Hans J. Herrmann. Transition from damage to fragmentation in collision of solids. *Physical Review E*, 59(3):2623–2632, 1999.

[59] Akihiro Kushima, Xi Lin, Ju Li, Jacob Eapen, John C. Mauro, Xiaofeng Qian, Phong Diep, and Sidney Yip. Computing the viscosity of supercooled liquids. *The Journal of Chemical Physics*, 130:224504, 2009.

[60] Alessandro Laio and Michele Parrinello. Escaping free-energy minima. *Proceedings of the National Academy of Sciences of the United States of America*, 99:12562–12566, 2002.

[61] C. Laird and G. Thomas. On fatigue-induced reversion and overaging in dispersion strengthened alloy systems. *International Journal of Fracture*, 3:81–97, 1967.

[62] S. Levy and J. F. Molinari. Dynamic fragmentation of ceramics, signature of defects and scaling of fragment sizes. *Journal of the Mechanics and Physics of Solids*, 58:12–26, 2010.

[63] S. Levy, J. F. Molinari, I. Vicari, and A. C. Davison. Dynamic fragmentation of a ring: Predictable fragment mass distribution. *Physical Review E*, 82:066105, 2010.

[64] J. Li. Atomeye: an efficient atomistic configuration viewer. *Modelling and Simulation in Materials Science and Engineering*, 11:173–177, 2003.

[65] Spandan Maiti, Krishnan Rangaswamy, and Philippe H. Geubelle. Mesoscale analysis of dynamic fragmentation of ceramics under tension. *Acta Materialia*, 53:823–834, 2005.

[66] Ethan A. Mastny and Juan J. de Pablo. Melting line of the lennard-jones system, infinite size, and full potential. *The Journal of Chemical Physics*, 127:104504, 2007.

[67] J. McKittrick, P.K. Liaw, S.I. Kwun, and M.E. Fine. Threshold for fatigue macrocrack propagation in some aluminum alloys. *Metallurgical Transactions A*, 12A:1535–1539, 1981.

[68] Anders Meibom and Ivar Balslev. Composite power laws in shock fragmentation. *Physical Review Letters*, 76(14):2492–2494, 1996.

[69] Patrick Michel, Paolo Tanga, Willy Benz, and Derek C. Richardson. Formation of asteroid families by catastrophic disruption: Simulations with fragmentation and gravitational reaccumulation. *Icarus*, 160:10–23, 2002.

[70] O. Miller, L. B. Freund, and A. Needleman. Modeling and simulation of dynamic fragmentation in brittle materials. *International Journal of Fracture*, 96:101–125, 1999.

[71] Ronald E. Miller and E.B. Tadmor. A unified framework and performance benchmark of fourteen multiscale atomistic/continuum coupling methods. *Modelling and Simulation in Material Science and Engineering*, 17:053001, 2009.

[72] Radu A. Miron and Kristen A. Fichthorn. Accelerated molecular dynamics with the bond-boost method. *Journal of Chemical Physics*, 119(12):6210–6216, 2003.

[73] J. F. Molinari, G. Gazonas, R. Raghupathy, A. Rusinek, and F. Zhou. The cohesive element approach to dynamic fragmentation: The question of energy convergence. *International Journal for Numerical Methods in Engineering*, 69:484–503, 2007.

[74] N. F. Mott and E. H. Linfoot. A theory of fragmentation. *Ministry of Supply*, A.C.3348:207–215, 1943.

[75] A. K. Nair, D. H. Warner, and R. G. Hennig. Coupled quantum-continuum analysis of crack tip processes in aluminum. *Journal of the Mechanics and Physics of Solids*, 59:2476–2487, 2011.

[76] A. K. Nair, D. H. Warner, R. G. Hennig, and W. A. Curtin. Coupling

quantum and continuum scales to predict crack tip dislocation nucleation. *Scripta Materialia*, 63:1212–1215, 2010.

[77] L. D. Nguyen, K. L. Baker, and D. H. Warner. Atomistic predictions of dislocation nucleation with transition state theory. *Physical Review B*, 84:024118, 2011.

[78] Lene Oddershede, Peter Dimon, and Jokob Bohr. Self-organized criticality in fragmentation. *Physical Review Letters*, 71(19):3107–3110, 1993.

[79] D. M. Owen, S. Zhuang, A. J. Rosakis, and G. Ravichandran. Experimental determination of dynamic crack initiation and propagation fracture toughness in thin aluminum sheets. *International Journal of Fracture*, 90:153–174, 1998.

[80] Jicai Pan, Subal Das Gupta, and Martin Grant. First order phase transition in intermediate-energy heavy ion collisions. *Physical Review Letters*, 80(6):1182–1185, 1998.

[81] Danny Perez, Blas P. Uberuaga, Yunsic Shim, Jacques G. Amar, and Arthur F. Voter. *Annual Reports in Computational Chemistry*, chapter Accelerated Molecular Dynamics Methods: Introduction and Recent Developments, pages 79–98. Elsevier, 2009.

[82] Danny Perez and Arthur F. Voter. Accelerating atomistic simulations through self-learning bond-boost hyperdynamics. Unpublished, May 2008.

[83] S. J. Plimpton. Fast parallel algorithms for short-ranged molecular dynamics. *Journal of Computational Physics*, 117:1–19, 1995.

[84] S. Qu, V. Shastry, W. A. Curtin, and R. E. Miller. A finite-temperature dynamic coupled atomistic/discrete dislocation method. *Modelling and Simulation in Materials Science and Engineering*, 13:1101–1118, 2005.

[85] Gonzalo Ruiz, Michael Ortiz, and Anna Pandolfi. Three-dimensional finite-element simulation of the dynamic brazilian test on concrete cylinders. *International Journal for Numerical Methods in Engineering*, 48:963–994, 2000.

[86] Eileen V. Ryan and H. J. Melosh. Impact fragmentation: From the laboratory to asteroids. *Icarus*, 133:1–24, 1998.

[87] E. Saether, V. Yamakov, and E. H. Glaessgen. An embedded statistical method for coupling molecular dynamics and finite element analyses. *International Journal for Numerical Methods in Engineering*, 78:1292–1319, 2009.

[88] N. Sator, S. Mechkov, and F. Sausset. Generic behaviours in impact fragmentation. *Europhysics Letters*, 81(44002):1–6, 2008.

[89] V.M.J Sharma, K. Sree Kumar, B. Nageswara Rao, and S.D. Pathak. Fatigue crack growth of aa2219 under different aging conditions. *Materials Science and Engineering: A*, 528:4040–4049, 2011.

[90] Tongye Shen and Donald Hamelberg. A statistical analysis of the precision of reweighting-based simulations. *The Journal of Chemical Physics*, 129:034103, 2008.

[91] V. B. Shenoy, R. Miller, E. B. Tadmor, R. Phillips, and M. Ortiz. Quasicontinuum models of interfacial structure and deformation. *Physical Review Letters*, 80:742–745, 1998.

[92] L. E. Shilkrot, Ronald E. Miller, and William A. Curtin. Multiscale plasticity modeling: coupled atomistics and discrete dislocation mechanics. *Journal of the Mechanics and Physics of Solids*, 52:755–787, 2004.

[93] L.E. Shilkrot, R.E. Miller, and W.A. Curtin. Coupled atomistic and discrete dislocation plasticity. *Physical Review Letters*, 89:025501, 2002.

[94] J.M. Silcock, T.J. Heal, and H.K. Hardy. Structural ageing characteristics of binary al-cu alloys. *Journal Institute of Metals*, 82:239–248, 1953–1954.

[95] C.V. Singh and D.H. Warner. Atomistic-based multiscale predictions of age hardening in al-cu alloy. Submitted to JMPS.

[96] Mads R. Sørensen and Arthur F. Voter. Temperature-accelerated dynamics for simulation of infrequent events. *Journal of Chemical Physics*, 112:9599–9606, 2000.

[97] A. Strachan and C. O. Dorso. Temperature and energy partition in fragmentation. *Physical Review C*, 59(1):285–294, 1999.

[98] S. Suresh. *Fatigue of Materials*. Cambridge University Press, 1998.

[99] S. Suresh, A.K. Vasudevan, and P.E. Bretz. Mechanisms of slow fatigue crack growth in high strength aluminum alloys: Role of microstructure and environment. *Metallurgical Transactions A*, 15A:369–379, 1984.

[100] E.B. Tadmor and S. Hai. A peierls criterion for the onset of deformation twinning at a crack tip. *Journal of the Mechanics and Physics of Solids*, 51:765–793, 2003.

[101] G. I. Taylor. Plastic strain in metals. *Journal of the Institute of Metals*, 62:307–324, 1938.

[102] S. Toxvaerd. Fragmentation of fluids by molecular dynamics. *Physical Review E*, 58(1):704–712, 1998.

[103] Blas Pedro Uberuaga, Steven J. Stuart, and Arthur F. Voter. Parallel replica dynamics for driven systems: Derivation and application to strained nanotubes. *Physical Review B*, 75:014301, 2007.

[104] Erik van der Giessen and Alan Needleman. Discrete dislocation plasticity: a simple planar model. *Modelling and Simulation in Material Science and Engineering*, 3:689–735, 1995.

[105] Eric Vanden-Eijnden and Fabio A. Tal. Transition state theory: Variational formulation, dynamical corrections, and error estimates. *The Journal of Chemical Physics*, 123:184103, 2005.

[106] Eric Vanden-Eijnden and Maddalena Venturoli. Revisiting the finite temperature string method for the calculation of reaction tubes and free energies. *The Journal of Chemical Physics*, 130:194103, 2009.

[107] Arthur F. Voter. Hyperdynamics: Accelerated molecular dynamics of infrequent events. *Physical Review Letters*, 78(20):3908–3911, 1997.

[108] Arthur F. Voter. A method for accelerating the molecular dynamics simulation of infrequent events. *Journal of Chemical Physics*, 106(11):4665–4677, 1997.

[109] Arthur F. Voter. Parallel replica method for dynamics of infrequent events. *Physical Review B*, 57(22):R13985–R13988, 1998.

[110] R.J.H. Wanhill. Low stres intensity fatigue crack growth in 2024-t3 and t351. *Engineering Fracture Mechanics*, 30:233–260, 1988.

[111] D. H. Warner and W. A. Curtin. Origins and implications of temperature-dependent activation energy barriers for dislocation nucleation in face-centered cubic metals. *Acta Materialia*, 57:4267–4277, 2009.

[112] D.H. Warner, W.A. Curtin, and S. Qu. Rate dependence of crack-tip processes predicts twinning trends in f.c.c. metals. *Nature Materials*, 6:876–881, 2007.

[113] R.P. Wei. Fatigue-crack propagation in a high-strength aluminum alloy. *The International Journal of Fracture Mechanics*, 4:159–168, 1968.

[114] F. Wittel, F. Kun, H. J. Herrmann, and B. H. Kröplin. Fragmentation of shells. *Physical Review Letters*, 93(3):1–4, 2004.

[115] F. K. Wittel, F. Kun, H. J. Herrmann, and B. H. Kröplin. Breakup of shells under explosion and impact. *Physical Review E*, 71(016108):1–11, 2005.

[116] Fenghua Zhou, Jean-François Molinari, and K. T. Ramesh. Analysis of the brittle fragmentation of an expanding ring. *Computational Materials Science*, 37:74–85, 2006.

[117] Fenghua Zhou, Jean-François Molinari, and K. T. Ramesh. A cohesive model based fragmentation analysis: effects of strain rate and initial defects distribution. *International Journal of Solids and Structures*, 42:5181–5207, 2005.

[118] Fenghua Zhou, Jean-François Molinari, and K. T. Ramesh. Characteristic fragment size distributions in dynamic fragmentation. *Applied Physics Letters*, 88(261918):1–3, 2006.

[119] S. J. Zhou, P. S. Lomdahl, R. Thomson, and B. L. Holian. Dynamic crack processes via molecular dynamics. *Physical Review Letters*, 76:2318–2321, 1996.